FILAMENTATION AND WHITE LIGHT GENERATION WITH SPATIALLY AND TEMPORALLY CONTROLLED FEMTOSECOND RADIATION

A Dissertation

by

NECATI KAYA

Submitted to the Office of Graduate and Professional Studies of
Texas A&M University
in partial fulfillment of the requirements for the degree of

DOCTOR OF PHILOSOPHY

Chair of Committee,	Hans A. Schuessler
Committee Members,	Siu A. Chin
	Dong H. Son
	Alexandre A. Kolomenskii
Head of Department,	George R. Welch

December 2014

Major Subject: Physics

ABSTRACT

Present laser technology allows the production of ultrashort and intense laser pulses. When matter is exposed to the laser field of such pulses, it exhibits highly nonlinear phenomena that find applications in many fields. Among these phenomena studied in this work are supercontinuum (white light) generation, filamentation, and photodissociation. First we show how the spatial profile of a laser beam can be formed with a phase grating created on a spatial light modulator and then analyzed with a holographic knife-edge method. Then we investigate some possibilities of controlling the nonlinear dynamics of laser-matter interaction by manipulations of the laser field such as creating spatially structured beams, forming high order paraxial beam modes or crossing two femtosecond laser beams in a medium. Additionally, as the first step toward coherent control and manipulation of the interaction of femtosecond radiation with molecular systems, a reconstruction of the momentum fragment distribution of laser-induced photo-dissociation of hydrogen molecular ions produced by 800 nm central wavelength, 50 fs laser pulses was studied experimentally with a time-slicing 3D imaging technique.

DEDICATION

To my wife, Gamze and my daughter, Azra

Eşim Gamze ve Kızım Azra'ya

ACKNOWLEDGEMENTS

There are many people who have in part helped me through my graduate career here at Texas A&M University and deserve much recognition. I would like to thank my advisor, Hans A. Schuessler, for providing me with the opportunity to become successful, for sharing with me his knowledge, and for many fruitful and stimulating discussions.

I would like to thank my committee members, Dr. Siu A. Chin, Dr. Dong H. Son, and Dr. Alexandre A. Kolomenskii, for their guidance and support throughout this research. I would like to thank Dr. James Strohaber for detailed discussions and assistance related to the research. I would also like to thank Dr. Hartmut Schroeder in the MPQ, in particular, for generously sharing with us his expertise in filamantation experiments.

I would like to thank all the people in the Attosecond and Few Cycle Laser Laboratory, and my fellow graduate students, Gamze Kaya, Francisco Pham, Nathan Hart, Cade Perkins, Rocardo Nava, Muhammed Sayrac, and Feng Zhu. Thanks also go to my friends and all other colleagues and the department faculty and staff for making my time at Texas A&M University a great experience.

I am deeply grateful to my family for their great care, support and love. Finally, I would like to give my special thanks to Gamze for coming into my life. There are no words to convey how much I love her. She has been a true and great supporter and has unconditionally loved me during my good and bad times. I wish I could thank her enough for her everlasting love and kindness, and for her all optimism, encouraging support and patience.

NOMENCLATURE

ATI	above-threshold ionization
ATD	above-threshold dissociation
U_a	acceleration voltage in ion source
l	azimuthal mode numbers
a_0	beam radius at 1/e
w_0	beam waist at $1/e^2$
CCD	Charge-Coupled Device
CGH	Computer Generated Hologram
P_{crit}	critical power of self-focusing
E_{diss}	dissociation energy
E_{υ}	energy of vibrational levels
fs	femtosecond
$E_{\mathrm{HG}_{n,m}}$	field amplitude of the Hermite-Gaussian modes
$E_{\mathrm{LG}_{l,p}}$	field amplitude of the Laguerre-Gaussian modes
FWHM	full width at half maximum
φ_G	gouy phase
H_n	Hermite Polynomials with n mode number
$\mathrm{HG}_{n,m}$	Hermite-Gaussian mode with n and m mode numbers
E_{Diss}	kinetic energy of the fragments H and H^+
$\mathrm{LG}_{p,l}$	Laguerre-Gaussian mode with radial mode numbers *p* and azimuthal mode numbers *l*

I	laser beam intensity
w	laser beam radius (at 1/e^2)
ν	laser field frequency
λ	laser field wavelength
n_0	linear refractive index
LCOS-SLM	Liquid Crystal on Silicon-Spatial Light Modulator
LC-SLM	Liquid Crystal-Spatial Light Modulator
n	mode numbers in x direction
m	mode numbers in y direction
υ	molecular vibrational level
MCP	multichannel plate
n_2	nonlinear coefficient
1D	one-dimensional
P	peak power
τ	pulse duration
p	radial mode numbers
$R(z)$	radius of curvature
z_0	Rayleigh range
Γ	retardation function for 1D SLM
L_{sf}	self-focusing length
3D	three-dimensional
T	transmission

2D	two-dimensional
U	voltage function for 1D SLM
WLG	white light generation
J_0	zero order Bessel function

TABLE OF CONTENTS

Page

ABSTRACT ii

DEDICATION iii

ACKNOWLEDGEMENTS iv

NOMENCLATURE...v

TABLE OF CONTENTS viii

LIST OF FIGURES..xi

CHAPTER I INTRODUCTION 1

1.1 Motivation...1
1.2 Summary of dissertation 3

CHAPTER II GENERAL DESCRIPTION OF RESEARCH INSTRUMENTATION 5

2.1 Laser systems 5
   2.1.1 Millenia V 5
   2.1.2 Kapteyn-Murnane (KM) oscillator 5
   2.1.3 Evolution 15...6
   2.1.4 Spitfire (Regenerative amplifier) 7
2.2 Pulse measurement 9
   2.2.1 Frequency Resolved Optical Gating (FROG) – GRENOUILLE 9

CHAPTER III IN SITU BEAM CHARACTERIZATION OF FEMTOSECOND OPTICAL BEAMS WITH A HOLOGRAPHIC KNIFE-EDGE 11

3.1 Introduction...11
3.2 Holography 14
   3.2.1 Spatial Light Modulator (SLM) 17
3.3 Equivalence between holographic and mechanical knife-edge methods.........23
3.4 Experimental setup 27
3.5 Knife-Edge equations for the Hermite-Gaussian beams.................................30
3.6 Knife-Edge equations for the Laguerre-Gaussian beams 35
3.7 Tomographic reconstruction 41
3.8 Conclusions...43

CHAPTER IV WHITE-LIGHT GENERATION USING SPATIALLY-STRUCTURED BEAMS OF FEMTOSECOND RADIATION 44

4.1 Introduction 44
4.2 Experimental procedure 47
  4.2.1 Liquid Crystal -Spatial Light Modulator (LC- SLM) 47
  4.2.2 Experimental formation of HG beams 50
  4.2.3 Calculations for HG modes: Apertures with phase changes 54
  4.2.4 Experiments on white-light generation of HG beams in water 57
4.3 Discussion 58
4.4 Conclusion 61

CHAPTER V WHITE-LIGHT GENERATION CONTROL WITH CROSSING BEAMS OF FEMTOSECOND LASER PULSES 63

5.1 Introduction 63
5.2 Experimental setup 65
5.3 Results 66
5.4 Discussion 74
5.5 Conclusion 76

CHAPTER VI FILAMENT PROPAGATION LENGTH OF FEMTOSECOND PULSES WITH GAUSSIAN AND BESSEL BEAM MODES 78

6.1 Introduction 78
6.2 Experimental details and results 80
6.3 Conclusion 90

CHAPTER VII TIME-SLICED 3D MOMENTUM IMAGING OF H_2^+ PHOTODISSOCIATION 91

7.1 Introduction 91
7.2 Photodissociation of the hydrogen molecular ion 93
7.3 Ion beam apparatus 96
7.4 Result and discussion 102
7.5 Conclusion 104

CHAPTER VIII OVERALL CONCLUSIONS 106

REFERENCES 109

APPENDIX A 121

APPENDIX B 125

APPENDIX C 134

APPENDIX D 135

APPENDIX E...150

LIST OF FIGURES

Page

Figure 2.1 The outline of the Ti:sapphire femtosecond oscillator (KM oscillator). M1, M2, M3, M4, M5 are the cavity mirrors, where M3 is at the same time the output coupler. The group velocity dispersion experienced by the laser pulse traveling inside the crystal is compensated by a pair of prisms P1 and P2. 6

Figure 2.2 Schematic of regenerative cavity 7

Figure 2.3 The outline of the laser system: Ti:sapphire femtosecond oscillator (KML oscillator) is pumped by a CW optical power of 4.5 W at 532 nm wavelength from Millenia V. Seed femtosecond pulses (800 nm, 35 fs, 80 MHz, 400 mW) are amplified by Ti:Sapphire regenerative amplifier (including stretcher, regenerative cavity, and the compressor), which is pumped by a Q-swithed Nd:YAG laser (10 W at 532 nm, 10 ns, 1 kHz). 8

Figure 2.4 (a) Optical scheme of SHG FROG. (b) GRENOUILLE is the simplest version of the FROG. 10

Figure 3.1 Plane wave illuminates a highly transmissive object from the left. Two wavefronts are emitted from the object: and attenuated version of the incident plane wave and a scattered wave. The attenuated wavefront interferes with the scattered wavefront and the interference pattern is recorded on film. To get an image of the object the film is illuminated with a plane wave. Three beams result from the hologram, a specularly transmitted beam, a real image, and a virtual image. The figure is adopted from Ref [81]. 15

Figure 3.2 The LCOS chip has a parallel-aligned nematic liquid crystal layer to modulate light. It only changes the phase of light without any change of intensity and rotation of polarization state. Phase modulation is changed according to the alignment of the LC. The LC alignment is controlled, pixel by pixel, using a CMOS backplane and a DVI signal via a PC. The figure is adopted from Ref [82]. 18

Figure 3.3 (a) Measured output power of a Michelson interferometer versus modulation depth (blue squares). The SLM was positioned in one arm of the interferometer and introduced a phase-modulation encoded as a grayscale value. The solid curve is the theoretically expected result. (b) Phase modulation retrieved from the data and theoretical curve shown in panel (a). 19

Figure 3.4 (a) Illustration of a blazed phase grating having modulation depth m and spatial Λ period displayed on the SLM. (b) Blazing efficiency as a function of modulation depth measured as the ratio of the power in the first diffraction order to that in the zero order. Nine sets of data were obtained each having a different grating period and denoted by the number of pixels (np) used for the grating period. Each pixel is assumed to be equal to the pitch, which is 20 µm. All data sets show a peak at a grayscale value of ~100, which corresponds to a phase shift of 2π radian. The inset in panel (b) shows the efficiencies for the peak values (grayscale value of 100) demonstrating the best achieved diffraction efficiency for a grating period of 8 pixels. 22

Figure 3.5 (a) Illustration of a hologram used to create a holographic knife-edge. The solid black color on the left side of hologram denotes a constant phase modulation and the right side of the hologram is that of a blazed grating. (b) Measured power as a function of knife-edge position. The black crosses represent the measured power from a mechanical knife-edge position at the location of the SLM, and the red circles are that obtained from the holographic knife-edge. Both mechanical and holographic knife-edge measurements are in good agreement. The insets are fits of the data to theoretical curves. 24

Figure 3.6. Experimental setup. Laser radiation from either a He-Ne or Ti:sapphire laser enters the setup from the right. DL = 50 cm diverging lens, CL = 200 cm converging lens, SLM = spatial light modulator, FM = folding mirror placed a distance of f =100 cm away from the SLM, PD = photodiode power meter head, PM = power meter. The upper left inset is an example hologram to create a $\mathrm{LG}^{o}_{2,2}$ beam followed by an angular knife-edge. 28

Figure 3.7 Intensity profiles of a $\mathrm{LG}^{o}_{2,2}$ beam being azimuthally knife-edged. (a) This sequence of frames shows the holograms used to perform an angular knife-edge measurement with an angular step size of 90 degrees. (b) CCD images of radiation from a He-Ne source after passing through the corresponding grating in sequence (a). Each frame shows both the zero and first diffraction orders. As the area of constant phase (denoted by the blackened areas in (a)) increases, the corresponding local radiation in the first diffraction order is directed into the zero order until the radiation is gone. 30

Figure 3.8 Cartesian knife-edge measurements of the Hermite-Gaussian modes. The modality of each mode is given as the label of the panel. The black opened squares are data taken from knife-edge measurements in the *x* direction and the black opened circles are that in the *y* direction. The number of plateaus is equal to the mode number. The red curves were obtained by fitting the data with theoretical curves presented in the text. From this fit the beam size was determined. 35

Figure 3.9 Radial knife-edge measurements for an assortment of helical Laguerre-Gaussian beams. The number of plateaus is equal to the radial mode number p. The waist of the beams can be determined by fitting the data to the theoretical equations given in the text. The fits are shown by the solid red curves. Unlike the HG beams, the radial knife-edge measurements depend on both radial and azimuthal mode numbers *p* and *l*. The dependence of the curve on the azimuthal mode number can be seen by the size of the initial plateau increasing from the leftmost column to the rightmost column. 38

Figure 3.10 Angular knife-edge measurements for an assortment of even LG beams having modalities as indicated. The number of plateaus is equal to twice the angular mode number $2l$. The waist of the beam cannot be determined from an angular knife-edge measurement, but this measurement can give an indication of the quality of the modal lobes. 40

Figure 3.11. Tomographic reconstruction of a femtosecond $\mathrm{LG}_{p=1}^{l=1}$ beam in a folded-2f setup. All images are 200-by-200 pixels and have the same vertical and horizontal scaling. The dimension of the images is given by the scale in panel (a). (a, c) Raw double-knife-edge data recorded by stepping a knife-edge in one direction (i.e., x) by a single step, completing a full knife-edge in the other direction (i.e., y), and repeating this process until finished. The raw data shown in panel (a) is that obtained by not correcting for angular dispersion in the folded-2f setup, while that in panel (c) has been corrected. Panels (b) and (d) were obtained by taking the partial derivatives (see text) of the measured double-knife-edge power. 42

Figure 4.1. Measured transmission signal with crossed polarizer...................................49

Figure 4.2. Typical phase modulation dependence. 50

Figure 4.3 Experimental setup to generate HG modes with the 1D SLM and for studies of white-light generation of HG beams in water. Laser radiation from the Ti:sapphire laser enters the setup from the left. Blue arrows (E) show the initial polarization of the beam and the changes of this polarization after the passage of the periscope P1 and a ($\lambda/2$) wave plate (WP). Other optical components used: P2-periscope to adjust the beam height, SLM - spatial light modulator, FM - folding mirror. Notice that in P1 the mirrors are rotated relative to each other in the horizontal plane by 90°, while in P2 the mirrors are parallel. The incident HG beam enters a 40mm long cuvette (C). A CCD camera for taking images is first placed at position 1 on the entrance of the cuvette to record the generated HG beam. Then the camera is placed at position 2 to record the generated white light on a frosted paper screen (FP) after the radiation of the pump beam is reflected by an 800nm dielectric mirror (DM). The colored picture of $\mathrm{HG}_{1,1}$

taken by a color digital camera at position 2 shows the strong white cores with colorful rings (conical emission) in the lower right inset. (a), (b), (c), and (d) present grey-scale encoded phase masks to create $HG_{0,0}$, $HG_{0,1}$, $HG_{1,0}$ and $HG_{1,1}$ beams, respectively. 53

Figure 4.4 The measured distributions of the laser intensity in the $HG_{0,0}$, $HG_{0,1}$, $HG_{1,0}$ and $HG_{1,1}$ beams. Each laser distribution has been peak normalized. HG beams in panels (a-d) are created with the phase masks (a-d) as shown in the inset of Fig. 4.3. 55

Figure 4.5 The normalized distributions of the laser intensity in the cases of $HG_{0,0}$, $HG_{0,1}$, $HG_{1,0}$ and $HG_{1,1}$ beams calculated by the integrals with appropriate phase factors (Eqs.(4.7)). 56

Figure 4.6 The measured white-light intensity distributions on the CCD for all HG modes generated at the fixed geometry. 58

Figure 4.7 The top view of the experimentally measured distributions of the laser intensity for the $HG_{0,0}$, $HG_{0,1}$, $HG_{1,0}$ and $HG_{1,1}$ beams from panels (a − d) of Fig. 2 . The intensity lobes used for the calculation of the critical power and self-focusing distance of HG beams (main lobes) are shown with black solid circles in panels (a − d), drawn at FWHM values of the peak intensity; the dotted lines show the same for other peaks in the intensity distributions... 60

Figure 5.1 Experimental setup: the delay between pulses in two optical arms is changed by a translation stage. The two beams cross in the sample. An input aperture was used for adjusting the power of the beams; a typical diameter of the aperture is 2.7 mm for beams producing filamentation in our case. The first incoming mirror is curved with the focal length 2.5 m. A dielectric mirror separates as shown in the inset an IR radiation around 800 nm and generated white-light, which were measured or imaged on a CCD camera depending on the delay between optical paths in two arms. Shown are: CM -curved mirror, BS - beam splitter, TS - translation stage, M1- M6 fast silver mirrors, DM - dielectric mirror. 66

Figure 5.2 Images of beam cross-sections with filaments taken with 6.6 fs intervals of time delays increasing from top to bottom and from left to right: left panel shows the whole series of images; the right panel shows a magnified view of the area in the red rectangle, where light produced by separate filaments can be discerned. 67

Figure 5.3 Variations of the white-light vs. relative delay of two beams; upper trace (blue) is the total amount of white light measured in both arms, the black trace is the power measured in the fixed arm, and the red trace is the power measured in the movable arm. 69

Figure 5.4 Spectral observation of white-light enhancement and suppression: the upper graph shows in false colors a plot of the spectral distribution of the two beams in the range 400-700 nm after their interaction in the sample as a function of the relative delay; the lower graph depicts the total (integrated) amount of white light also vs. time delay. An enhancement of the spectral components at negative delays and for positive delays and a strong suppression of the spectrum near zero delay can be clearly seen, which result also in the integrated white-light variations (lower graph). 70

Figure 5.5 IR beams after interaction: right panel shows a magnified view of the images of the cross sections of beams on the CCD camera in the movable arm (top) and in the fixed arm (bottom) at zero delay; left panel shows the dependence of the measured power in the circled areas vs. delay in movable and fixed arms (the curves shifted up for better viewing). The bottom panel shows images taken at large delays (1, 5), at delays corresponding to maximal white-light output (2, 4) and zero delay (3). The starting points of arrows indicate respective delays on the time scale. 71

Figure 5.6 The dependence of the IR power on delay and images of the IR beams with the central parts blocked taken at large delays (1, 5), at delays corresponding to maximal white-light output (2, 4) and zero delay (3). The starting points of arrows indicate respective delays on the time scale. 72

Figure 5.7 Variations of the IR radiation in the central spot of the fixed arm for different angles between polarizations of the beams in the two arms. The curves are shifted vertically for better viewing. 73

Figure 6.1 Experimental setup: SLM, spatial light modulator; SP, syringe pump; GC, glass cell with an optical window; FG, flat glass (4% reflectivity at 45 deg.); IR-F or ND-F, infrared filter or neutral density filter to measure the incident beam; PM, power meter; IC, integrated cavity; SM, spectrometer. The inset under the SLM is an example hologram used to create a Bessel-Gaussian beam. The other inset shows image of a Bessel-Gaussian beam with filaments core taken a color CCD camera with necessary filters and attenuators. 81

Figure 6.2 Optical filters selectively transmitted light having certain a particular range of wavelengths. 82

Figure 6.3 Spectral profiles of the (a) Gaussian beam and (b) Bessel-Gaussian beam measured over the central lobes as a function of the propagation distance. The corresponding experimentally created input beam modes are shown in the right panel. 83

Figure 6.4 Measured IR distributions of the laser intensity in the (a) Bessel-Gaussian and (b) Gaussian beams at the different propagation distances........................85

Figure 6.5 Experimentally created modes of the incident Bessel-Gaussian beam: (a) central peak of the beam with no lobes and (b-h) central peak with additional radial lobes..86

Figure 6.6 Spectra of the central lobe of the Bessel-Gaussian beams with different number of radial lobes and measured as a function of the propagation distance. 88

Figure 6.7 Average IR power measured for the central peak of the Bessel-Gaussian beam with the different number of radial lobes as a function of the propagation distance. 89

Figure 7.1 Potential energy curves of the two lowest states of hydrogen molecular ion in a weak field [178]. 94

Figure 7.2 Potential energy curves of the photon dressed states. At $I>10^{12}$ W/cm^{2} the coupling between the ground $1s\sigma_g$ and the first excited state $2p\sigma_u$ becomes very strong [178]...95

Figure 7.3 Layout of the ion beam apparatus. DP: deflection plates (13mm x 22.5mm x 0.85mm); EL: Einzel lenses; SM: sector magnet, R=150, B=10G, 8A, A: apertures; A3: 60mm circular plate with 2mm circular hole, A4: 60mm x 60mm square plate with 300μ circular hole, A5: 8mm circular hole, A6: 60mm x 60mm square plate with 3mm circular hole, A7: 25 x 200 slit and 1mm x 1mm square hole , IA, ion accelerator, S: vertical slit 0.75mm Gap, IG: Ion gate 92mm x 40mm high deflection plates with 5mm separation, L: focusing lens; FC: Faraday cup; MCP: microchannel plate detector. Inset (a) Interaction volume defined by the intersection of a laser beam (shown as a cylinder) and an ion beam (box). Inset (b) shows schematic diagram of the geometry employed for collimation along the x axis. 97

Figure 7.4 (a) Schematic view of the spectrometer, (b) after applying ion accelerator voltage +750V for Δt=60ns separation, TOF spectrums of the neutral and charged fragments resulting from the photodissociation of H_2^+ (upper graphs), related accumulated frames of the fragments for TOF between 220ns-340ns, 220-280 ns and 280-340ns (lower graphs). 1pixel=25μm. 101

Figure 7.5 Time-of-flight spectrum of fragments from H_2^+ photo-dissociation. No voltage was applied to the electrostatic spectrometer....................................103

Figure 7.6 Series of time slices (10 ns intervals between 197 ns and 274 ns) through the H_2^+ momentum distribution. The momentum distribution of the center slice (230 ns–240 ns) is clearly sharper than the momentum distribution of the full data set (197 ns-274 ns)..104

CHAPTER I

INTRODUCTION

1.1 Motivation

When a matter is exposed to an intense ($I > 10^{13}$ W/cm^2) laser field, it exhibits highly nonlinear dynamics that has held a great deal of promise in many fields and led to the observation of phenomena such as high order harmonic generation (HHG) [1-5], attosecond pulses generation [6-9] , above-threshold ionization (ATI) (i.e.absorption of more photons than the minimum number required for ionization) [10-13], white-light (supercontinuum) generation, [14-25], and filamentation [26-35]. In the recent studies, researchers therefore have been trying to gain optimal controls over laser-matter interactions to a desired outcome via manipulating different laser parameters, such as peak intensity [36-39], wavelength [36,40-42], pulse length [37,38,43,44], pulse shape [36,45], or carrier-envelope phase [46-50].

In the center of these efforts, there are strategies that provide extended nonlinear propagation under controlled conditions, as applied to filaments [29,51,52] or individual sources of white-light. This phenomenon has been the subject of active research motivated by various potential applications such as remote spectroscopy [53], generation of few-cycle optical pulses [54], lightning control [55], and generation of THz radiation [56].

In this work supercontinuum (white light) generation, filamenation, and photo-dissociation are extensively studied. An in situ beam characterization technique, which makes use of a two-dimensional spatial light modulator (SLM) to holographically redirect radiation between different diffraction orders with the aim to analyze femtosecond optical beams is presented. By creating and employing the laser beams with spatially modulated phase and amplitude, we studied the production and control of white-light generation and filamentation in transparent media. These research went in the following directions: (i) white-light generation using spatially-structured beams of femtosecond radiation, (ii) study of filament propagation length of femtosecond pulses with these different transverse modes, and (iii) white-light generation control with crossing beams of femtosecond laser pulses. Additionally, the development of ion detection system with both fast timing and simultaneous two-dimensional position determination capabilities provided new insights in the understanding of nonlinear molecular dynamics related to photoionization and photodissociation processes. In experimental study of dissociation processes, it is now possible to measure the 3D (three-dimensional) momentum vector with high resolution and efficiency for each charged fragment by combining large-diameter MCP (microchannel plate) detectors with delay-line anodes [57-59]. As a first step of coherent control and manipulation of the interaction of femtosecond radiation with H_2^+, we obtained a clear picture of the photodissociation process of H_2^+ with central wavelength 800 nm, 50 fs laser pulses in our ion beam apparatus by employing the time-sliced 3D imaging technique.

1.2 Summary of dissertation

Chapter II: This chapter gives detailed information about femtosecond laser systems and the pulse measurement techniques that we used. The main focus of this chapter is on the laser system.

Chapter III: By reviewing of Gabor and Leith-Upatneik holography, this chapter starts with the method that was used to encode phase and amplitude information onto phase-only hologram and provides a detailed description of in situ beam characterization technique to analyze femtosecond optical beams. This technique employs a spatial modulation of the phase and amplitude by using a two-dimensional spatial light modulator (SLM). The chapter ends with testing our method by holographically knife-edging and tomographically reconstructing both continuous wave and broadband radiation having various transverse optical modes.

Chapter IV: This chapter is a synopsis of study on white-light generation and control using spatially-structured beams of femtosecond radiation. One of the subjects of this chapter is how to create a Hermite-Gaussian (HG) beam by using a one-dimensional spatial light modulator (SLM). By briefly reviewing the role of self-focusing in white-light generation, the self-focusing lengths of the different realized transverse intensity profiles were calculated to qualitatively explain the white-light production. Also, distributions of the laser intensity for beams having step-wise spatial phase variations were modeled using the Fresnel-Kirchhoff integral in the Fresnel approximation.

Chapter V: In this chapter, the effects of two-beam interaction in white-light generation were investigated. By varying the relative delay of two interacting intense femtosecond laser pulses, the white-light was generated and manipulated. The effects of the two-beam interaction on the generated white light and pump beams are discussed.

Chapter VI: This chapter describes first the application of the holographic method, used to create Gaussian and Bessel-Gaussian beams with the same peak intensity, pulse duration and the size of the central part of the beams. The comparison of the filament propagation lengths of femtosecond pulses with these different transverse modes is given. This is followed by a more detailed study of the dependence of the filament propagation length on the number of radial modal lobes to better understand the Bessel-Gaussian beam propagation.

Chapter VII: This chapter gives a detailed information on the ion beam apparatus. For our long term goal of studying H_2^+ and its interaction with a white-light source in the ion beam apparatus, we performed a study of the photo-dissociation of H_2^+ with 800nm femtosecond radiation. The reconstruction of the laser-induced fragment momentum distribution in photo-dissociation of H_2^+ was shown experimentally by employing a time-sliced 3D imaging technique to obtain a clear picture of the photo-dissociation process in the ion beam apparatus.

Chapter VIII: The chapter gives the summary of the research work carried out in the dissertation.

CHAPTER II

GENERAL DESCRIPTION OF RESEARCH INSTRUMENTATION

The main focus of this chapter is on the laser system and the pulse measurement techniques used in measurements.

2.1 Laser systems

Our laser system includes four interrelated lasers. We labelled them by the manufacturer as Millenia V, Kapteyn-Murnane (KM oscillator), Evolution laser and Spitfire (regenerative amplifier).

2.1.1 Millenia V

The Millennia V is a solid-state, high power, continuous wave (CW) laser that supplies more than 5 W of green 532 nm output, which is obtained by intracavity doubling the frequency of a diode pumped Nd:YAG laser. The frequency doubling is done by a temperature tuned lithium triborate (LBO) crystal. In our system, Millennia V is used to pump the femtosecond Kapteyn-Murnane (KM) oscillator at a continuous optical power of ~4.4 W at 532 nm wavelength.

2.1.2 Kapteyn-Murnane (KM) oscillator

KM is a mode-locked Ti:Sapphire femtosecond oscillator pumped by Millennia V. To achieve the Kerr lens effect, concave mirrors are used which form the telescope with the crystal in the focal plane. In Figure 2.1, Ti:Sapphire femtosecond oscillator is shown, where M1, M2, M3, M4, M5 are the cavity mirrors, and M3 is also the output mirror. The group velocity dispersion experienced by the laser pulse traveling inside the crystal is compensated by a pair of prisms P1 and P2. The output of the oscillator is a train of pulses emitted in the spectral range from 780 nm to 830 nm; the pulse duration is about 35 fs, the repetition rate is close to 80 MHz, the energy ~5 nJ/pulse and the average power is about 400 mW.

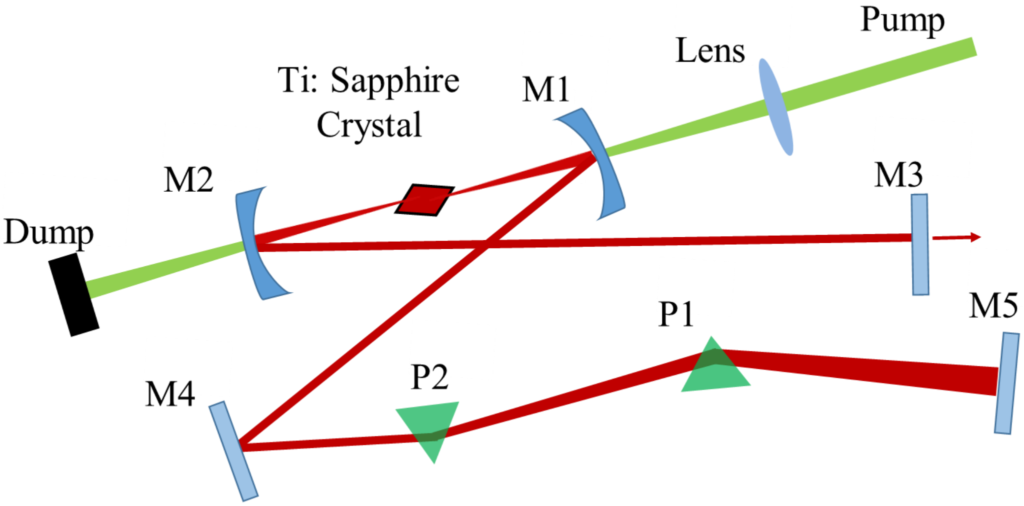

Figure 2.1 The outline of the Ti:sapphire femtosecond oscillator (KM oscillator). M1, M2, M3, M4, M5 are the cavity mirrors, where M3 is at the same time the output coupler. The group velocity dispersion experienced by the laser pulse traveling inside the crystal is compensated by a pair of prisms P1 and P2.

2.1.3 Evolution 15

Evolution is a Q-switched Nd:YAG laser (Spectra Physics, Merlin) at a repetition rate 1 kHz, output power 10 W at 532 nm wavelength with ~10 ns pulse duration. The gain medium and pump lasers are enclosed inside the laser head and co-located in a directly water cooled resonant cavity. The Evolution is used to pump the spitfire.

2.1.4 Spitfire (Regenerative amplifier)

The regenerative amplifier technique is used to amplify femtosecond pulses. In our system (Figure 2.2) [60] it is used to amplify seed pulses (KM Oscillator) that follow with a repetition rate around 80 MHz. The amplifier is pumped by the Evolution laser that has a repetition rate of 1 kHz. Thus, only a small part of the pulses from the oscillator is amplified. The seed pulse is inside the laser cavity when the pump pulse passes through the crystal. When the gain is saturated, the amplified pulses are let out of the cavity. For this reason a fast optical switch that has a response time in the nanosecond range is required.

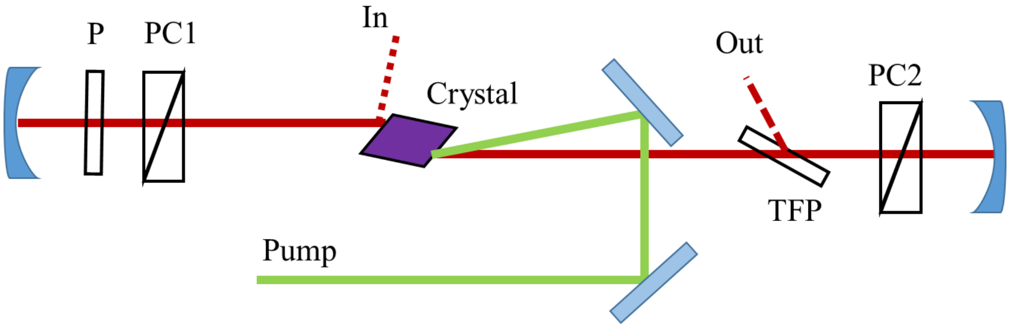

Figure 2.2 Schematic of regenerative cavity

Our Spitfire contains three main parts: stretcher, regenerative cavity and compressor. First, the seed pulses are expanded in the stretcher. A photodiode that is placed behind one of the cavity mirrors helps to monitor the trace of the femtosecond pulses on the oscilloscope. The Pockels cell changes the refractive index of the material under the applied electric field and consequently the polarization, so that an amplified linearly polarized pulse is let out of the cavity. The output of the amplifier is a train of the pulses having average power ~900 mW, repetition rate 1 kHz, pulse energy 0.9 mJ and pulse duration 50 fs. Figure 2.3 depicts the layout of the laser system.

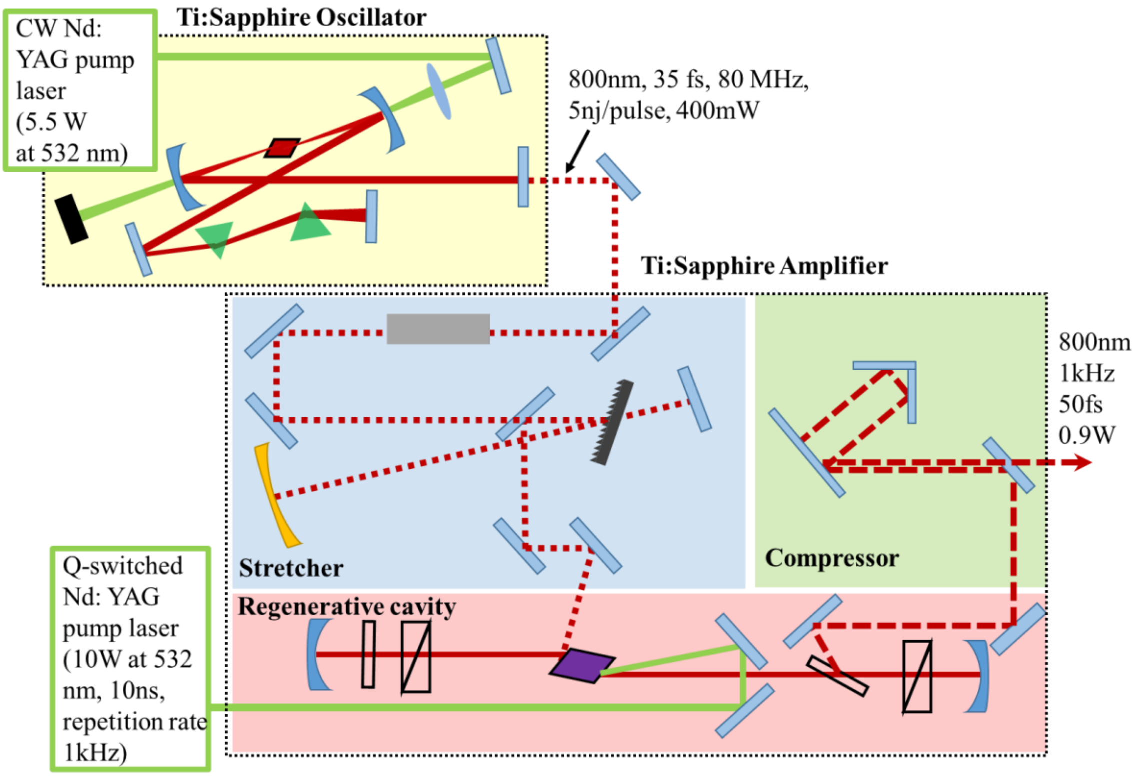

Figure 2.3 The outline of the laser system: Ti:sapphire femtosecond oscillator (KML oscillator) is pumped by a CW optical power of 4.5 W at 532 nm wavelength from Millenia V. Seed femtosecond pulses (800 nm, 35 fs, 80 MHz, 400 mW) are amplified by Ti:Sapphire regenerative amplifier (including stretcher, regenerative cavity, and the compressor), which is pumped by a Q-swithed Nd:YAG laser (10 W at 532 nm, 10 ns, 1 kHz).

2.2 Pulse measurement

2.2.1 Frequency Resolved Optical Gating (FROG) – GRENOUILLE

Frequency resolved optical gating (FROG) helps researchers characterize the pulses in the temporal domain. FROG has the ability to measure femtosecond pulse's spectral intensity vs. time. The FROG setup is shown in Figure 2.4; it consists of an auto-correlation unit and a spectrometer. For autocorrelation the laser pulse is split into two replicas, with one delayed with respect to the other; then both are focused and recombined on a nonlinear Second Harmonic Generation (SHG) crystal. The SHG crystal produces twice the frequency of the input laser, and the spectrometer determines the shape and the phase of the laser pulse. The described FROG update is called GRENOUILLE by Trebino et al. [61,62]. In this device the beam splitter, delay line and beam combining optics is replaced with a Fresnel biprism and a thick SHG crystal. Thus, GRENOUILLE is a combination of two cylindrical lenses, Fresnel biprism, and an SHG crystal. The first lens focuses the beam into the SHG crystal, the Fresnel biprism splits the beam, and delays one pulse relative to the other, and the second lens focuses the beam onto a CCD camera. In Figure 2.4 we show the results of the measurements with the Grenouille (8-20, Swamp Optics).

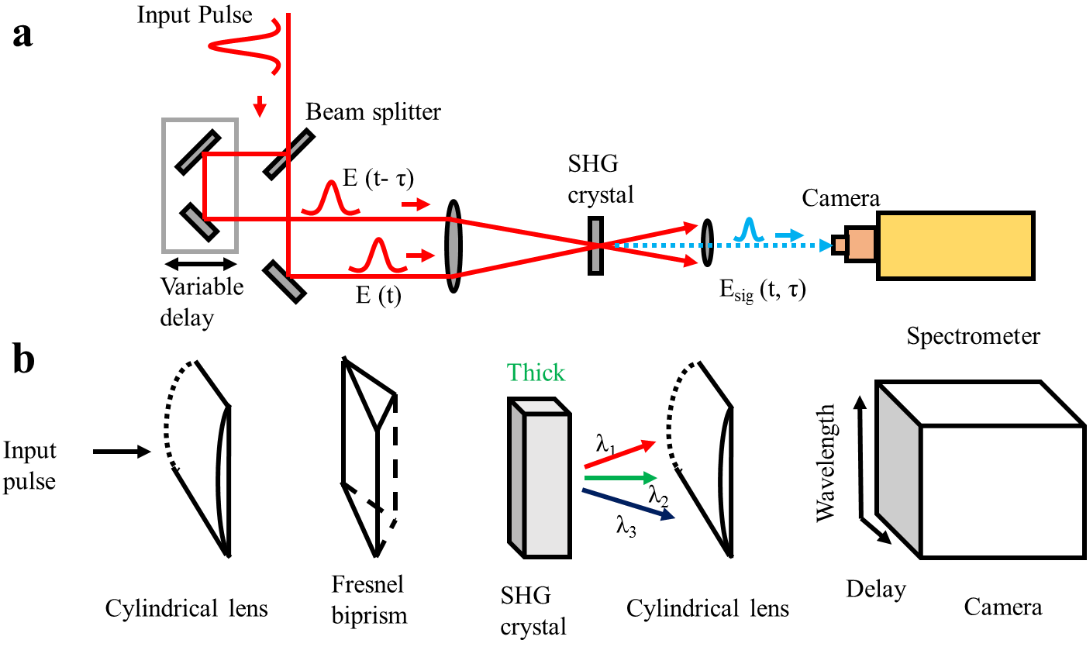

Figure 2.4 (a) Optical scheme of SHG FROG. (b) GRENOUILLE is the simplest version of the FROG.

CHAPTER III

IN SITU BEAM CHARACTERIZATION OF FEMTOSECOND OPTICAL BEAMS WITH A HOLOGRAPHIC KNIFE-EDGE[1]

In this Chapter, we present an in situ beam characterization technique to analyze femtosecond optical beams in a folded version of a 2*f*-2*f* setup [63]. The chapter starts with reviewing of Gabor and Leith-Upatneik holography and then describes a method to encode phase and amplitude information onto phase-only hologram and provides a detailed description of in situ beam characterization technique to analyze femtosecond optical beams. This technique employs a spatial modulation of the phase and amplitude by using a two-dimensional spatial light modulator (SLM). The chapter ends with testing our method by holographically knife-edging and tomographically reconstructing both continuous wave and broadband radiation with various transverse optical modes.

3.1 Introduction

Optical beam modes have drawn considerable interest in the scientific community over the past few decades. These transverse optical modes, which are eigensolutions of the paraxial wave equation in different coordinate geometries, are represented by the Hermite-Gaussian, Laguerre-Gaussian and more recently the Ince-Gaussian beams. Radiation in these transverse modes have been used in a broad range of disciplines having

---

[1] This chapter is based on one of our published papers that appears as Appendix D : J. Strohaber, G. Kaya, N. Kaya, N. Hart, A. Kolomenskii, G. Paulus, and H. Schuessler, "In situ tomography of femtosecond optical beams with a holographic knife-edge," Optics Express 19, 14321-14334 (2011). doi.org/10.1364/OE.19.014321.

applications in the optical manipulation of atomic and molecular systems [64-66], optical vortex coronagraph for the direct imaging of exoplanets, thermal noise in gravitation wave interferometric antennas [67-69], ultrashort intense-field filamentation experiments [70], and optical trapping [71]. The Laguerre-Gaussian beams are of considerable interest, because radiation in these transverse modes carries, in addition to intrinsic angular momentum, a sharp quantized amount of optical orbital angular momentum equal to $\ell\hbar$, where ℓ is integer per photon. Recent theoretical work has suggested that this additional angular momentum can couple to the internal degrees of freedom of a molecular system in addition to external degrees of freedoms as in [66]. Our plans are to produce intense femtosecond optical vortices in a “pure” transversal mode such that the angular momentum per photon is sharp, i.e. beams, which are not in a superposition of eigenmodes having different angular momentum quantum numbers.

When producing optical beam modes, a common approach is to use gratings, where phase and amplitude information about the mode is encoded within the grating structure [72,73]. This approach works well when the light used is monochromatic [74], however, when a polychromatic light such as femtosecond radiation is used, a compensation technique is needed in order to correct for angular dispersion. This need for compensation has been met with a variety of successful experimental techniques [75-78]. In most of these experimental setups, a second dispersive optical element was used as the compensator. In this paper, we introduce a method for the in situ analysis of optical beams by using the needed second pass of the folded version of a 2*f*-2*f* setup (folded-2*f*) to “holographically knife-edge” optical beams, which were produced in the first pass of the setup [78]. As a note, in principle our technique can be used in a folded version of the 4f-setup [77]. The focusing element in the 2*f*-2*f* or folded-2*f* setup reverses the sign of the angular dispersion causing the dispersed broadband beam to exhibit a zero amount of *spatial dispersion* at the position of the second grating [76]. At all other positions within the setup, except at the position of the first grating, the beam will exhibit some degree of “blurriness” in the dispersion plane. Because of this —while the beam still exhibits *angular dispersion*—it is possible to knife-edge and tomographically reconstruct the beam it situ at the position of the second grating pass. Here we show how this can be carried out using holographic techniques.

There are several attractive aspects of this it situ beam characterization. Compared to CCD beam profilers and cameras, SLMs can withstand intensities of up to $I \sim 10^{11}$ W/cm^2, because laser radiation is transmitted instead of absorbed by them, and the active area of a SLM’s LCD is typically larger than that found for the CCD chips in beam profilers and cameras. Compared to mechanical knife-edge methods such as razor blades and irises (hard apertures), SLMs are highly flexible having no moving parts; multiple knife-edge directions can be performed without the need of a spinning drum perforated with holes. SLMs can be used to generate complex two-dimensional shapes, and because their pixels are fixed, there is a high degree of reproducibility. We will show that SLMs can produce virtually any desired geometric aperture using its LCD (soft aperture). Furthermore, The SLM has a refresh rate of 60 Hz allowing for measurements to be taken in real time. In addition to tomographic reconstruction, a few beam characteristics such as the beam waist and the relative power between modal lobes can be determined by using only a few knife-edge measurements—as long as the beam is nearly ideal.

3.2 Holography

Holography was invented in 1947 by Dennis Gabor, and The Nobel Prize in Physics 1971 was awarded to him "for his invention and development of the holographic method" [79]. The discovery was an unexpected result of research into improving electron microscopes. The technique as originally invented is still used in electron microscopy, where it is known as electron holography, but optical holography did not really advance until the development of the laser in 1960. Hologram literarily means “whole writing”. Gabor holography is also known as on-axis holography. The light emitted by an object contains both a phase and an amplitude. In principle, if one could reproduce the phase and amplitude of the emitted light then an image of the object could be artificially produced. This was originally carried out by recording the interference pattern of an object wave with a reference wave onto photographic film [80,81]. Figure 3.1 shows a setup used to record an on-axis hologram. When a coherent source illuminates a highly transmissive object (from the left in Figure 3.1), two transmitted wavefronts result on the right of the object. The first wave is an attenuated version of the source light, and the second is a scattered wave from the object. The transmitted wave possesses a flat wavefront and is referred to as the reference wave E_R . The scattered E_O wave contains phase and amplitude information about the object. The interference pattern produced by the interference of these two wavefronts is recorded onto photographic film. The intensity of the interference pattern is,

$$I(x,y) = \left|E_O(x,y) + E_R\right|^2 = \left|E_R\right|^2 + \left|E_O\right|^2 + E_O^* E_R + E_O E_R^* \tag{3.1}$$

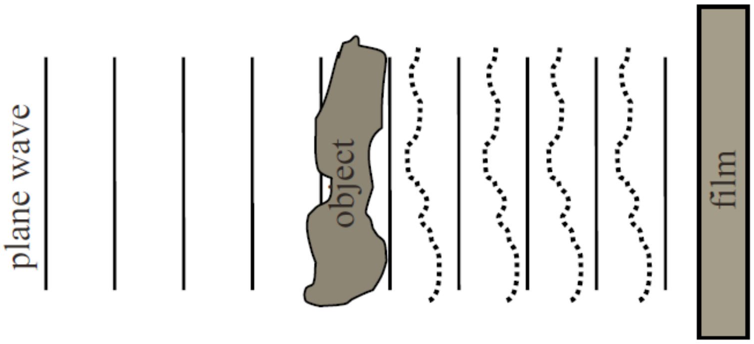

Figure 3.1 Plane wave illuminates a highly transmissive object from the left. Two wavefronts are emitted from the object: and attenuated version of the incident plane wave and a scattered wave. The attenuated wavefront interferes with the scattered wavefront and the interference pattern is recorded on film. To get an image of the object the film is illuminated with a plane wave. Three beams result from the hologram, a specularly transmitted beam, a real image, and a virtual image. The figure is adopted from Ref [81].

The first term is a DC offset, the second term is small and contains amplitude information of the object, and the last two terms encode for the phase of the object in the form of interference fringes. To reconstruct an image of the object from the developed film, the film is illuminated with a normally incident plane wave having a uniform amplitude. The resulting transmitted light suffers from a few limitations. First, there is a component of the plane wave which passes directly through the hologram, and second the third term in Eq. (3.1) gives rise to a virtual image. The virtual image is similar to the real image (arising from the fourth term in Eq. (3.1)) except that it is the complex conjugation of the real image. Therefore, the light passing through the hologram is the superposition of three wavefronts. In the context of this research, holography is used to create paraxial beam modes possessing, in the ideal case, no contaminants. Based on the above discussion, on-axis holography is not suitable for our purpose.

After the development of the laser in the early 1960s, Leith and Upatnieks [80] modified Gabor holography to remove the on-axis overlapping of the transmitted, virtual and real images. Instead of relying on a highly transmissive object to produce the reference wave they used a second source split from the first source. This allowed for the reference beam to interfere with the object wave at an oblique angle. Upon illuminating the hologram with a plane wave of uniform intensity the transmitted, virtual and real images no longer overlap. This method is known as off-axis holography and is the method used in this work to produce paraxial beam modes.

From the previous discussion of both on-axis and off-axis holography, a natural question arises: How do you make a hologram of an object, when you need the object to make the hologram? This vicious circular argument is solved by using a computer to generate the hologram and then by some means record the hologram on a medium. One way to record the computer-generated hologram (CGH) onto a medium is to print the CGH and take a picture of it. The negative can then be illuminated with a plane wave to produce the object encoded in the CGH [76]. A liquid crystal spatial light modulators (LC-SLM) and more recently liquid crystal on silicon-spatial light modulators (LCOS-SLM) have been used to display the CGH directly [63,73]. In most of this study, an optically addressed LCOS-SLM by Hamamatsu was used along with CGHs to generate paraxial beam modes.

3.2.1 Spatial Light Modulator (SLM)

The SLM (Hamamatsu LCOS-SLM X10468-02) used in this work was designed to function optimally for wavelengths within the range of 750 nm to 850 nm meaning that the antireflective coating and dielectric retroreflecting mirror (R>95%) are optimized for operation in this wavelength range. The X10468-02 is a reflective type of pure phase Spatial Light Modulators (SLMs), based on Liquid Crystal on Silicon (LCOS) technology in which liquid crystal (LC) is controlled by a direct and accurate voltage, and can modulate a wavefront of light beam (Figure 3.2). The LCOS-SLMs are carefully designed to achieve high light utilization efficiency from various points of view, such as reflectivity, aperture ratio and diffraction noise due to the pixel structure. The X10468 series can be controlled via a PC using the Digital Video Interface (DVI), which is a standard interface for computer displays. The distortions in the LCOS chip, such as wavefront distortion and nonlinear response of the LC, are efficiently compensated by the controller. Easy computer control, precise and linear phase modulation characteristics can be accomplished with the X10468 series. They can also provide high diffraction efficiency and high light utilization efficiency [82].

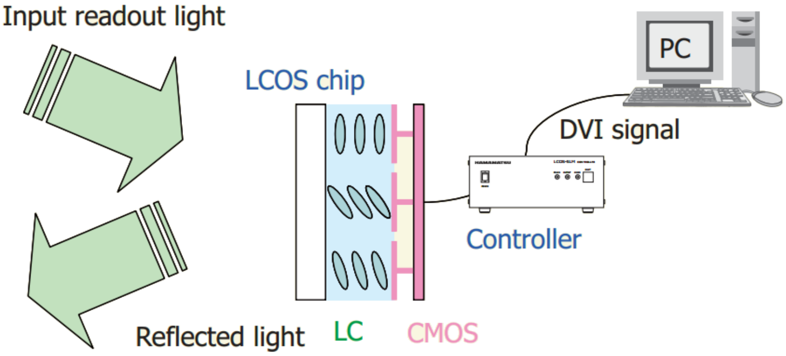

Figure 3.2 The LCOS chip has a parallel-aligned nematic liquid crystal layer to modulate light. It only changes the phase of light without any change of intensity and rotation of polarization state. Phase modulation is changed according to the alignment of the LC. The LC alignment is controlled, pixel by pixel, using a CMOS backplane and a DVI signal via a PC. The figure is adopted from Ref [82].

Some of our future goals involve the use of continuous wave radiation from a He-Ne source in addition to 800-nm femtosecond from a broadband radiation source. The difference in wavelength is expected to affect the reflectivity due to the spectral response of the SLM’s optics. In contrast to the programmable phase modulator (PPM) used in [76], the LCOS-SLM is a pixelated device, which consequently results in a loss of power due to parasitic diffraction effects. In all experiments carried out in this work, noticeable amount of light was observed in higher diffraction orders. For the above mentioned reasons, the reflectivity of the SLM for the He-Ne wavelength was determined by taking the ratio of the spectrally reflected (zero order) and incident laser powers when a constant phase modulation was displayed on the SLM's LCD (encoded in the grayscale value of a picture). The reflectivity was found to be $R \approx 76\%$.

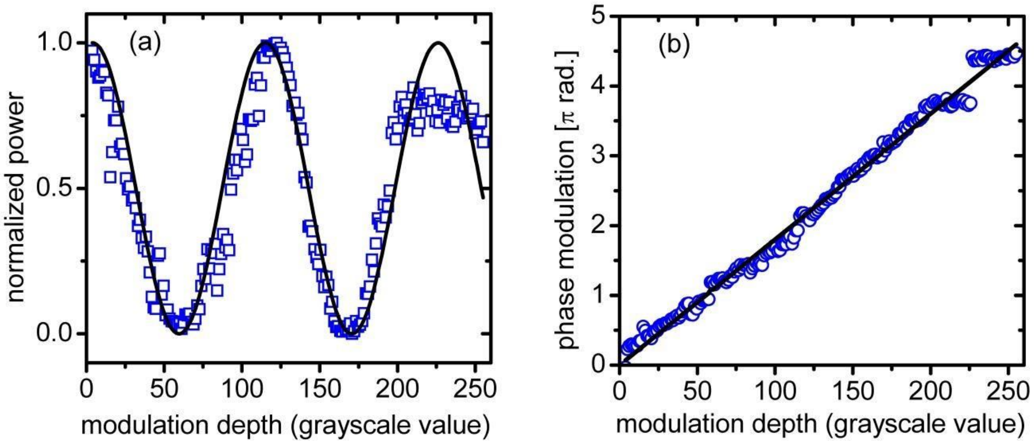

Figure 3.3 (a) Measured output power of a Michelson interferometer versus modulation depth (blue squares). The SLM was positioned in one arm of the interferometer and introduced a phase-modulation encoded as a grayscale value. The solid curve is the theoretically expected result. (b) Phase modulation retrieved from the data and theoretical curve shown in panel (a).

Besides the spectral response of the optical coatings, another consideration is the induced phase modulation as a function of the applied voltage or programmed grayscale value when using 633 nm radiation instead of 800 nm. The phase modulation of the SLM was factory-calibrated using 800 nm and was shown to produce over 2π radians of phase modulation. A quick calculation shows that for the 633 nm He-Ne wavelength a larger phase modulation is expected $\Delta\varphi_{633} = 3.2\pi$. To experimentally determine the phase modulation as a function of displayed grayscale value, the SLM was incorporated into one arm of a Michelson interferometer. This interferometer was constructed with fixed arms, so that phase changes are introduced only by the SLM. A uniform grayscale image (60 × 792 pixels) was computer generated having a specific grayscale value between 0 and 255. This image was subsequently displayed on the SLM through a digital visual interface (DVI) connection and the output power of the interferometer was measured (Ophir PD300-UV) as a function of grayscale value. Recorded data (blue squares) are shown in Figure 3.3(a) and have been fitted to the theoretically expected result $P = P_0 \cos^2\left(\varphi/2\right)$ (solid black curve). From this fit, the phase modulation as a function of grayscale value was determined from $\varphi = 2\arccos\left(\sqrt{P/P_0}\right)$.

From this fit, the phase modulation as a function of grayscale value was determined from e^{iC}. Figure 3.3(b) shows the phase modulation given as a function of grayscale value. The phase modulation φ as a function of grayscale value χ was found to be described by a linear function $\varphi = m\chi \approx \left(1.8\pi/100\right)\chi$ with a maximum phase modulation of $\sim 4\pi$ radians for a grayscale value of $\chi = 200$, which is in rough agreement with our estimate. For grayscale values greater than ~200, the phase modulation introduced by the SLM exhibited a nearly constant behavior. This can be seen by the blue squares in Figure 3.3(a) where the data points deviate from the theoretical curve. Consequently, as seen by the blue circles in Figure 3.3(b), a gap appears in the data for phase modulation versus grayscale value. The reason for this is not known, but for experiments reported here, phase modulations of less than 2π radian, corresponding to grayscale values less than ~100, were used.

Since we use our SLM in a folded version of a 2 f -2 f setup to compensate for angular dispersion [78], we find it convenient to use the second half of the SLM's LCD to characterize the amplitude-phase-modulated optical beams produced on the first pass of the setup. This was accomplished using an amplitude-phase encoding method on a phase-only device, which makes use of blazing techniques [73,83,84].

For these reasons, two parameters were explored in this experiment: the grating period Λ measured in pixels (20 μm pitch) and the modulation depth m given in grayscale value. The purpose of this measurement was to experimentally determine the optimal blazing conditions. Nine sets of data were recorded; one for each value of the grating period $\Lambda = \{3,4,6,7,8,10,13,15,20\}$. For each data set, the first order diffraction efficiency was measured as a function of modulation depth. For all data sets, each having a different grating constant, the maximum efficiency was found to correspond to a modulation depth having a grayscale value of roughly 105, which from the calibration data is a phase modulation of ~ 2π radians. The peak in the diffraction efficiency curves at this value of the phase is in agreement with that expected from diffraction theory when using blazed grating [80,85]. The diffraction efficiency is expected to increase with increasing number of steps [80]. This increase is experimentally observed; however, the data in the inset shows that in the first diffraction order, the efficiency was found to be optimal for a grating period of 8 pixels or $\Lambda = 160\,\mu$m and then decreased. Based on the results shown in Figure 3.4 all gratings used in this work were designed to have a grating period of $\Lambda = 160\,\mu\mathrm{m}$, which corresponded to a diffraction angle of $\theta \approx 4\mathrm{mrad}$ for 633 nm, and a phase modulation depth of 2π or less.

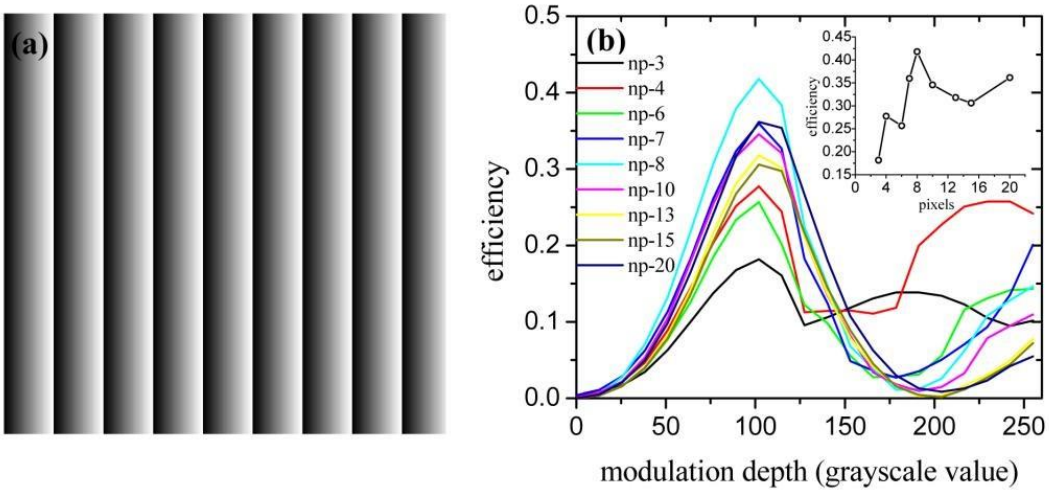

Figure 3.4 (a) Illustration of a blazed phase grating having modulation depth m and spatial Λ period displayed on the SLM. (b) Blazing efficiency as a function of modulation depth measured as the ratio of the power in the first diffraction order to that in the zero order. Nine sets of data were obtained each having a different grating period and denoted by the number of pixels (np) used for the grating period. Each pixel is assumed to be equal to the pitch, which is 20 µm. All data sets show a peak at a grayscale value of ~100, which corresponds to a phase shift of 2π radian. The inset in panel (b) shows the efficiencies for the peak values (grayscale value of 100) demonstrating the best achieved diffraction efficiency for a grating period of 8 pixels.

3.3 Equivalence between holographic and mechanical knife-edge methods

In this work, we employ a technique that uses a phase hologram encoded with phase and amplitude information to knife edge eigenmodes of the paraxial wave equation. The commonly-known knife-edge measurements use hard apertures and are amplitude modulators. It will be shown that by using off-axis holography from a phase-only modulator, the first order diffracted beam from a knife-edge hologram is proportional to an amplitude knife-edge.

Immediately preceding a mechanical knife edge or holographic grating, the electric field is assumed to have a constant phase e^{iC} and an arbitrary amplitude profile $\psi\left(x\right)$, i.e., Gaussian. For the mechanical knife edge, the radiation is modified such that only the spatial amplitude has changed and immediately following the knife-edge the electric field is $E_{mech}=H\left(x-\xi\right)\psi\left(x\right)$, where $H\left(x-\xi\right)$ is the Heaviside function, and ξ is the position of the knife-edge. For the holographic knife-edge, as shown in Figure 3.5(a), the electric field immediately following the grating is phase modulated only, but due to the choice in phase modulation the electric field amplitude in different diffraction orders can be modified locally. In this work, blazed gratings are used to control local diffraction efficiencies; however, to keep the present analysis tractable sinusoidal gratings are used [80]. The field directly following the grating can be written as the sum of a constant phase (left half of grating in Figure 3.5(a)) and a sinusoidal phase modulation (right half of grating in Figure 3.3(b)),

$$E_{holo}=\left(H\left(\xi-x\right)+H\left(x-\xi\right)\sum_{q=-\infty}^{\infty}J_q\left(\frac{m}{2}\right)e^{iqKx}\right)\psi\left(x\right) \tag{3.2}$$

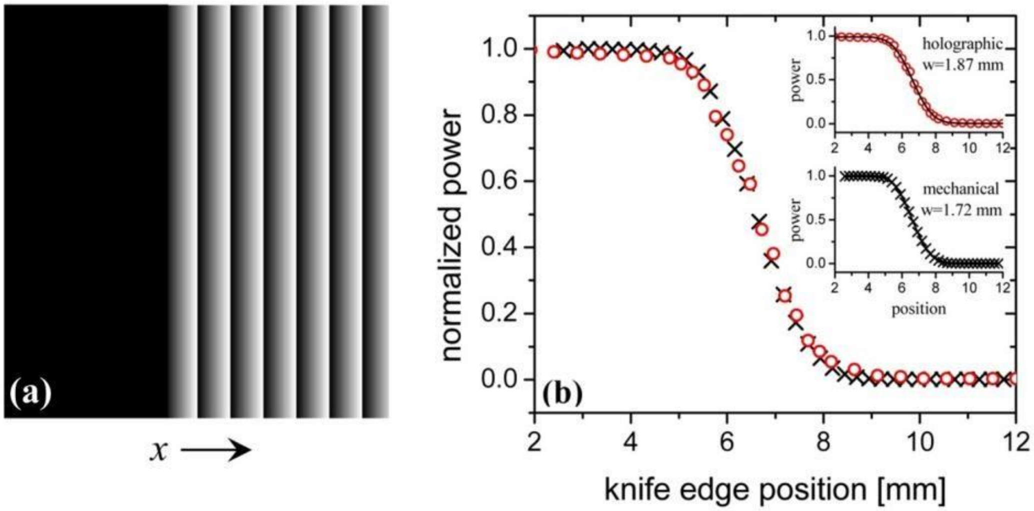

Figure 3.5 (a) Illustration of a hologram used to create a holographic knife-edge. The solid black color on the left side of hologram denotes a constant phase modulation and the right side of the hologram is that of a blazed grating. (b) Measured power as a function of knife-edge position. The black crosses represent the measured power from a mechanical knife-edge position at the location of the SLM, and the red circles are that obtained from the holographic knife-edge. Both mechanical and holographic knife-edge measurements are in good agreement. The insets are fits of the data to theoretical curves.

Here the Jacobi-Anger expansion has been used in the second term to expand the sinusoidal phase grating $exp\left[\left(i\ m/\ 2\right)sin\left(Kx\right)\right]$ in terms of plane waves with coefficients given by Bessel functions of the first kind $J_q\left(x\right)$. The modulation depth of the sinusoidal phase grating is given by *m* and $K=2\pi/\Lambda$ is the grating constant having a spatial period of Λ. The first term in Eq. (3.2) is the electric field amplitude $\psi\left(x\right)$ that has been "cut" by the holographic knife-edge function $H\left(\xi-x\right)$. This first term and the $q=0$ term direct light into the zero order. All terms in the sum with $q \neq 0$ are responsible for redirecting radiation into higher diffraction orders. This can be seen from the argument of the exponential qK. If the diffraction orders are allowed to separate, then to a good approximation the electric field in the first diffraction order can be taken as $E_{holo} \approx \left(H\left(x-\xi\right)J_1\left(m/2\right)e^{iKx}\right)\psi\left(x\right)$. Because this separation is possible and because the exact intensity profile is unimportant (since it is integrated over by a power meter), it is not necessary to propagate this field using the Huygens-Fresnel-Kirchhoff integral. As can be seen, this field consists of the field from the mechanical knife edge $E_{mech} = H\left(x-\xi\right)\psi\left(x\right)$, therefore we can combine both equations and take the modulus squared to determine the intensity going into the first diffraction order $I_{holo}\left(x;\xi\right) = J_1^2\left(m/2\right)I_{mech}\left(x;\xi\right)$. Since $J_1\left(m/2\right)$ is a constant, this last result states that the intensity of the holographic knife-edge is proportional to that of the mechanical knife-edge. The power is then found by integrating over all space $P_{holo}\left(\xi\right) = J_1^2\left(m/2\right)P_{mech}\left(\xi\right)$. As a note, the proportionality factor will be different for different types of gratings such as a blazed grating. The zero and higher orders also contain knife-edge information, but these orders contain residual angular dispersion and for this reason may not be the best choice to measure the power. Additionally, the corrected first order can be imaged with a CCD camera for further analysis.

To experimentally investigate the equivalence between the holographic knife-edge and the more traditional mechanical knife-edge, the fundamental Gaussian laser beam from a He-Ne laser was used for comparison of the two methods. Figure 3.5 shows the results of both measurements. The mechanical knife-edge was performed at the position of the SLM. The holographic knife-edge was performed using a grating similar to that shown in Figure 3.5 (a) with $\Lambda = 160\ \mu\text{m}$ and $\varphi = 2\pi$. The discontinuity at x was scanned, and the knife-edge data was recorded by a photodiode. The waist of the Gaussian beam was found to be roughly ~2 mm, which was obtained by fitting the data with $P = P_0 \text{erfc}\left(\sqrt{2}x / w\right) / 2$. This is in agreement with the size of the output of the He-Ne laser (~0.5 mm) after passing through a beam expander, which had a magnification of four times (~2 mm). More precisely these values were found to be 1.87 mm and 1.72 mm for the holographic and mechanical knife edge measurements respectively, inset in Figure 3.5(b). The two sets of data are in good agreement, demonstrating that the holographic knife-edge can be effectively used to characterize laser beams. To further demonstrate the utility of this method, a number of different optical modes were created and analyzed using this knife-edge method. To the best of our knowledge, knife-edge equations for the Hermite and Laguerre Gaussian modes have not been shown in the literature. The derivation of these equations is the topic of the subsequent sections. There exists another family of solutions to the paraxial wave equation known as the Ince-Gaussian modes. These solutions are mathematically somewhat more difficult to deal with than the HG and LG modes and for this reason will not be considered here. However, it is noted that the IG modes are an excellent example where a “soft aperture” is easier to make than a “hard aperture”. This is because the natural choice for knife-edging these beams consists of confocal ellipses and hyperbolas.

3.4 Experimental setup

Figure 3.6 shows an illustration of the experimental setup used to generate and analyze the paraxial beams used in this work. Since only a single SLM was used in this experiment, the SLM's display was divided into halves, each half having a different hologram: the first hologram was encoded with phase-amplitude information to produce a desired optical beam, and the second was encoded with the holographic knife-edge. An example hologram is shown in the inset of Figure 3.6.

This setup is similar in design to the folded-2f setup used in [78]. Laser light from two different sources was used in this work. Monochromatic radiation was from a He-Ne laser (Melles Griot) having a maximum output power of 2.5 mW, a wavelength of 633 nm and a $e^{1/2}$ beam waist of 0.5 mm. Broadband radiation was produced from a KMLabs femtosecond oscillator having a repetition rate of ~80 MHz, ~50 nm of bandwidth with a center wavelength of 800 nm and an output power of ~400 mW. This radiation was magnified by a telescoping beam expander consisting of a 50 mm diverging lens (DL) and a 200 mm converging lens (CL) to give a magnification of M=4 and resulting in a final beam size of ~2 mm. This beam waist was verified by mechanical and holographic knife-edge measurements. The expanded beam was shone onto a spatial light modulator (Hamamatsu LCOS-SLM X10468). The SLM was a parallel aligned liquid crystal on silicon (LCOS) spatial light modulator having a resolution of 800x600 pixels (16 mm x 12 mm), and a maximum reflectivity of >95% for radiation between 750 nm and 850 nm. The SLM was capable of modulating the local phase within the beam by over 2π radian for radiation within the specified wavelength range. Grayscale computer generated holograms CGHs were displayed on the SLM's LCD via a digital visual interface DVI connection. Phase modulated beams from the SLM in the first diffraction order were reflected back onto the SLM where they were analyzed by the second half of the hologram. Power measurements were obtained using a photodiode power meter head (Orphir PD300-UV) having a spectral response of 200 nm to 1100 nm.

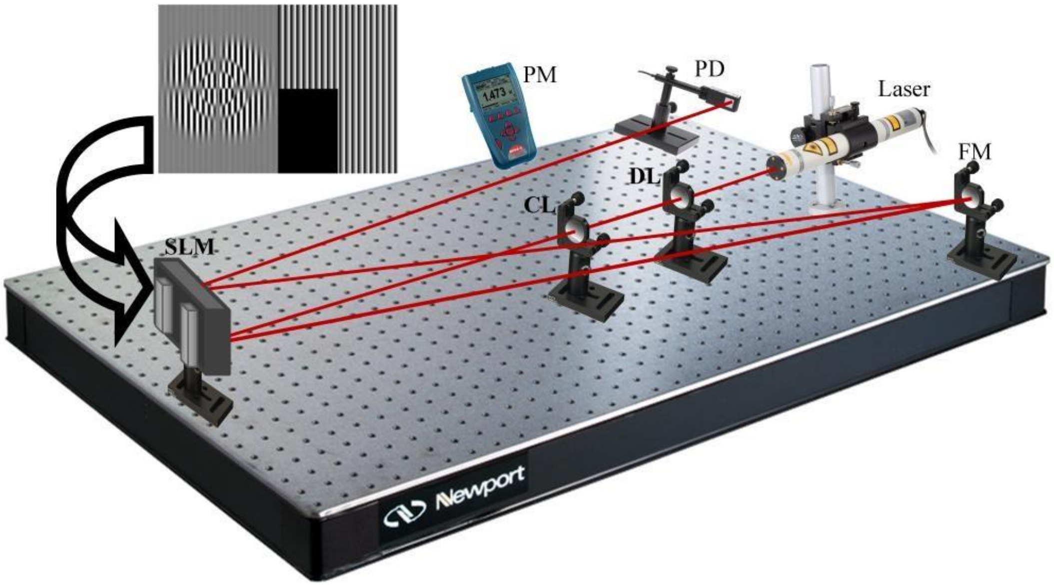

Figure 3.6. Experimental setup. Laser radiation from either a He-Ne or Ti:sapphire laser enters the setup from the right. DL = 50 cm diverging lens, CL = 200 cm converging lens, SLM = spatial light modulator, FM = folding mirror placed a distance of f =100 cm away from the SLM, PD = photodiode power meter head, PM = power meter. The upper left inset is an example hologram to create a $\mathrm{LG}_{2,2}^{o}$ beam followed by an angular knife-edge.

The knife-edge data, shown in this work, is the result of integrating the spatial intensity profile by a power meter. To qualitatively illustrate the performance of the holographic knife-edge, images of the zero and first orders for an odd $\mathrm{LG}_{2,2}^{o}$ beam produced with He-Ne wavelengths were recorded with a CCD camera. In Figure 3.7, the knife-edge measurement was performed in an azimuthal direction. For illustration purposes, the angular step size was taken to be 90 degrees. The upper sequence in Figure 3.7(a) is a representation of holograms with angular knife-edge angles of 0, 90, 180, 270 and 360 degrees. This grating was blazed according to optimal conditions shown in Figure 3.4. In the lower sequence, the images were taken with a CCD camera and show the intensity profiles in the zero and first orders. In the first frame, the grating is that of a regular blazed grating showing only a fraction of the power in the zero order compared to that in the first order. When a section of the holographic grating is set to a constant phase, this part of the beam will be directed into the zero order. It can be seen that the radiation in the first diffraction order, corresponding to this region, has been removed and appears in that region of the zero order. In the remaining frames of the sequence, the azimuthal knife-edge is increased in steps of 90 degrees, and with each step a portion of the optical mode is redirected into the zero order until the beam in the first diffraction order vanishes, and the grating becomes that of a constant phase plate.

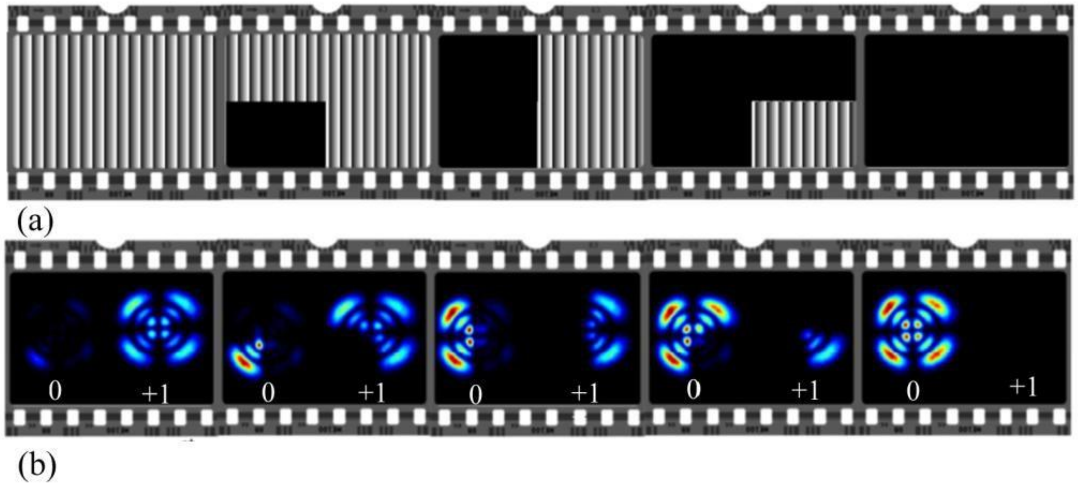

Figure 3.7 Intensity profiles of a $\mathrm{LG}_{2,2}^{o}$ beam being azimuthally knife-edged. (a) This sequence of frames shows the holograms used to perform an angular knife-edge measurement with an angular step size of 90 degrees. (b) CCD images of radiation from a He-Ne source after passing through the corresponding grating in sequence (a). Each frame shows both the zero and first diffraction orders. As the area of constant phase (denoted by the blackened areas in (a)) increases, the corresponding local radiation in the first diffraction order is directed into the zero order until the radiation is gone.

3.5 Knife-Edge equations for the Hermite-Gaussian beams

In contrast to theoretically obtained knife-edge curves, experimental measurements yield data that is not always monotonically increasing or decreasing. Due to noise such as laser fluctuations, differentiation of experimental data may lead to noisy and/or unphysical results. For this reason, it is advantageous to fit experimentally obtained data with theoretical curves in which one can extract quantitative beam parameters needed to characterize the beam. This is commonly practiced by experimentalists when performing knife-edge measurements for Gaussian beams [86]. For more complex beams such as that shown in Figure 3.7, one can readily determine the relative power and spatial extent within each modal lobe by observing the plateau regions of a knife-edge measurement of the beam.

The Hermite-Gaussian modes are eigensolutions of the paraxial wave equation in Cartesian coordinates. Because of their rectangular geometry, a straight-edge presents a natural choice for characterizing such beams. Theoretical knife-edge curves for the HermiteGaussian modes have been presented in the literature [87] The authors in this work, however, stated that they were unable to obtain a general analytical form for the knife-edge equations and therefore presented numerical solutions. Using numerical solutions complicates fitting routines when obtaining beam parameters from experimental data. For this reason, we present the derivation of these analytical solutions. The electric field amplitude of the Hermite-Gaussian modes is,

$$E_{\mathrm{HG}_{n,m}} = N_{n.m} E_0 \frac{w_0}{w} \mathrm{H}_n\left(\frac{\sqrt{2}x}{w(z)}\right) \mathrm{H}_m\left(\frac{\sqrt{2}y}{w(z)}\right) e^{-\left(r^2/w^2\right)} e^{i\left[\frac{kr^2}{2R} - (\mathrm{m}+\mathrm{n}+1)\varphi_G + kz\right]} \tag{3.3}$$

Here w_0, $w(z)$ and $z_0 = \pi w_0^2 / \lambda$ are the beam waist and size and Rayleigh range respectively; $\varphi_G(z) = \arctan(z / z_0)$ is the Gouy phase, $R(z) = z + z_0^2 / z$ is the radius of curvature, and H_n are the Hermite Polynomials in which *n* and *m* are mode numbers. The normalization factor $N_{n,m} = \sqrt{1/2^{n+m} n! m!}$ is chosen such that the integral of

$I_{HG_{0,0}} = \left|E_{HG_{0,0}}\right|^2$ over all space leads to $P_0 = \pi I_0 w_0^2 / 2$. The measured position-dependent power is found from,

$$P_{\mathrm{HG}_n}\left(x\right) = \int_x^\infty \int_{-\infty}^\infty I_{\mathrm{HG}_{n,\mathrm{m}}}\left(x', y', \mathrm{z}'\right) dx' dy' \tag{3.4}$$

A similar expression can be written for a knife-edge measurement performed in the *y* direction; however, the functional form of the solution is the same as that found for the *x* direction. To find the power as a function of the knife-edge position, it is advantageous to make the following substitutions $\xi = \sqrt{2}x/w$ and $\eta = \sqrt{2}y/w$ Eq. (3.3) prior to integration,

$$P_{\mathrm{HG}_n}\left(x\right) = N_{n,m}^2 I_0 w_0^2 \frac{1}{2} \int_{-\infty}^\infty \mathrm{H}_m^2\left(\eta\right) e^{-\eta^2} d\eta \int_x^\infty \mathrm{H}_n^2\left(\xi\right) e^{-\xi^2} d\xi = N_{n,m}^2 I_0 w_0^2 \frac{1}{2} I_\eta I_\xi\left(x\right) \tag{3.5}$$

Here I_η is the integral over the *y* direction, and its solution is well-known from the normalization of H_m to be $I_\eta = m! 2^m \sqrt{\pi}$. Because the Hermite polynomials are indexed by a single mode number and because the position-dependent power depends on the integral I_ξ, the knife-edge measurement over a single coordinate direction depends only on the mode number in that direction. To solve the I_ξ integral, we use Rodrigues formula $\mathrm{H}_n\left(\xi\right) = \left(-1\right)^n e^{\xi^2} d^n \left(e^{-\xi^2}\right) / d\xi$ for the Hermite Polynomials,

$$I_\xi = \left(-1\right)^n \int_x^\infty \mathrm{H}_n\left(\xi\right) \frac{d^n}{d\xi^n}\left(e^{-\xi^2}\right) d\xi \tag{3.6}$$

Integrating by parts one time and using the Appell sequence $H_n' = 2nH_{n-1}$, where n=1,2,3,…, Eq. (3.6) becomes,

$$I_\xi = \left(-1\right)^n \left[-\mathrm{H}_n\left(\xi\right)\frac{d^{n-1}}{d\xi^{n-1}}\left(e^{-\xi^2}\right) - 2n\int_x^\infty \mathrm{H}_{n-1}\left(\xi\right)\frac{d^{n-1}}{d\xi^{n-1}}\left(e^{-\xi^2}\right)d\xi \right] \tag{3.7}$$

Rodrigues formula can be used once again to remove the derivative in the first term, showing how the first term in a sequence of terms is found,

$$I_\xi = \left(-1\right)^n \left[\left(-1\right)^n e^{-\xi^2}\mathrm{H}_{n-1}\left(\xi\right)\mathrm{H}_n\left(\xi\right) - 2n\int_x^\infty \mathrm{H}_{n-1}\left(\xi\right)\frac{d^{n-1}}{d\xi^{n-1}}\left(e^{-\xi^2}\right)d\xi \right] \tag{3.8}$$

Continuing in this fashion *n* times, the position-dependent power can be obtained. Upon restoring the contribution from the y-integral, the measured power from the knife-edge experiment reduces to the finite sum,

$$P_{\mathrm{HG}_n}\left(x\right) = \frac{1}{2}P_0\left\{ e^{-\xi^2}\sqrt{\frac{1}{\pi}}\sum_{k=1}^{n}\frac{2^{k-n}}{\left(n+1-k\right)!}\mathrm{H}_{n-k+1}\left(\xi\right)\mathrm{H}_{n-k}\left(\xi\right) + \mathrm{erfc}\left(\xi\right) \right\} \tag{3.9}$$

Here $\xi\left(x\right) = \sqrt{2}x/w$, and the last term is the complimentary error function $\mathrm{erfc}\left(\xi\right) = 1 - \mathrm{erf}\left(\xi\right)$. The total power P_0 is that from the integration over all space.

From Eq. (3.9), it can be seen that the position-dependent power is independent of the mode number governing the y -dependent part of the beam profile. When n=0, the term in Eq. (3.9) containing the sum vanishes, and Eq. (3.9) reduces to the well-known knife-edge formula for a Gaussian beam $P_{\mathrm{HG}_n}\left(x\right)=P_0\mathrm{erfc}\left(\xi\right)/2$.

In Figure 3.8, knife-edge measurements of higher-order Hermite-Gaussian beams are shown along with fit-curves based on Eq. (3.9). The squares (circles) are from knife-edge measurements in the $x\left(y\right)$ direction. In the data, some curves can be seen to have plateaus. These plateaus correspond to nodes of the beam, and are equal in number to the mode numbers. In the x knife-edge, the number of plateaus corresponds to mode number n in Eq. (3.3), and in the y direction to mode number m. The ratio of the powers between the plateaus gives an indication of the symmetry of the modal structure. The red curves were obtained by fitting to the data using Eq. (3.9). In general good agreement is found between experiment and theory. Since the beam size $w\left(z\right)$ is independent of the mode numbers, the $\mathrm{HG}_{2,2}$ mode has the same beam size as that of the $\mathrm{HG}_{0,0}$ mode. The beam size in the x and y directions was found to ~52 pixels or ~1 mm.

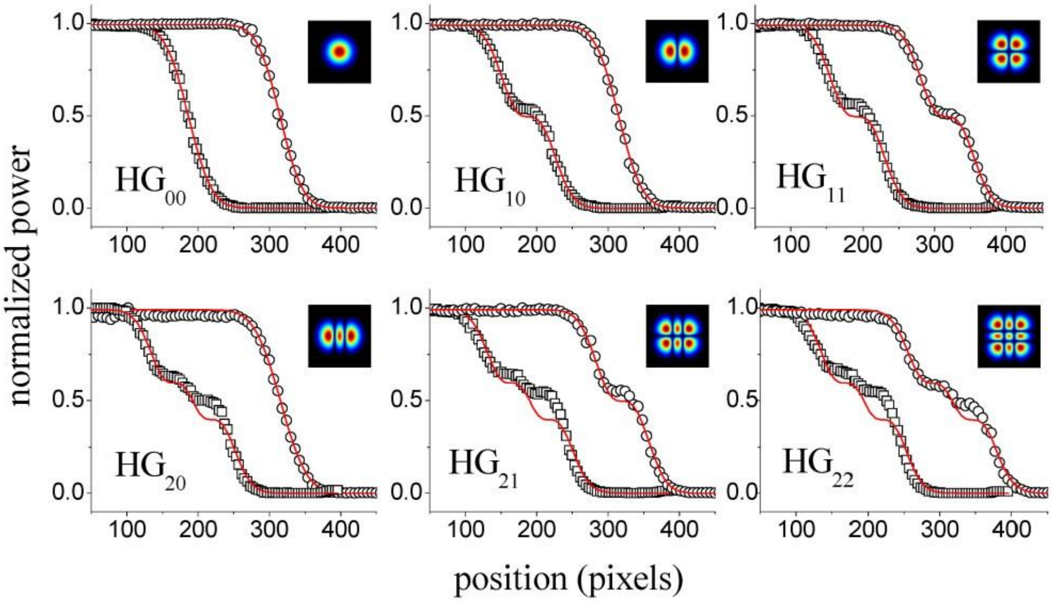

Figure 3.8 Cartesian knife-edge measurements of the Hermite-Gaussian modes. The modality of each mode is given as the label of the panel. The black opened squares are data taken from knife-edge measurements in the *x* direction and the black opened circles are that in the *y* direction. The number of plateaus is equal to the mode number. The red curves were obtained by fitting the data with theoretical curves presented in the text. From this fit the beam size was determined.

3.6 Knife-Edge equations for the Laguerre-Gaussian beams

Similar to the knife-edge measurements for the Hermite-Gaussian modes, there exist preferable knife-edge geometries when considering beams in cylindrical polar coordinates: azimuthal and radial. The radial knife edge measurement is similar to closing an iris down on a beam. Less familiar is the azimuthal knife edge, which mechanically would be similar to the opening of a folding fan. The azimuthal knife-edge is a prime example of a knife edge geometry which is difficult to mechanically reproduce. An example of a more difficult knife-edge is that used for the Ince-Guassian beams. The azimuthal and radial knife-edge analogues for the Ince-Gaussians beams correspond to the mechanically difficult to reproduce hyperbola and ellipses—these geometries; however, are readily produced using computers.

The radial-knife equation is found in a similar form to that carried out for the HermiteGaussian knife-edge equations. The electric field of the Laguerre-Gaussian beam is

$$E_{\mathrm{LG}_{l,p}} = N_{l,p} E_0 \frac{w_0}{w}\left(\frac{\sqrt{2}r}{w(z)}\right)^{l} L_p^l\left(\frac{2r^2}{w^2(z)}\right) e^{-\left(r^2/w^2\right)} e^{il\theta} e^{i\left[\frac{kr^2}{2R}-(2p+l+1)\varphi_G+kz\right]} \ . \tag{3.10}$$

The normalization factor $N_{l,p}$, is chosen such that the integral of $I_{LG} = \left|E_{LG}\right|^2$ over all space leads to $P_0 = \pi I_0 w_0^2 / 2$. The measured position-dependent power is found from the volume integration of the intensity,

$$P_{\mathrm{LG}}(r) = \int_0^r \int_0^{2\pi} I_{LG}(r') r' dr' d\theta' \ . \tag{3.11}$$

To find the power as a function of the knife-edge position, it is advantageous to make the following substitution $\xi = 2r^2 / w^2$ to Eq. (3.10),

$$P_{\mathrm{LG}_{l,p}}(r) = \frac{\pi}{2} I_0 w_0^2 N_{l,p}^2 \int_0^r \xi^l L_p^l(\xi) L_p^l(\xi) e^{-\xi^2} d\xi = \frac{\pi}{2} I_0 w_0^2 N_{l,p}^2 I_\xi(r) \ . \tag{3.12}$$

The solution to the integral $I_\xi(r)$ from zero to infinity is well-known from normalization of the associated Laguerre polynomials to be $(p+l)!/\,p!$. Unlike the $\mathrm{HG}_{n,m}$ modes, the position-dependent power for the radial knife-edge of the LG modes depends on both the radial p and azimuthal l mode numbers. To solve for the integral, we use Rodrigues formula $L_p^l(\xi)=\left(\xi^{-l}e^{\xi}/p!\right)d^p\left(\xi^{p+l}e^{-\xi}\right)/d\xi^p$ for one of the Laguerre Polynomials,

$$I_\xi=\frac{1}{p!}\int_0^r\frac{d^p}{d\xi^p}\left(\xi^{p+l}e^{-\xi}\right)L_p^l(\xi)\,d\xi\ . \tag{3.13}$$

Integrating by parts one time and using the differential relation $L_p^{l\,\prime}=-L_{p-1}^{l+1}$,

$$I_\xi=\frac{1}{p!}\left[L_p^l(\xi)\frac{d^{p-1}}{d\xi^{p-1}}\left(\xi^{p+l}e^{-\xi}\right)-\int_0^r L_p^{l\,\prime}(\xi)\frac{d^{p-1}}{d\xi^{p-1}}\left(\xi^{p+l}e^{-\xi}\right)d\xi\right]. \tag{3.14}$$

Rodrigues formula can be used once again to remove the derivative in the first term,

$$I_\xi=\frac{1}{p!}\left[(p-1)!\,\xi^{l+1}e^{-\xi}L_p^l(\xi)L_{p-1}^{l+1}(\xi)-(-1)\int_0^r L_{p-1}^{l+1}(\xi)\frac{d^{p-1}}{d\xi^{p-1}}\left(\xi^{p+l}e^{-\xi}\right)d\xi\right] \tag{3.15}$$

Continuing in this fashion p times gives the position-dependent power in terms of a finite sum,

$$P_{LG_p^l}(r)=P_0\left\{e^{-\xi}\sum_{k=1}^{p}(p-k)!\,\xi^{l+k}L_{p-k}^{l+k}(\xi)L_{p-k+1}^{l+k-1}(\xi)+\gamma(p+l+1,\xi)\right\} \tag{3.16}$$

Here $\xi=2r^2/w^2$ and the last term is the incomplete gamma function. From Eq. (3.16), it can be shown that when p,l =0, Eq. (3.16) returns the radial knife-edge formula for a Gaussian beam $P_{\mathrm{LG}}(r)=P_0\left(1-exp\left(-2r^2/w^2\right)\right)$. In contrast to the knife-edge curves found for the Hermite-Gaussian beams, the radial knife-edge curves of the LG beams depend on both the radial and azimuthal mode numbers.

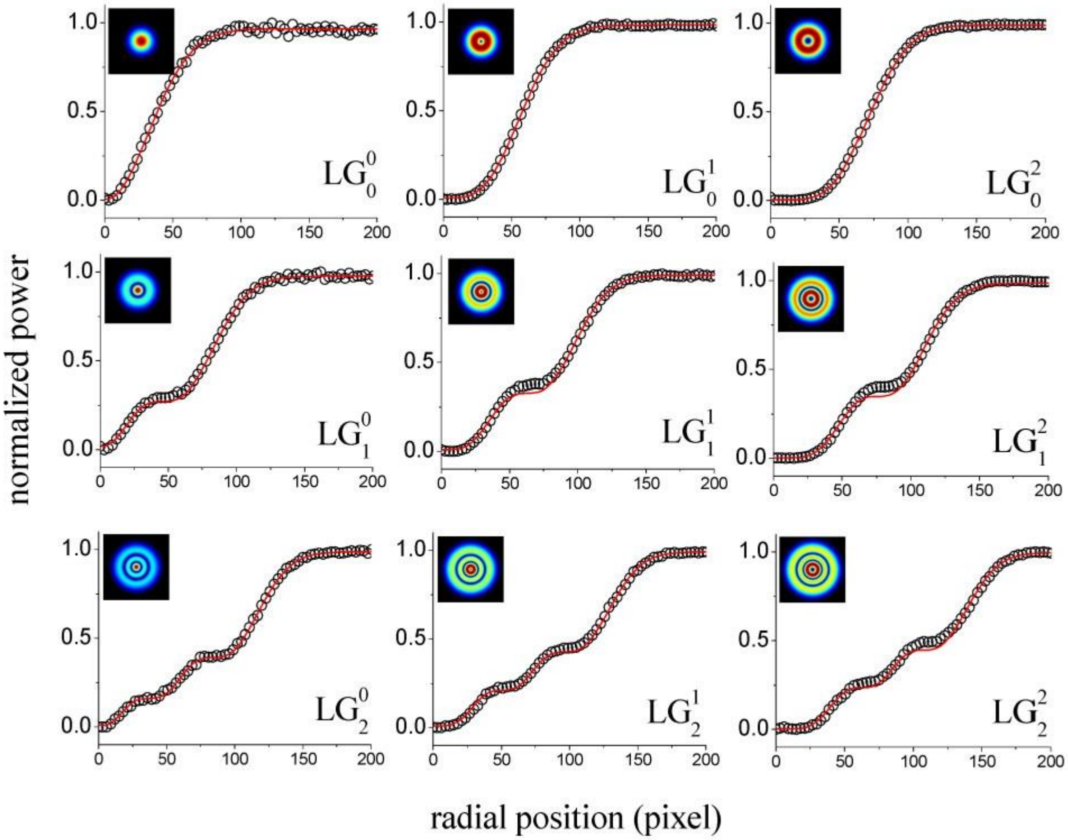

Figure 3.9 Radial knife-edge measurements for an assortment of helical Laguerre-Gaussian beams. The number of plateaus is equal to the radial mode number p. The waist of the beams can be determined by fitting the data to the theoretical equations given in the text. The fits are shown by the solid red curves. Unlike the HG beams, the radial knife-edge measurements depend on both radial and azimuthal mode numbers *p* and *l*. The dependence of the curve on the azimuthal mode number can be seen by the size of the initial plateau increasing from the leftmost column to the rightmost column.

Figure 3.9 shows radial knife-edge measurements of nine LG_p^l beams. Their modalities are denoted in the figures. Going from left to right in each column, it can be seen that the initial plateau (corresponding to the intensity profile near the vortex core) becomes increasingly extended with increasing angular mode number l. This is expected since the peak position of the doughnut beam increases with angular mode number according to $r = w\sqrt{l/2}$.

Comparatively, the azimuthal knife-edge for the LG beams requires little calculational effort. In addition to the well-known helical LG beams, there also exist the even and odd solutions of the paraxial wave equation denoted by $\mathrm{LG}_{p,l}^e$ and $\mathrm{LG}_{p,l}^o$ respectively. Helical LG beams do not show parity in the azimuthal coordinate as do the even and odd solutions

[73]. Because of this, all knife-edge curves in the azimuthal direction for the helical LG beams will be identical and equal to $P_{\mathrm{LG}_p^\ell}(\theta) = P_0(1-\theta/2\pi)$ for all mode numbers p and l.

For the even and odd LG modes, which are related by a rotation of 90 degrees, the knife-edge curves are found from the integrals to be,

$$P_{\mathrm{LG}}(\theta) = P_0\left\{1-\frac{\theta}{2\pi}\left[1\pm\frac{\sin(2l\theta)}{2l\theta}\right]\right\} \tag{3.17}$$

where $+(-)$ stands for the even (odd) LG mode. Since $\mathrm{LG}^{o}_{p,l}$ contains $\sin(l\theta)$ Eq. (3.17) does not hold for the odd solutions when l=0. However, the even solutions contain $\cos(l\theta)$ so when $l=0$ Eq. (3.17) reduces to $P_{\mathrm{LG}}(\theta)=P_0(1-\theta/2\pi)$. Figure 3.10 shows the results for the azimuthal knife edge. The odd LG beams have been shown because they are related to the even LG beams by a rotation of 90 degrees. Unlike the radial knife-edge equation for the LG beams, the azimuthal knife-edge equation depends only on the azimuthal mode number l and by itself cannot be used to obtain information about the radial structure of the beam such as the waist. However, this measurement can be used as an indication of the azimuthal purity of the beam.

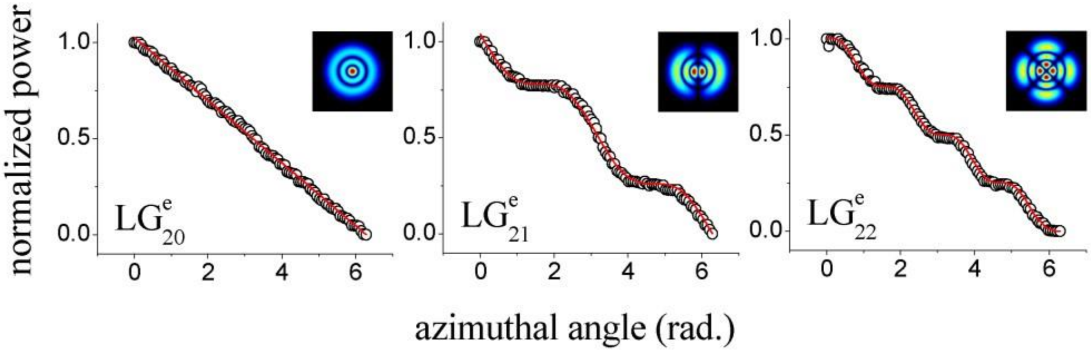

Figure 3.10 Angular knife-edge measurements for an assortment of even LG beams having modalities as indicated. The number of plateaus is equal to twice the angular mode number $2l$. The waist of the beam cannot be determined from an angular knife-edge measurement, but this measurement can give an indication of the quality of the modal lobes.

3.7 Tomographic reconstruction

We conclude this work with experimental results on the tomographic reconstruction of femtosecond $\mathrm{LG}_{p=1}^{l=1}$ optical modes. Even though we have chosen a known optical beam, it is important to note that this reconstruction can be applied to optical beams having an arbitrarily-shaped intensity profile. There exist techniques to tomographically reconstruct optical beam using knife-edge methods [88,89]. We reconstruct beams by using two orthogonal knife-edge measurements, i.e., one along the *x* direction and the other along the *y* direction were taken by stepping the first knife-edge by a single step, completely knife-edging with the second knife-edge and then stepping the first knife another step and so on until the process is completed. For convenience, we have chosen Cartesian knife-edging, but in principle other geometries are possible i.e., the radial and azimuthal knife-edge measurements of polar coordinates. In general, the measured power from a double-knife-edge procedure has the form of Eq. (3) with integration limits $\left(-\infty, x\right]$ and $\left(-\infty, \mathrm{y}\right]$, and arbitrary intensity profile $I\left(x, y\right)$. To reconstruct the intensity profile from the measured data all that is needed is the double derivative of the power $\partial^2 P / \partial x \partial y = I\left(x, y\right)$.

Figure 3.11(a, c) shows raw double-knife-edge data for a broadband $\mathrm{LG}_{p=1}^{l=1}$ beam compensated and uncompensated for angular dispersion, which was achieved by using a concave mirror *f*=100 cm and a flat mirror as the folding mirror in the folded-2f setup. The resolution in the *x* and *y* directions is ~30 $\mu\mathrm{m}$ and ~ 40 $\mu\mathrm{m}$, respectively. Figure 3.11(b, d) are the tomographically reconstructed images according to our method. As mentioned previously, taking the derivative of experimental data can lead to noise in the resulting data. This was encountered when we reconstructed the beam images, and as a result, the raw data was sent through a mean filter before derivatives of the data were taken. As expected, the uncompensated beam exhibits a “blurring” in the dispersion plane similar to that shown in [73], while the compensated beam appears more “crisp” [76].

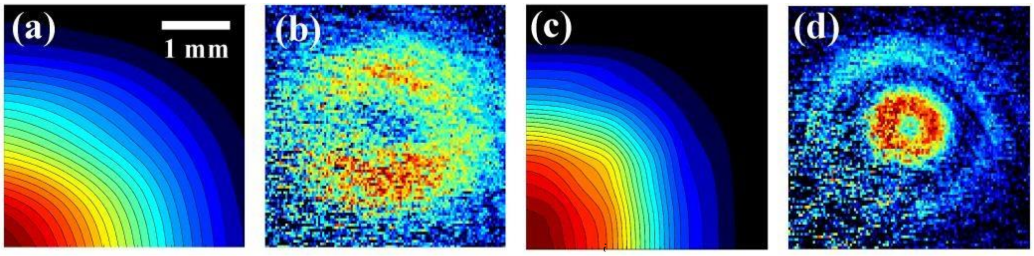

Figure 3.11. Tomographic reconstruction of a femtosecond $LG_{p=1}^{l=1}$ beam in a folded-2f setup. All images are 200-by-200 pixels and have the same vertical and horizontal scaling. The dimension of the images is given by the scale in panel (a). (a, c) Raw double-knife-edge data recorded by stepping a knife-edge in one direction (i.e., x) by a single step, completing a full knife-edge in the other direction (i.e., y), and repeating this process until finished. The raw data shown in panel (a) is that obtained by not correcting for angular dispersion in the folded-2f setup, while that in panel (c) has been corrected. Panels (b) and (d) were obtained by taking the partial derivatives (see text) of the measured double-knife-edge power.

3.8 Conclusions

In summary we have demonstrated a beam analysis method based on a holographic knife-edge. Experimental results of the measured power from both holographic and mechanical knife-edge methods showed good agreement with each other. By using the same method to that used to holographically knife-edge (phase-amplitude encoding), high fidelity HG and LG modes were produced. To analyze these modes, we derived theoretical knife-edge equations to fit to the measured data. From the derived equations we were able to determine beam characteristics such as the waist and the distribution of intensities between the modal lobes. All measured data showed good agreement with the theoretically predicted curves. In principle, the method outlined here can be used to create virtually any desired shape for the characterization of optical beams. Finally, we used this method to tomographically reconstruct, in situ, a broadband optical beam in a folded-2f setup.

CHAPTER IV

WHITE-LIGHT GENERATION USING SPATIALLY-STRUCTURED BEAMS OF FEMTOSECOND RADIATION[2]

This chapter is a synopsis of study on white-light generation and control using spatially-structured beams of femtosecond radiation [90]. We show how to create a Hermite-Gaussian ($HG_{n,m}$) beam mode by using a one-dimensional spatial light modulator (SLM) first. Then, by reviewing the role of self-focusing in white-light generation, the self-focusing lengths of the different realized transverse intensity profiles were calculated to qualitatively explain the white-light production by the created HG beam modes. Also, the distributions of the laser intensity of beams having step-wise spatial phase variations were modeled using the Fresnel-Kirchhoff integral in the Fresnel approximation.

4.1 Introduction

An ultrashort pulse propagated through a transparent medium can produce a white-light continuum, which can extend from the ultraviolet to the infrared, and this well-known phenomenon occurs in a wide variety of media [14-25]. The ultrafast white-light generation is useful for various applications such as femtosecond time-resolved spectroscopy, biomedical applications, optical pulse compression for the generation of ultrashort pulses, or as a seed pulse for optical parametric amplifiers [15,91-98].

---

[2] This chapter is based on one of our published papers that appears as Appendix E: N. Kaya, J. Strohaber, A. Kolomenskii, G. Kaya, H. Schroeder, and H. Schuessler, "White-light generation using spatially-structured beams of femtosecond radiation," Optics Express 20, 13337-13346 (2012). doi.org/10.1364/OE.20.013337.

Self-phase modulation[18-20], self-steepening[99], and parametric four-photon mixing [19] are some of the mechanisms that have been invoked to explain the white-light generation. However, the primary process responsible for the phenomenon of white-light generation is self-focusing, which causes the pulse to compress in space, resulting in a corresponding increase in the peak intensity[20]. When a threshold peak power for a white-light continuum P_{th}^{wl} is just above the input pulse power, the beam producing white-light continuum appears to the eye as a white spot. As the input peak power is increased to a few P_{th}^{wl}, a colorful ring pattern appears surrounding the central spot. The resulting beam appears to the eye as a white light disk surrounded by a distinct, concentric, rainbow-like pattern. Experiments have shown that the threshold power P_{th}^{wl} for white-light generation coincides with the calculated critical power P_{crit} for self-focusing [17,20-23,100]. Experiments conducted by Brodeur and Chin [101,102] have confirmed that white-light generation is triggered by self-focusing. Comparison of the critical power for self-focusing P_{crit} and for white-light continuum P_{th}^{wl} in several media shows that $P_{crit} \cong P_{th}^{wl}$ [102]. Therefore, it should then be noted that P_{crit} and P_{th}^{wl} are essentially equivalent.

Studies of white-light generation in liquids, which typically have nonlinear contributions to the refractive index about 10^3 times larger than that for gases, can reproduce many important features of the processes at much lower laser powers and on a much smaller scale under laboratory conditions [103]. According to Marburger's formula[104], it holds for the critical power of self-focusing

$$P_{crit} = 3.77\frac{\lambda_0^2}{8\pi n_0 n_2} \tag{4.1}$$

where $\lambda_0 = 800\ \mathrm{nm}$, $n_0 = 1.33$, and $n_2 = 2\times 10^{-16}\mathrm{cm}^2/\mathrm{W}$ [101] for water, and one obtains $P_{crit} = 3.6\ \mathrm{MW}$. Here, λ_0 denotes the laser wavelength, n_0 is the linear refractive index of the medium, and n_2 is its nonlinear coefficient. The self-focusing length of the beam with a spatial Gaussian distribution of intensity at the input of the medium [104] is given by:

$$L_{sf} = \frac{0.734\pi n_0 a_0^{\ 2}}{\lambda_0\left[\left(\sqrt{P/P_{crit}}-0.852\right)^2-0.0219\right]^{1/2}} \tag{4.2}$$

where P is the beam power and a_0 is the radius of the beam profile at the 1/e level of intensity. The self-focusing length, L_{sf}, varies as a function of the beam radius, a_0, and the ratio of the peak power over the critical power for self-focusing, P/P_{crit}.

In the present paper we show that by changing the transverse spatial phase of an initial Gaussian beam to that of an Hermite-Gaussian ($HG_{n,m}$) mode, we were able to generate beams exhibiting phase discontinuities and steeper intensity gradients. The previous experiments emphasized that the locus of conical emission was controlled by local diffraction catastrophes produced by any kind of aperture [105,106]. In the present case the situation is much clearer. When the spatial phase of an initial Gaussian beam (showing no significant white-light generation) was changed to that of a $HG_{0,1}$, or $HG_{1,1}$ mode, significant amounts of white-light were produced. The self-focusing lengths determined by the peak powers and radii of the lobes in the resulting transverse intensity profiles were used to qualitatively explain this production, because self-focusing is known to play an important role in white-light generation. Distributions of the laser intensity for beams having step-wise spatial phase variations were modeled using the Huygens-Fresnel-Kirchhoff diffraction formulation in the Fresnel approximation and were found to be in good agreement with experiment.

4.2 Experimental procedure

In the experiment, an 800 nm Ti:sapphire laser system (Spitfire, Spectra Physics) with a typical power of about 1W and pulse duration ~50fs was employed. From Eq. (4.2), for constant beam power the self-focusing distance is proportional to the square of the beam size so decreasing the beam size decreases the self-focusing distance. Therefore, to shorten the length for white-light formation we reduced the beam size by using an optical telescope. For generating taylored phase variations we used a Spatial Light Modulator (SLM) to change the transverse spatial phase of an initial Gaussian beam to that of an HGn,m mode. In the following the formation and recording of the resulting transverse intensity profiles together with their analytical form are presented. Subsequently the experiments of white-light generation of these beams are described.

4.2.1 Liquid Crystal -Spatial Light Modulator (LC- SLM)

For generating taylored phase variations we used a Spatial Light Modulator (SLM), Jenoptik SLM-S 640/12, which is a liquid crystal modulator with 640 stripe-shaped pixels and 12 bit resolution to change the transverse spatial phase of an initial Gaussian beam to that of an HGn,m mode. Its active area is 63.7 mm x 7 mm, and the transmission for a wavelength range (430 nm-800 nm) is >75%. The nematic liquid crystal is driven by a 0-8 V RMS voltage with frequency 4 kHz. The maximum phase shift at 430 nm is 7π and at 1500 nm is 2π. The damage threshold as given by the datasheet is 300GW/cm2 at 800nm, 45 fs and repetition rate of 1 kHz. This is the same SLM with that we used in our previous studies [107]. The LC SLM is controlled by a controller board which can be connected to a PC via the RS 232 interface. The modulator can be controlled by simple terminal program including LabView or other programming language with RS-232 functions.

The retardation of LC-SLM was measured with a simple set up. A He-Ne laser was used as a light source. Two linear polarizing plates were set up with the transmission axes perpendicular to each other with an angle of 45 deg. to the vertical axis of the liquid crystal spatial light modulator array. Two lenses are used to focus the beam into one stripe. This is necessary to get the phase retardation of only one stripe of the LC cell.

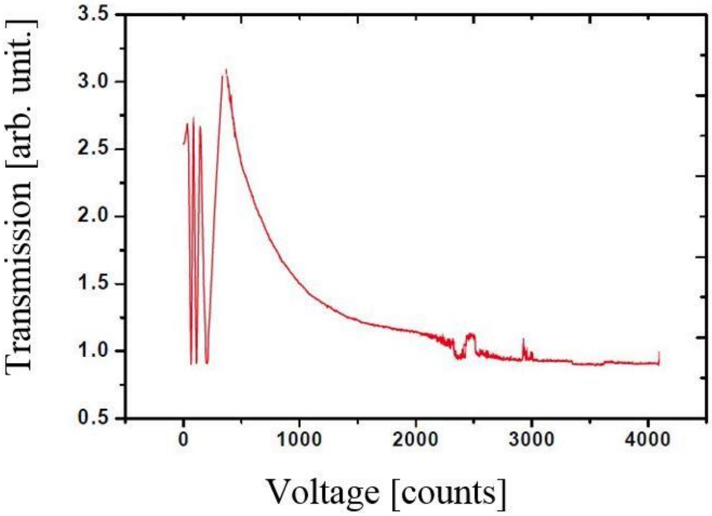

Figure 4.1. Measured transmission signal with crossed polarizer.

The light emerging from the array was focused onto a standard photo diode. The transmission was recorded in dependence of the pixel voltage (0-8) V in 4096 steps. The transmission curve is shown in Figure 4.1.

The dependence for the reconstruction of the retardation from the measured transmission function is given by

$$\Gamma(U) = 2\,sin^{-1}\left(\frac{T}{U}\right) \tag{4.3}$$

where *U* is a function of the voltage and *T* is the Transmission.

To account for the π periodicity the retardation function, $\Gamma(U)$ has to be unwrapped by adding multiples of π. Figure 4.2 shows the typical characteristic of the phase modulation of the SLM-640.

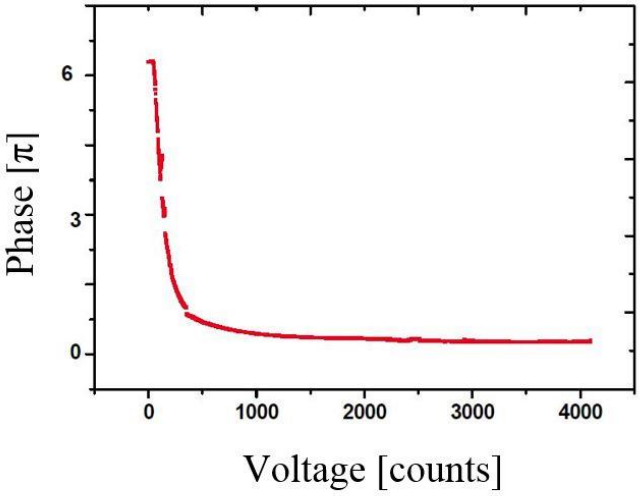

Figure 4.2. Typical phase modulation dependence.

4.2.2 Experimental formation of HG beams

HG modes are a family of stable transverse laser beam modes which are structured perpendicular to the propagation axis. These modes are approximate solutions of the wave equation, valid for weak focusing (paraxial approximation). The well-known normalized HG mode distributions are

$$E_{n_x,m_y}(x,y,z)=\left(\frac{1}{2^{n_x+m_y}\pi n_x!m_y!}\right)^{1/2}\frac{1}{w_z}\times H_{n_x}(\frac{\sqrt{2}x}{w_z})H_{m_y}(\frac{\sqrt{2}y}{w_z})e^{-(r^2/w_z{}^2)}$$
$$\times\exp i\left[\frac{kr^2}{2R_z}-(n_x+m_y+1)\phi_G(z)+kz\right]. \tag{4.4}$$

where k, w_z, R_z, z_R, and H_n are the wave number, beam width, phase front curvature radius, Rayleigh range, and *n*th order Hermite polynomials, respectively. $\phi_G(z) = \arctan(z/z_R)$ is the Gouy phase [108,109].

In the experiment, an 800nm Ti:sapphire laser system (Spitfire, Spectra Physics) with a typical power of about 1W and pulse duration $\sim 50\text{fs}$ was employed. From Eq. (4.2), for constant beam power the self-focusing distance is proportional to the square of the beam size so decreasing the beam size decreases the self-focusing distance. Therefore, to shorten the length for white-light formation we reduced the beam size by using an optical telescope. The setup to change the spatial phase of an initial Gaussian beam to that of a $HG_{0,0}$, $HG_{0,1}$, $HG_{1,0}$, or $HG_{1,1}$ mode is shown in Figure 4.3. HG beams were formed by using the SLM with a required phase mask. Since the SLM was used twice in the experiment to generate HG beams, the power incident on a cuvette with water (taking into account all optical losses) was reduced to 397 mW. For the repetition rate of our laser system of 1 kHz and the pulse duration $\tau = 50 \text{ fs}$ we obtain the input peak power of the laser pulse $P_{in} = 7.94 \text{ GW}$.

Since we used a 1D SLM, to generate the spatial phase of the $HG_{1,1}$ the beam passed the mask twice, both times with the required horizontal polarization. The display of the SLM was divided into three parts with phases shifted by 180°, as is shown in the inset of Figure 4.3, diagram (d). The center of the beam was positioned for the first pass at the border of the 1st and 2nd portions (pixel 118) of the mask, and for the second pass at the border of the 2nd and the 3rd portions (pixel 468) of the mask. Consequently, after two passes in the pairs of the left and right halves and the top and bottom halves of the beam the phases were shifted by 180°.

Although we are able to generate the spatial phases of $HG_{0,0}$, $HG_{0,1}$ and $HG_{1,0}$, except for $HG_{1,1}$, without using the SLM twice, we used for all measurements the fixed geometry, utilized for the generation of HG_{11}, in order to have the same conditions for all HG beams. In this configuration, for obtaining the spatial phases of HG_{10} and HG_{01} beams the phases of the 1st (relative to the 2nd) and the 2nd (relative to the 3rd) portions of the mask were not changed. The liquid crystal phase masks to generate the spatial phases of $HG_{0,0}$, $HG_{0,1}$, $HG_{1,0}$ and $HG_{1,1}$ are shown as (a‑d) in the inset of Figure 4.3, respectively. Then, we recorded the images of the distribution of the laser intensity in HG beams by using a CCD camera with resolution 1392x1040 and pixel size 4.65 x4.65 at the position 1 (the entrance of the cuvette) in Figure 4.3. Figure 4.4 demonstrates the distributions of the laser intensity in the $HG_{0,0}$, $HG_{0,1}$, $HG_{1,0}$ and $HG_{1,1}$ beams created with the phase masks (a-d) as shown in the inset of Figure 4.3.

The $HG_{0,0}$ beam had an intensity distribution of the Gaussian with beam size w_{FWHM}=1.93mm at a full width at half-maximum (FWHM). Using camera pixels, the value of w_{FWHM} is experimentally obtained from image of the $HG_{0,0}$ beam (see panel (a) Figure 4.4) on the beam entrance of the cuvette. Because we modified only the phase within the initial Gaussian beam profile, the resulting HG modes are expected to be superposition of $HG_{0,1}$, $HG_{1,0}$ and $HG_{1,1}$ and higher modes. This can be seen in panels (b‑d) in Figure 4.4 by the appearance of side lobes.

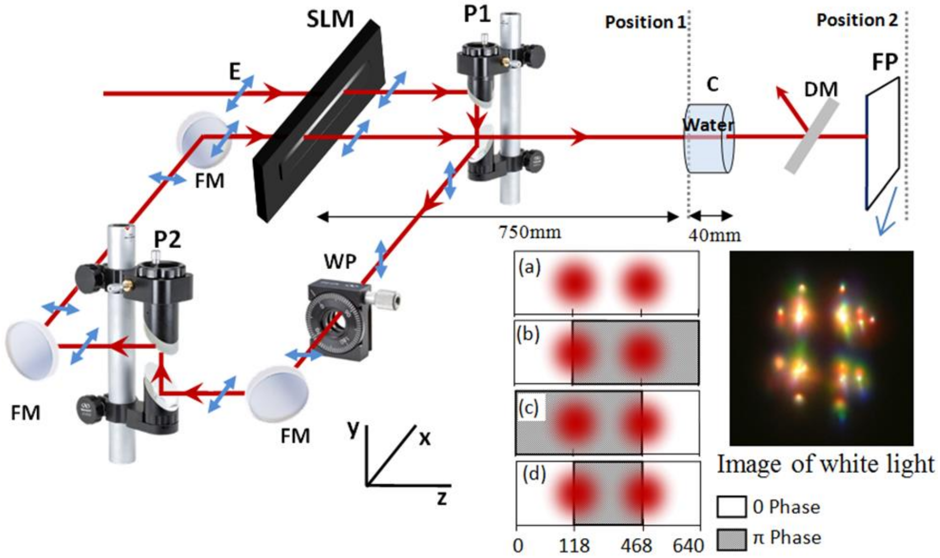

Figure 4.3 Experimental setup to generate HG modes with the 1D SLM and for studies of white-light generation of HG beams in water. Laser radiation from the Ti:sapphire laser enters the setup from the left. Blue arrows (E) show the initial polarization of the beam and the changes of this polarization after the passage of the periscope P1 and a ($\lambda/2$) wave plate (WP). Other optical components used: P2- periscope to adjust the beam height, SLM - spatial light modulator, FM - folding mirror. Notice that in P1 the mirrors are rotated relative to each other in the horizontal plane by 90^o, while in P2 the mirrors are parallel. The incident HG beam enters a 40mm long cuvette (C). A CCD camera for taking images is first placed at position 1 on the entrance of the cuvette to record the generated HG beam. Then the camera is placed at position 2 to record the generated white light on a frosted paper screen (FP) after the radiation of the pump beam is reflected by an 800nm dielectric mirror (DM). The colored picture of $HG_{1,1}$ taken by a color digital camera at position 2 shows the strong white cores with colorful rings (conical emission) in the lower right inset. (a), (b), (c), and (d) present grey-scale encoded phase masks to create $HG_{0,0}$, $HG_{0,1}$, $HG_{1,0}$ and $HG_{1,1}$ beams, respectively.

4.2.3 Calculations for HG modes: Apertures with phase changes

The analytical solutions of the distribution of the laser intensity in HG beams are obtained in the form of the diffraction integral by using the Fresnel approximation. In the Fresnel approximation [110], we have the expression

$$E(x,y,z=d) \cong -\frac{ie^{ikd}e^{i\frac{k}{2d}(x^2+y^2)}}{\lambda d} \iint_{aperture} E(x',y',z=0)e^{i\frac{k}{2d}(x'^2+y'^2)}e^{-i\frac{k}{d}(xx'+yy')}dx'dy' \quad (4.5)$$

Where $E(x',y',z=0)$ is the scalar amplitude of the initial beam at the position of the SLM, $k = 2\pi/\lambda$ is the wave number, λ is the wavelength of the beam, d is the distance in $\hat{z}$ direction after taking the changes of the phase on SLM. When we were generating the HG$_{11}$ mode, there was a 20cm distance (Δd) between the 1st and 2nd passes. Because the distance Δd was much smaller than the Rayleigh range ($\Delta d << z_0$), we neglected the propagation of the beam over the distance Δd . The field before incidence on the SLM was assumed to be $E(x',y',z=0) = E_0 e^{-(x'^2+y'^2)/w_0^2}$ with beam size, w_0 ($w_0 = w_{FWHM} / \sqrt{2\ln 2}$). After the SLM, taking into account changes of the phase imposed by the SLM mask $\varphi(x',y')$, we obtain $E(x',y',z=0) = E_0 e^{-(x'^2+y'^2)/w_0^2} e^{i\varphi(x',y')}$. Consequently, we have the expression,

$$E(x,y,z=d) \cong -\frac{ie^{ikd}e^{i\frac{k}{2d}(x^2+y^2)}}{\lambda d} \int_{-\infty}^{\infty}\int_{-\infty}^{\infty} E_0 e^{-\frac{x'^2+y'^2}{w_o^2}} e^{i\frac{k}{2d}(x'^2+y'^2)} e^{-i\frac{k}{d}(xx'+yy')} e^{i\varphi(x',y')}dx'dy'. \quad (4.6)$$

Since for HG modes, where the neighboring modal lobes are out of phase by π, we can factorize the phase factor as $e^{i\varphi(x',y')} = e^{i\varphi_x(x')}e^{i\varphi_y(y')}$, the integrals over x and y coordinates are independent. The expressions become completely defined after the phases for each HG mode are determined. As an example, the phases for $HG_{1,1}$ mode for x and y directions were defined as

$$\varphi(x') = \begin{cases} \pi \rightarrow -\infty < x' < 0 \\ 0 \rightarrow 0 < x' < \infty \end{cases} \text{ and } \varphi(y') = \begin{cases} 0 \rightarrow -\infty < y' < 0 \\ \pi \rightarrow 0 < y' < \infty \end{cases} . \tag{4.7}$$

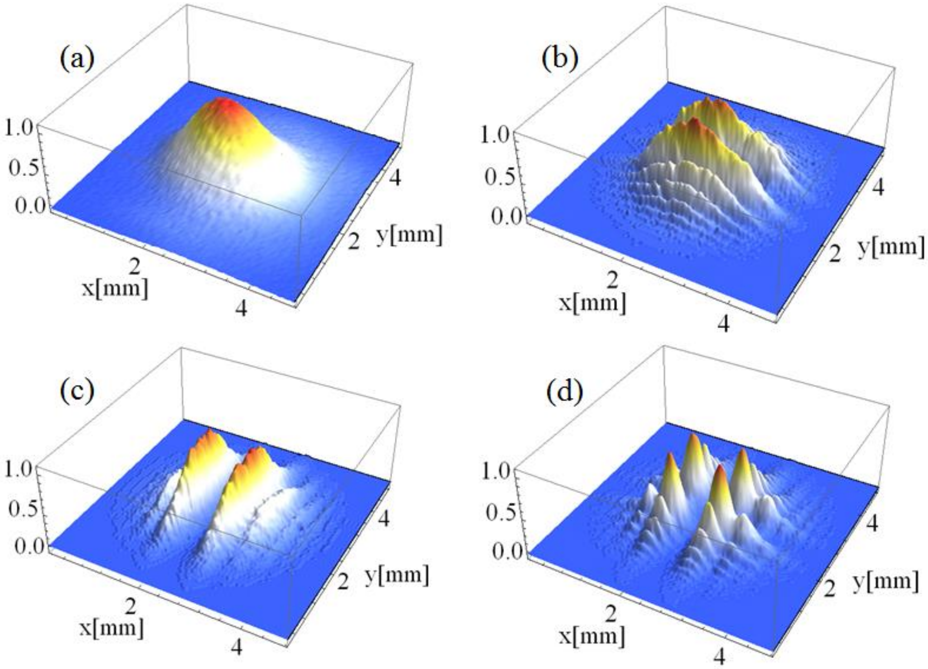

Figure 4.4 The measured distributions of the laser intensity in the $HG_{0,0}$, $HG_{0,1}$, $HG_{1,0}$ and $HG_{1,1}$ beams. Each laser distribution has been peak normalized. HG beams in panels (a-d) are created with the phase masks (a-d) as shown in the inset of Fig. 4.3.

For each mode, we calculated the integrals with appropriate phase factors, and presented them in Figure 4.5. Because we modified only the phase within the initial

Gaussian beam profile (panel (a) in Figure 4.5), the resulting HG beams in panels (b–d) of Figure 4.5 are expected to be the superposition of $HG_{0,1}$, $HG_{1,0}$, $HG_{1,1}$ and higher modes similar to their experimental counterparts in panels (b–d) of Figure 4.4. Numerical decomposition calculations for the modes produced in our setup have shown that for $HG_{0,1}$ and $HG_{1,0}$ phase configuration over 60% and for $HG_{1,1}$ over 40% of the radiation sits in the desired mode; therefore we referred the resultant beams as $HG_{0,1}$ and $HG_{1,0}$, $HG_{1,1}$. For the $HG_{0,0}$ mode the phase is constant across the beam and the decomposition is 100% in the lowest order mode i.e., a Gaussian.

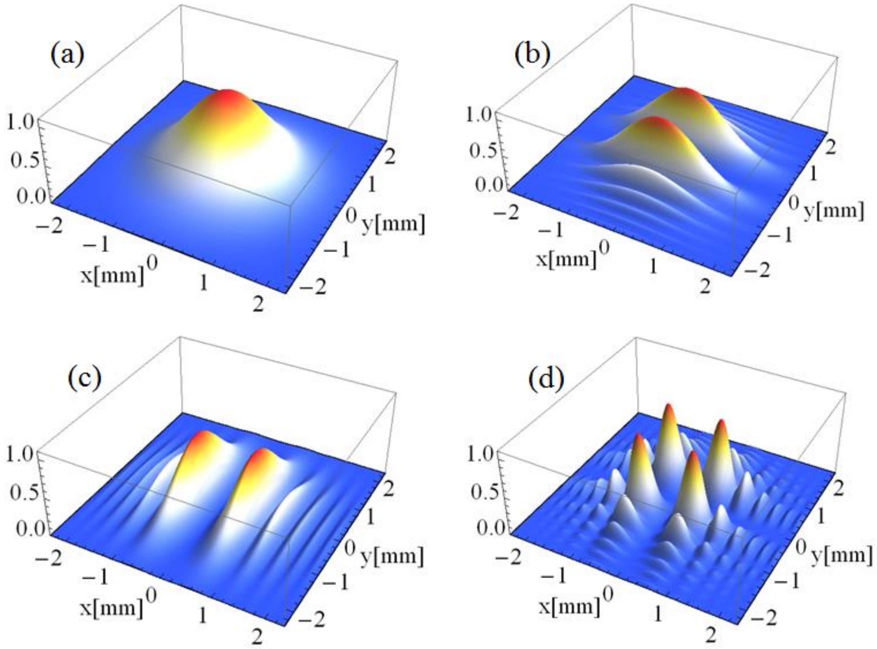

Figure 4.5 The normalized distributions of the laser intensity in the cases of $HG_{0,0}$, $HG_{0,1}$, $HG_{1,0}$ and $HG_{1,1}$ beams calculated by the integrals with appropriate phase factors (Eqs.(4.7)).

4.2.4 Experiments on white-light generation of HG beams in water

In order to generate white-light in water, the created $HG_{0,1}$, $HG_{1,0}$, or $HG_{1,1}$ beams pass through a water cuvette of 40 mm length placed at distance 750 mm from the SLM as shown in Figure 4.3. The images of white-light in water are projected on a frosted paper screen. A narrowband 800 nm mirror was inserted before the frosted paper to deflect the radiation of the pump beam and to obtain images of the generated white-light, avoiding also saturation of the CCD camera. The camera was placed at position 2 to record the white-light on the frosted paper screen.

Panels (a‑d) in Figure 4.6 show the images of the distribution of the measured light intensity on the CCD for all HG modes generated at the fixed geometry. No significant white-light formation took place in water for the $HG_{0,0}$ mode (panel (a) in Figure 4.6). However, if the phase masks, described above were imposed on the beam and the corresponding $HG_{0,1}$, $HG_{1,0}$ and $HG_{1,1}$ modes were generated, then the white-light generation took place. The alignment of white-light emissions closely follows the peaks of the intensity in the cross section of the respective laser beams (Figure 4.4). For instance, for $HG_{0,1}$ and $HG_{1,0}$ modes the white-light emissions are formed along the crests of the intensity distribution, and for the $HG_{1,1}$ mode the white-light emissions are concentrated in four lobes near the maxima of the intensity.

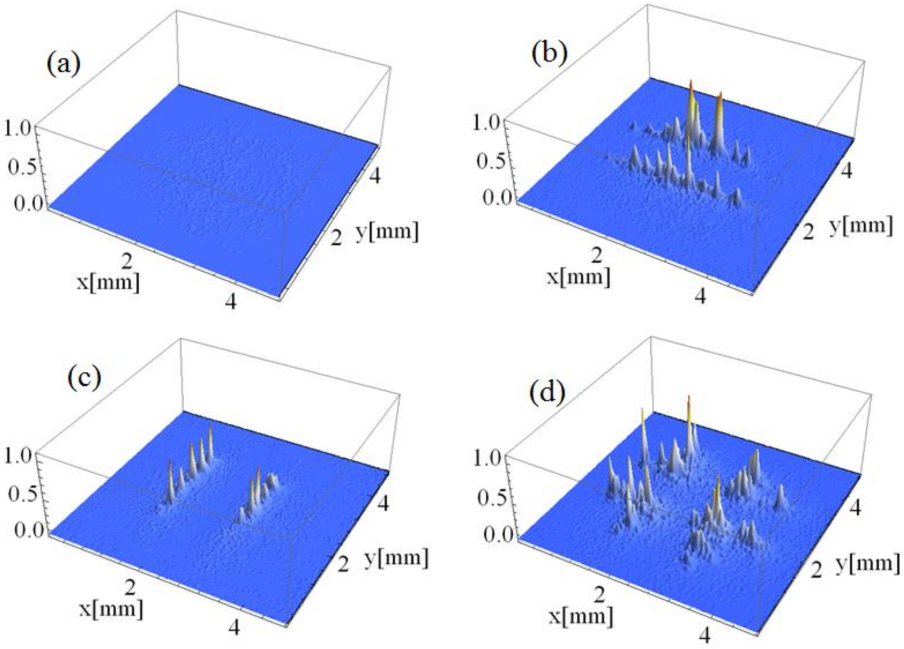

Figure 4.6 The measured white-light intensity distributions on the CCD for all HG modes generated at the fixed geometry.

4.3 Discussion

The generation of white-light that we observed can be justified in the following way. The resulting transverse intensity profiles of HG beams consist of several bright spots (intensity lobes), so we can assess strong white-light generation of the resulting HG beams by calculating the critical powers and self-focusing distances corresponding to these lobes. To trace these parameters for each of the observed lobes we presented each of the observed intensity distributions in top-view panels in Figure 4.7.

The Gaussian beam ($HG_{0,0}$) on the entrance of the cuvette has a beam radius w_a =1.16mm at 1/e value of the peak intensity (see panel (a) in Figure 4.7). The value of w_a

is obtained from the beam size $w_{FWHM} = 1.93\text{ mm}$ at FWHM by using the relation $w_a = w_{FWHM} / 2\sqrt{\ln 2}$. For the HG$_{1,1}$ beam configuration the strong white-light generations are concentrated in four central lobes near the maxima of the intensity. We assume that the intensity distribution of each lobe can be approximated by a Gaussian profile (see panel (d) in Figure 4.7). We measured the radius $w_d = 0.17 w_a$ for one of the lobes of HG$_{11}$ beam profile. For HG$_{0,1}$ or HG$_{1,0}$ beams the white-light generations are produced along the crests in the intensity distribution (see panels (b and c) in Figure 4.7). One of the crests of HG$_{0,1}$ has beam sizes at 1/e levels of 1.16mm and 0.19 mm in *x* and *y* directions of the crest respectively. One can count 5 well pronounced and partially overlapped intensity distribution peaks along x direction and choose one of the intense lobes on the one of the crests of HG$_{0,1}$ as a Gaussian shaped sub-beam with a radius w_b =0.19 mm. Similarly, for HG$_{1,0}$ the chosen Gaussian lobe radius is $w_c = w_b$. Again, the values of the beam radii refer to the 1/e levels of the lobes in the images. By using the radii and maximal intensities of the main lobes of HG$_{0,1}$, HG$_{1,0}$ and HG$_{1,1}$ beams, we calculate the corresponding input powers $P_{int}^a = 40.81 P_{int}^b = 60.41 P_{int}^d$ and $P_{int}^c \cong P_{int}^b$.

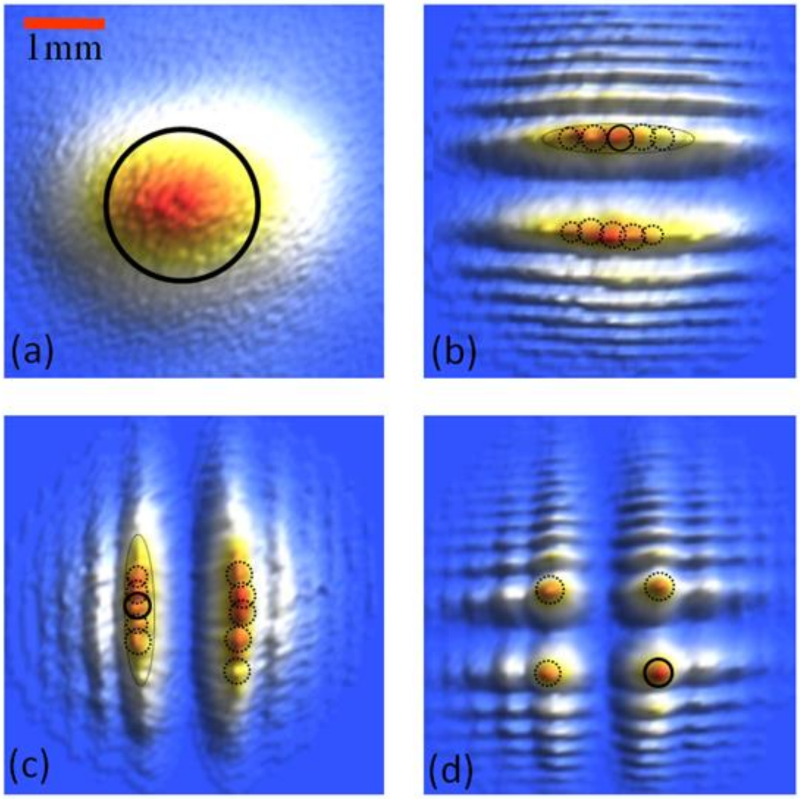

Figure 4.7 The top view of the experimentally measured distributions of the laser intensity for the $HG_{0,0}$, $HG_{0,1}$, $HG_{1,0}$ and $HG_{1,1}$ beams from panels (a − d) of Fig. 2 . The intensity lobes used for the calculation of the critical power and self-focusing distance of HG beams (main lobes) are shown with black solid circles in panels (a − d), drawn at FWHM values of the peak intensity; the dotted lines show the same for other peaks in the intensity distributions.

The critical power for water was calculated as 3.60 MW by using Eq. (4.1). Inserting the input powers and radius of the lobes into Eq. (4.2), we obtained the self-focusing distances $L_{sf}^{a} = 11$ cm , $L_{sf}^{b} \cong L_{sf}^{c} = 2.1$ cm and $L_{sf}^{d} = 2.6$ cm for the lobes with the highest intensities (main lobes), shown by solid circles in panels (a–d) in Figure 4.7. We can see that for the Gaussian beam, no significant white-light in water can be expected, since the self-focusing distance $L_{sf}^{a} = 11\ \mathrm{cm}$ of $HG_{0,0}$ is longer than the cuvette length 40mm. In contrast, the self-focusing distances of the main lobes of $HG_{0,1}$, $HG_{1,0}$ and $HG_{1,1}$ beam are shorter than the cuvette length, so changing the beam configuration to $HG_{0,1}$, $HG_{1,0}$ and HG_{11} beams resulted in the generation of white-light.

4.4 Conclusion

In this study, we presented how to generate the beams exhibiting phase discontinuities and steeper intensity gradients by imposing spatial phase masks on the initial Gaussian beam. Namely, $HG_{0,1}$, $HG_{1,0}$ and $HG_{1,1}$ and higher modes were produced by using a 1D spatial light modulator. The laser intensity distributions for the beams having step-wise spatial phase variations were described with the Fresnel-Kirchhoff integral in the Fresnel approximation and found to be in good agreement with experiment.

When the spatial phase of the Gaussian beam (showing no significant white-light generation) was changed to those of a $HG_{0,1}$, $HG_{1,0}$ or $HG_{1,1}$ mode, we observed significant production of white-light in the main lobes of the intensity distribution. Because self-focusing is known to play an important role in white-light generation, by calculating the self-focusing lengths of the resulting transverse intensity profiles we have qualitatively confirmed this effect. The calculations with experimentally obtained parameters of the beams confirmed that the resulting transverse $HG_{0,1}$, $HG_{1,0}$ and $HG_{1,1}$ intensity configurations have self-focusing distances shorter than the cell length, while the Gaussian beam requires a longer cell for strong white-light production.

There is only one beam on the output of the setup so the lobes “sub-beams” in this beam are mutually coherent. Coherence of white light sources from single laser beam was studied and confirmed in [111]. The coherence of the white light radiation is an important aspect, and the beams from the lobes of coherent white-light radiation can be used for spectroscopy and pump-probe experiments. This aspect is the subject of our future studies.

CHAPTER V

WHITE-LIGHT GENERATION CONTROL WITH CROSSING BEAMS OF FEMTOSECOND LASER PULSES[3]

In this chapter, the effects of variation of the white-light generation in two interacting beams are studied. We showed that depending on the relative delay of two interacting intense femtosecond laser pulses the white-light generation can be enhanced or suppressed. With a decrease of the relative temporal delays between the laser pulses an enhancement of the white-light output was observed, which at small delays was replaced by a suppression of white-light generation. The level of suppressed white-light output could be lower than the initial level of output, corresponding to large delays, when pulses do not overlap in time. The enhancement of the white light generation happens in the beam that is lagging. Based on the observation results, we explained these effects of variation of the white light generation.

5.1 Introduction

The controlling of light by light is a fascinating possibility. Several physical mechanisms were previously considered, including nonlinear optical interaction[112,113], laser-induced Kerr effect [114-118] and birefringence[119]. Such non-destructive and reversible mechanisms of the interaction of laser pulses form the basis for development of ultrafast optical gating techniques [120-122], including shutters and pulse pickers. The

---

[3] A. Kolomenskii, N. Kaya, J. Strohaber, G. Kaya, H. Schroeder, and H. Schuessler, “White-light generation control with crossing beams of femtosecond laser pulses,” in preparation to submit for publication.

advent of the femtosecond laser science brought such advantages as high intensities and an extremely fast switching time of these optical devices, compared to their electronic counterparts. An intense pulse propagating in the medium can experience self-focusing [104,123,124] with modification of its spectrum due to nonlinear optical processes [125-128]. The availability of femtosecond laser pulses renewed interest in self-focusing phenomena [33] and development of beam instability[129], related to filamentation[24,32,130-132], white light generation [19,20,22,24,90,99,106,133] and conical emission[134]. The white light generation is usually accounted for by self-phase modulation[127,135], however stimulated Raman scattering[136], parametric four-wave mixing[137-140], and cascading of these effects as the beam propagates can also contribute to generation of a supercontinuum. The question we are interested in is how the interaction of two beams affects these processes.

It was shown experimentally that two beams interacting in gas [141,142] or in a liquid[143], can exchange their energy and mutually transform their spectra. In isotropic solid materials, such as glass, the nonlinear refractive coefficient is typically much larger than in a gas, and therefore the above mentioned optical phenomena, provided similar laser parameters, develop on shorter distances. The interaction of two intense beams affects not only the initial beams themselves, but also the resulting spectral transformation. However, the effects of the two-beam interaction on white-light generation were not investigated. We show that depending on the relative delay of two interacting intense femtosecond laser pulses the white-light generation can be enhanced or suppressed. The white light generation closely correlates with the number of filaments formed. Thus, the latter appears as an indicator of the local beam intensity.

5.2 Experimental setup

In the experiment (see Figure 5.1) we used amplified femtosecond laser pulses (Spitfire, Spectra Physics) with 50 fs duration and initial energy up to 1 mJ at 1 kHz repetition rate. The pulses went through a 2-3 mm diameter aperture, which limited the laser power, and then were focused by a curved mirror with a focal length of 2.5m, split into two sub-beams, and propagated in two optical arms with approximately equal optical paths. The optical path of one of the arms, labeled "movable arm" could be varied relative to the other arm, labeled "fixed arm" by a computer-controlled motorized translation stage (ESP300, Newport) with a temporal resolution of 0.33fs (0.00005mm). The sample had a parallelepiped shape and was made of a flint glass with dimensions 32.27 mm × 15.84 mm × 12.60 mm, the refractive index n=1.81 and density 3.49 g/cm^3. The two sub-beams in front of the sample had close typical powers about 100 mW and crossed in the sample at an angle of 2.68 deg. In a special series of experiments the crossing angle was varied from 1 to 8 deg. The IR (around 800 nm) radiation and white-light were separated by a dielectric mirror, effectively transmitting light from 400 to 600 nm and reflecting light at around 800 nm. We measured the power of the IR 800 nm radiation and that of white-light in the movable and fixed arms depending on the relative delay with an Ophir power meter. Alternatively, IR radiation and white light were imaged by projecting them onto a CCD camera. The spectra were measured by an Ocean Optics spectrometer using an integrating sphere.

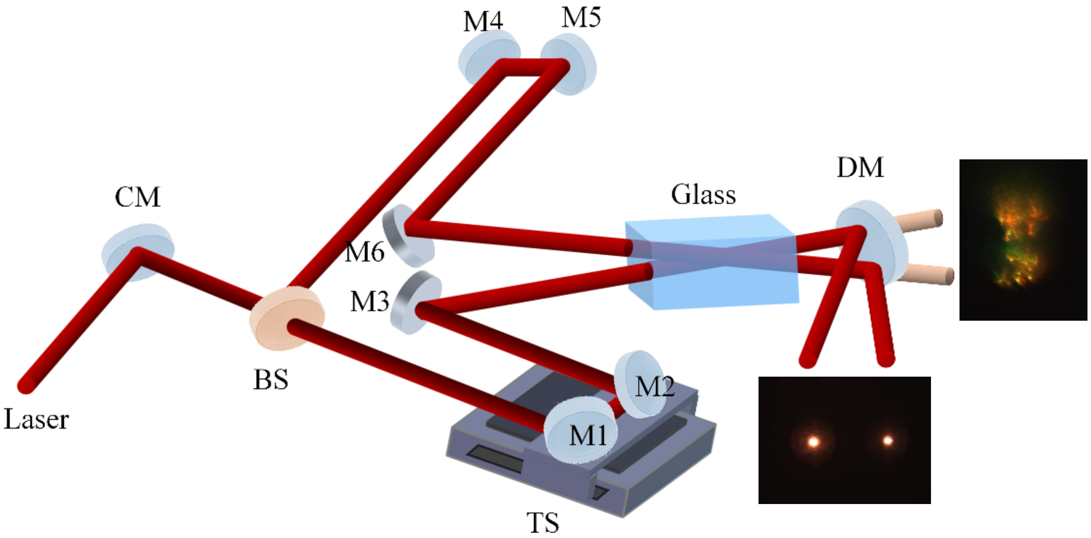

Figure 5.1 Experimental setup: the delay between pulses in two optical arms is changed by a translation stage. The two beams cross in the sample. An input aperture was used for adjusting the power of the beams; a typical diameter of the aperture is 2.7 mm for beams producing filamentation in our case. The first incoming mirror is curved with the focal length 2.5 m. A dielectric mirror separates as shown in the inset an IR radiation around 800 nm and generated white-light, which were measured or imaged on a CCD camera depending on the delay between optical paths in two arms. Shown are: CM -curved mirror, BS - beam splitter, TS - translation stage, M1- M6 fast silver mirrors, DM - dielectric mirror.

5.3 Results

First, we describe results, obtained with a flint glass sample. Since the power of white-light closely correlated with the number of filaments, we took a series of pictures of the cross-section of the beams with formed filaments taken with equal time intervals of 6.6 fs (Figure 5.2). In each picture the upper colored spot shows filaments in the movable arm and the lower spot corresponds to the fixed arm. The right panel shows a magnified view of the selected area, so that separate filaments can be distinguished and counted. From the images we observed that the number of filaments experienced variations in both arms, when the delay was changed between the arms. We define the delay time as the arrival time of the pulse in the fixed arm minus the arrival time of the pulse in the movable arm. The number of filaments in the movable arm increased at negative delays then dipped near zero delays. The number of filaments in the fixed arm qualitatively showed a behavior reversed with respect to the delay time compared to the movable arm.

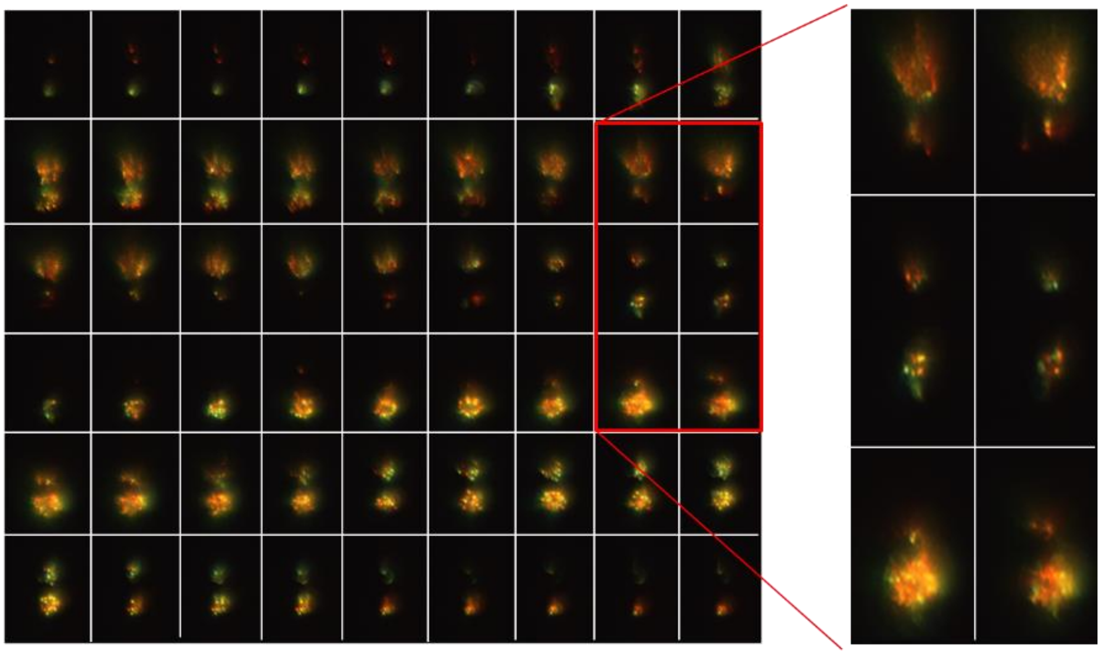

Figure 5.2 Images of beam cross-sections with filaments taken with 6.6 fs intervals of time delays increasing from top to bottom and from left to right: left panel shows the whole series of images; the right panel shows a magnified view of the area in the red rectangle, where light produced by separate filaments can be discerned.

The power output of white-light was measured in each of the arms by alternatively blocking half of the output plane; the total amount of white-light output produced in both arms was also measured. When the delay was changed the amount of the generated white-light experienced variations in both arms (Figure 5.3). The power measured in the movable arm peaked at negative delays then dipped near zero delays even below the initial level and showed a minor peak at positive delays. The white-light output in the fixed arm qualitatively showed a behavior reversed with respect to the delay time compared to the movable arm. Consequently, the amount of white light production increased for pulse that was lagging, and the total output of white-light of both arms exhibited two well pronounced peaks with a deep valley in between them. It was established that the appearance of minor peaks in each of the arms was a result of partial overlap of the outputs of two arms and measuring these outputs at larger distances from the sample could reduce them. Around zero delay, the white-light level goes to the level that is below the level found for large delays, when pulses do not overlap.

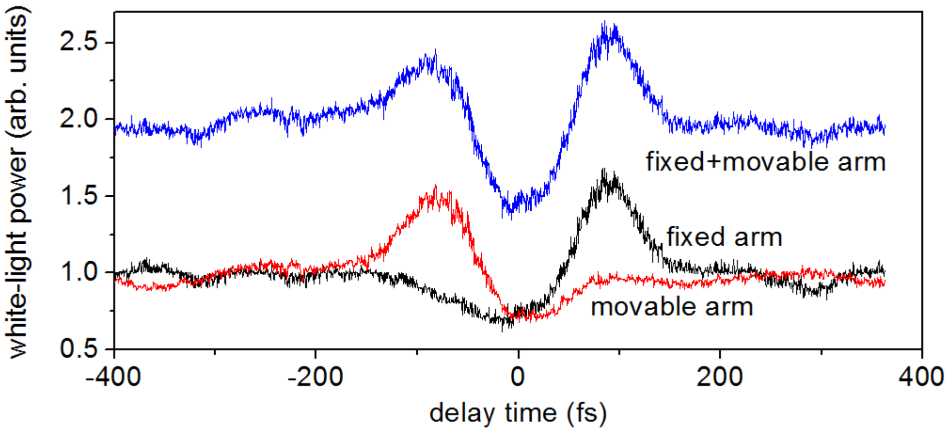

Figure 5.3 Variations of the white-light vs. relative delay of two beams; upper trace (blue) is the total amount of white light measured in both arms, the black trace is the power measured in the fixed arm, and the red trace is the power measured in the movable arm.

A more detailed spectral information on the white-light generation depending on the delay was obtained with a spectrometer. The output beams were sent into an integrating cavity through a small opening, and a tip of an optical fiber inserted in a side wall of the integrating cavity, collected light that was then analyzed with an Ocean Optics spectrometer. The measured spectrum (see Figure 5.4) and the result of the integration of the spectrum interval in the range 400-700 nm, presented on the lower graph, show a well pronounced suppression of the white light spectrum in the vicinity of the zero delay.

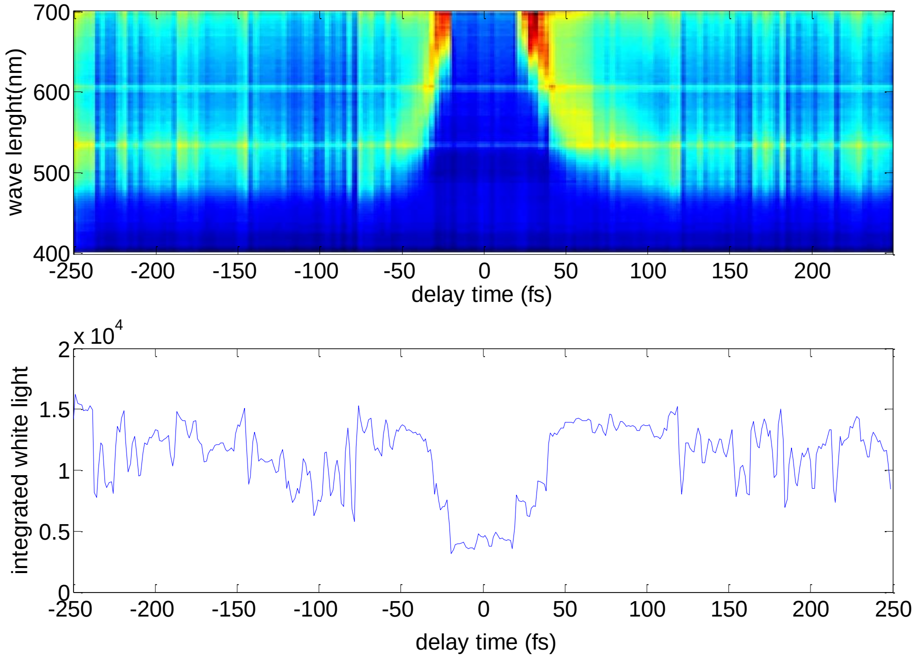

Figure 5.4 Spectral observation of white-light enhancement and suppression: the upper graph shows in false colors a plot of the spectral distribution of the two beams in the range 400-700 nm after their interaction in the sample as a function of the relative delay; the lower graph depicts the total (integrated) amount of white light also vs. time delay. An enhancement of the spectral components at negative delays and for positive delays and a strong suppression of the spectrum near zero delay can be clearly seen, which result also in the integrated white-light variations (lower graph).

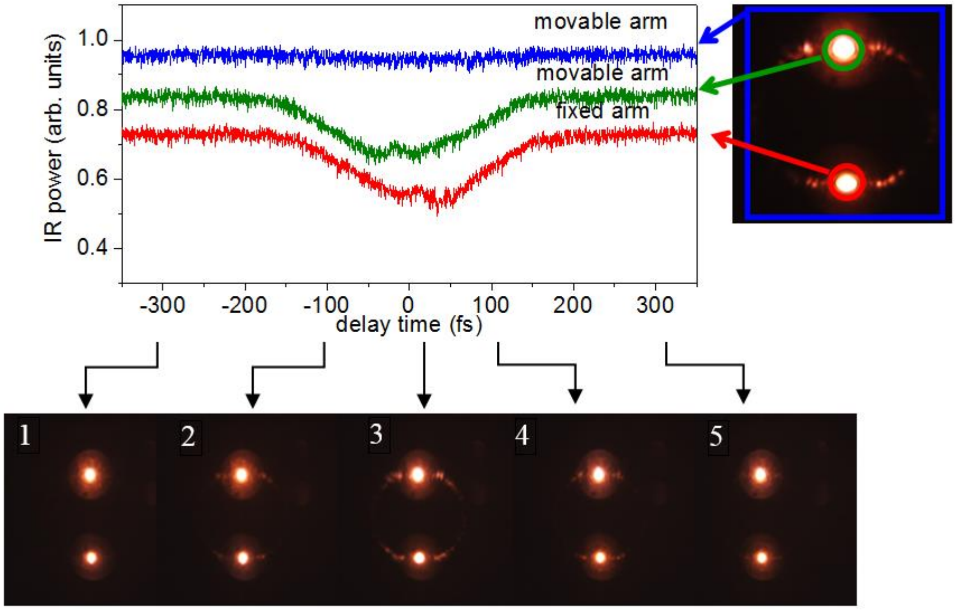

Figure 5.5 IR beams after interaction: right panel shows a magnified view of the images of the cross sections of beams on the CCD camera in the movable arm (top) and in the fixed arm (bottom) at zero delay; left panel shows the dependence of the measured power in the circled areas vs. delay in movable and fixed arms (the curves shifted up for better viewing). The bottom panel shows images taken at large delays (1, 5), at delays corresponding to maximal white-light output (2, 4) and zero delay (3). The starting points of arrows indicate respective delays on the time scale.

To better understand the correlation of the interaction of the beams with the white-light generation, we imaged and measured beam cross-sections with the IR radiation transmitted through the sample in intervals of time delays, which revealed in the beam cross-sections a redistribution of the intensity, especially pronounced near zero delays (Figure 5.5). When only the power of the circled central part of the beams was measured by inserting an aperture, the power values for both of them exhibited a dip at close to zero delays (green and red traces in Figure 5.5).

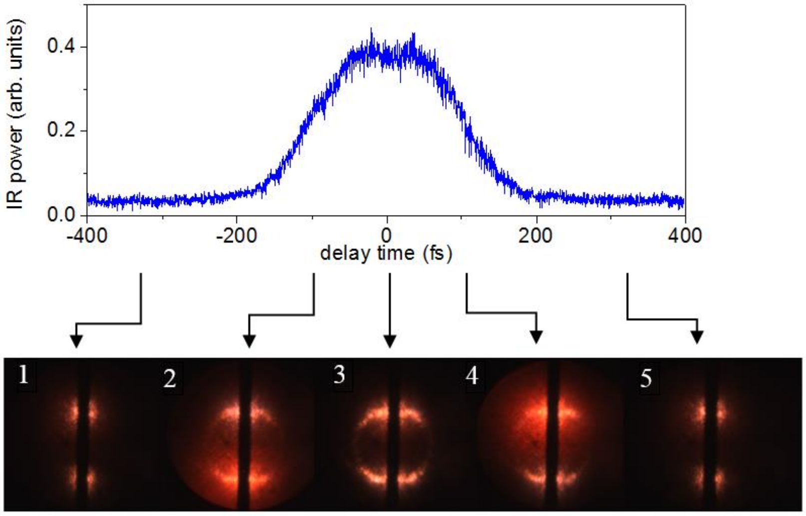

Figure 5.6 The dependence of the IR power on delay and images of the IR beams with the central parts blocked taken at large delays (1, 5), at delays corresponding to maximal white-light output (2, 4) and zero delay (3). The starting points of arrows indicate respective delays on the time scale.

When the power in a larger area, covering the whole output of one beam (and surrounded by a rectangle in Figure 5.5) was measured the output was almost constant. Thus, some of the energy of the beams was deflected to the peripheral area with well pronounced arc-shaped wings extending from the central part of the beam. Additional measurements of the total IR output with the central spots of the beams blocked (Figure 5.6) indeed showed a maximum at delays close to zero. The interaction of the beams depends on their mutual orientation of polarizations. The decrease of the power in the central region of the beams is the largest for parallel polarizations and decreases when the angle between polarizations increases to 90 deg (Figure 5.7).

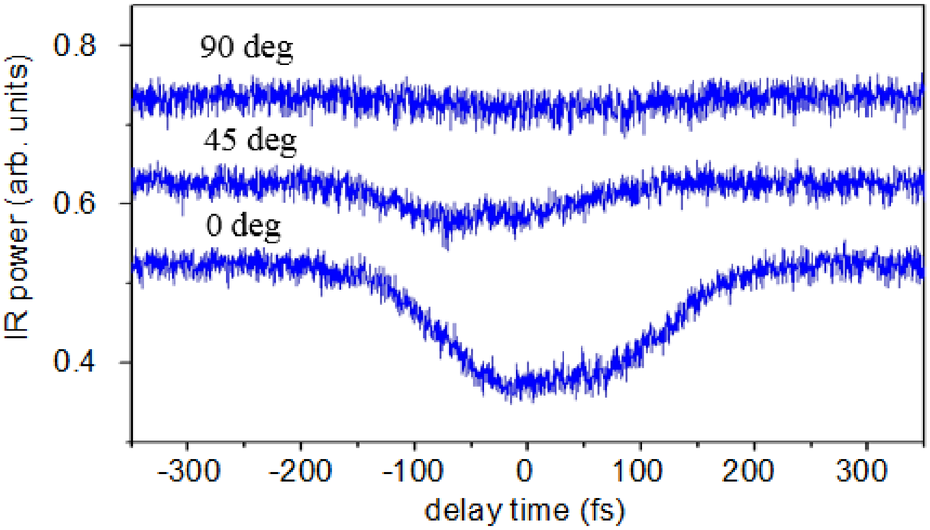

Figure 5.7 Variations of the IR radiation in the central spot of the fixed arm for different angles between polarizations of the beams in the two arms. The curves are shifted vertically for better viewing.

5.4 Discussion

We observed two main effects due to two beam interaction: (1) the white-light generation can be increased or decreased by varying the relative delay of two interacting pulses, propagating at some angle, and at certain conditions the contrast of this process is so high that it can be described as "switching" white-light on and off; (2) the changes in the intensity distributions of the beams were observed with appearance of arc-shaped lateral extensions, especially pronounced at small delays.

We will start the discussion with the second effect. It is known that in the diffraction of a beam on a transparent dielectric cylinder a series of arcs centered around the cylinder appears in the forward directions, which are due to a reflection from the cylinder surface and transmission[144-146]. In the latter case the cylinder also works as a one-dimensional lens. For a cylinder of a small size also diffraction on a cylinder plays noticeable role. In our experiments (Figure 5.5 and Figure 5.6) we see arc-shaped formations going from one beam to the other. This suggests that the interaction of the beams creates a perturbation of the refractive index that extends along the internal bisector of the angle formed by the two crossing beams. It is assumed that the elongated central structure with higher intensity leads to corresponding change in the refractive index, and then each beam experiences interaction with this structure similar to the interaction with a dielectric cylinder. Since the variations of the refractive index are gradual, mostly the transmission of the beams can be expected to lead to formation of arc-shaped lateral extensions in Figure 5.5 and Figure 5.6.

At the conditions of our experiment the self-focusing threshold 0.53 MW (for $n_0 = 1.81$, $n_2 = 10^{-15} \text{cm}^2/\text{W}$) is exceeded manyfold. Therefore the self-focusing length of the beams is relatively small.

Consequently, small-scale perturbations of the beams lead to development of filaments[15,147]. At the conditions close to filament formation threshold at the length of the sample even a relatively small increase of the laser intensity will lead to appearance of filaments. In our experiments, the increase of the refractive index in the high-intensity central structure serves as a cylindrical lens, providing necessary initial increase of the intensity for development of filaments.

However, if the mutual beam refraction-diffraction process reduces (as is seen in Figure 5.5- Figure 5.6) their peak intensity, which lies in the middle of their cross sections, diminishes as well and then the filamentation process is suppressed, as is observed at small delays (Figure 5.2, Figure 5.3 and Figure 5.4).

An interesting aspect of the beam interaction is its dependence on the mutual orientation of polarizations. This points out to an important role of interference in this interaction. For beams with perpendicular polarizations the increase of the intensity in the region of the intersection corresponds to their summation. The laser beams with the same orientation of polarizations can effectively interfere, reaching quadrupled values of a single beam intensity at the peaks. While propagating in the glass or quartz laser pulses experience significant dispersion and acquire a chirp. This is confirmed by measuring the laser pulse durations at the entrance face of the sample τ=57fs and after passing through the sample τ=83fs. For dominating linear chirp one can assume the frequency shift of the beams at the crossing is proportional to the delay time.

If the two beams with slightly shifted wavelengths λ_1 and λ_2 cross then they can interact coherently on a coherence length $L_c = \lambda^2 / \Delta\lambda$, where $\Delta\lambda = |\lambda_2 - \lambda_1|$. When the interaction length L, which is determined by the beam diameters d and the crossing angle θ, $L = d / tan(\theta / 2)$, is longer than L_c the intensity along the central structure will oscillate together with the output of the scattered light, which will be maximal when the interaction length is a multiple of the coherence length according to the Maker's formula[148], so that the maximum oscillates $\propto [sin(kL)]^2$, where $k = 2\pi / \lambda$. Therefore, one can expect oscillations of the beam mutual scattering with a variation of the crossing angle, resulting also in different levels of the suppression of the white light generation as was observed in the experiment. With an increase of the interaction angle the coherence length across the beams, $L_{c\perp} = \lambda / (4 sin(\theta / 2))$, will decrease leading to a faster decrease of the intensity across the central structure, thus resulting in weaker mutual refraction and diffraction of the beams.

5.5 Conclusion

We observed the effect of variation of the white light generation in two interacting beams. With a decrease of the relative temporal delays between the laser pulses an enhancement of the white-light output was observed. This enhancement was changed to a suppression of white-light generation in the interval of delays close to zero. The level of suppressed white-light output could be lower than the level of output at large delays, when pulses do not overlap in time. The enhancement of the white light generation happens in the beam that is lagging. The patterns of IR light distributed around the main beams in arc-shaped extensions were observed and are more pronounced at small delays, where the powers of the central parts of IR beams exhibit dips. When beams start interfering, following a decrease in the delay, this initially leads to an increase of the intensity in the interaction region, inducing respective changes in the refractive index due to the Kerr effect. As a result, after beams pass each other they experience cylindrical lensing effect, leading to a local increase of intensity and enhanced filament formation. However, with a further decrease of the delay, the redistribution of the laser intensity to the refraction/diffraction side extensions becomes significant and results in the decrease of both the peak intensity and the number of filaments and, consequently, in a lower level of the generated white-light.

CHAPTER VI

FILAMENT PROPAGATION LENGTH OF FEMTOSECOND PULSES WITH GAUSSIAN AND BESSEL BEAM MODES[4]

This chapter shows an application of holographic method, which was used to create Gaussian and Bessel-Gaussian beams with the same peak intensity, pulse duration and the size of the central part of the beams. The comparison of the filament propagation lengths of femtosecond pulses with these different transverse modes is given first. This is followed by a more detailed study of the dependence of the filament propagation length on the number of radial modal lobes to better understand the Bessel Gaussian beam propagation.

6.1 Introduction

Light filaments formed by femtosecond laser radiation propagating in nonlinear media [149,150] facilitate a number of applications, including remote sensing [53,151,152], attosecond physics [153-155], and lightning control [156]. In such settings, extended filaments are desirable, but although various techniques aiming to prolong their length have been explored [157-159], the substantial extension of optical filaments continues to attract considerable interest, and much still remains to be understood [160].

Since filamentation is a result of the prevailing of the Kerr self-focusing of an intense pulse over the defocusing by the self-generated weak plasma and the effect of free electrons [161], one can expect that different incident laser transverse modes should also

---

[4] N. Kaya, M. Sayrac, G. Kaya, Y. Boran, J. Strohaber, A. A. Kolomenskii, and H. A. Schuessler, "Filament propagation length of femtosecond pulses with Gaussian and Bessel-Gaussian modes", in preparation to submit for publication.

exhibit different filament propagation dynamics. The ideal Bessel beams are known to be diffraction-free beams when they propagate in vacuum [162,163]. Although ideal Bessel beams do not exist, the use of approximate or quasi-Bessel beams has long been suggested in diverse areas of optical physics, since such beams maintain long propagation lengths in optical media by virtue of the strongly suppressed diffraction of their central lobe over long distances [164,165].

When a Bessel beam is compared to a Gaussian beam with the same beam diameter, it shows a remarkable resistance to diffraction during propagation [166]. Recent theoretical studies on filamentation dynamics in Ar gas of intense femtosecond beams with different transverse modes have shown that the cross-sectional profile of the laser beam in Bessel modes remain undistorted [167] during propagation over long distances, the outer part of the Bessel beam serves as an energy reservoir for the filament that is formed around the central portion [168]. Recently, Scheller and colleagues have experimentally shown that the propagation of a femtosecond laser filament in air can be substantially extended by an appropriate use of a surrounding auxiliary dressing beam, continuously supplying energy to the filament [169]. It is a seminal idea that the length of the energy transmission by the filament can be strongly affected by the transverse profile of a beam. In our work, instead of using an annular dressing beam with a Gaussian filament seed beam, as a new approach, we used a specifically shaped input beam, a Bessel beam, which has an annular structure. Therefore, we experimentally investigate filament propagation dynamics in water with intense femtosecond pulses of Gaussian beam and Bessel-Gaussian beam profiles with similar peak intensities, pulse durations, and beam diameters. Then particular emphasis is placed on the incident Bessel-Gaussian beams and a more detailed study of the mode structure on its propagation.

In liquids the Kerr nonlinearity is about two orders of magnitude larger than in gases [170], and therefore the nonlinear effects develop on a shorter distance and require less power. The reason to choose water is the available laser power and available space in experimental size.

6.2 Experimental details and results

The transverse modes of Gaussian and Bessel-Gaussian are described respectively by the following spatial field amplitude:

$$E_{Gaussian}\ \ r,z=0,t=0\ \ =E_0e^{-r^2/w_0^2} \tag{6.1}$$

$$E_{Bessel-Gaussian}\ \ r,z=0,t=0\ \ =E_0\,J_0\ \ \alpha r\ \ e^{-(\beta r)^2} \tag{6.2}$$

where E_0 is the peak amplitude, w_0 is the radius of the beam profile at the $1/e^2$ level of intensity, and J_0 is the zero order Bessel function. The constants α and β are chosen in such a way as to make the FWHM of the central lobes of the different transverse modes equal (for the Gaussian beam, $w_{FWHM}=w_0\left(2\,ln|2|\right)^{1/2}$).

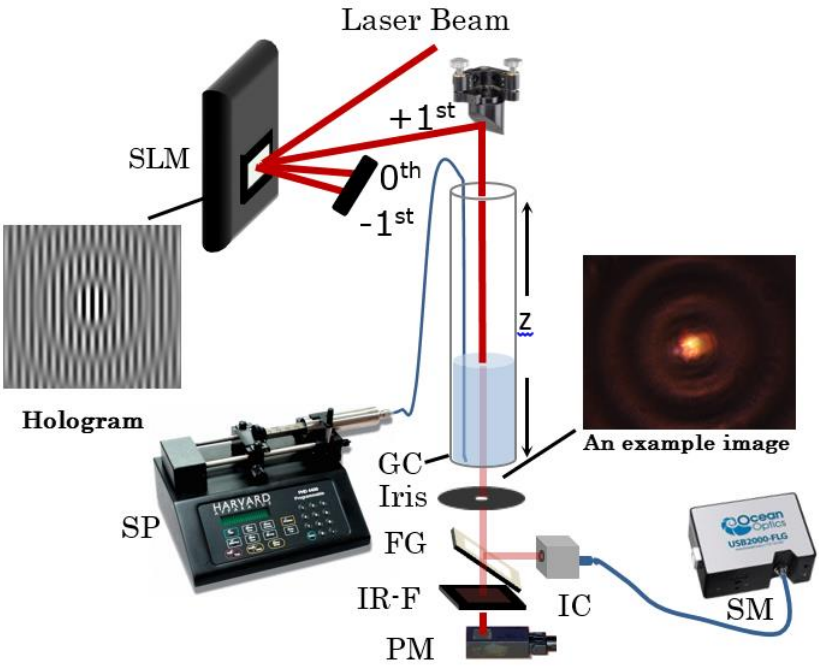

Figure 6.1 Experimental setup: SLM, spatial light modulator; SP, syringe pump; GC, glass cell with an optical window; FG, flat glass (4% reflectivity at 45 deg.); IR-F or ND-F, infrared filter or neutral density filter to measure the incident beam; PM, power meter; IC, integrated cavity; SM, spectrometer. The inset under the SLM is an example hologram used to create a Bessel-Gaussian beam. The other inset shows image of a Bessel-Gaussian beam with filaments core taken a color CCD camera with necessary filters and attenuators.

Laser modes were created from an initial Gaussian beam of a Ti:sapphire laser system (pulse duration of ~50 fs, central wavelength of 800 nm, and an output energy of 1 mJ per pulse at a 1 kHz repetition rate) by using computer-generated holograms [63,171] displayed on a liquid crystal spatial light modulator (Hamamatsu LCOS-SLM X10468-2). The SLM had a resolution of 800×600 pixels (16 mm × 12 mm), and a maximum reflectivity of >95% for radiation between 750 nm and 850 nm. Figure 6.1 shows an illustration of the experimental setup used. The laser beam illuminates the SLM with a phase-amplitude encoded hologram set by a computer to produce a desired optical beam in the 1st diffraction order. Such grayscale computer-generated holograms for Gaussian and Bessel-Gaussian beams, prepared with a MATLAB code, were displayed on the SLM's LCD via a digital visual interface connection. An illustration of the computer-generated hologram used to produce a Bessel-Gaussian beam in the first diffraction order is shown in the inset of Figure 6.1. We note that the SLM creates a quasi-Bessel amplitude-phase distribution that together with the Gaussian distribution of the incident beam produces a Bessel-Gaussian beam, which has a limited cross section and a finite number of lobes.

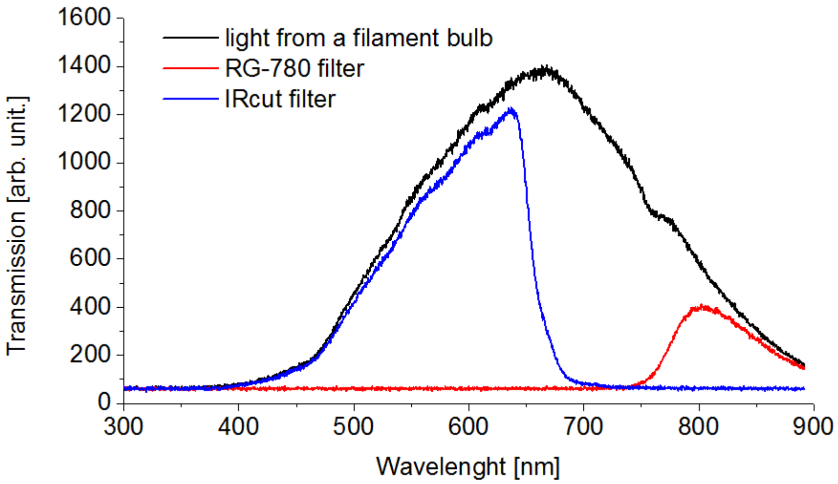

Figure 6.2 Optical filters selectively transmitted light having certain a particular range of wavelengths.

With all optical losses, including the loss on the SLM, which employs off-axis holography to generate the beam modes, the incident power of the Gaussian beam mode with a 300 µm diameter at FWHM on the water cell was measured as 270 mW at the entrance of the cell. Consequently, for the repetition rate of our laser system (1 kHz) and the pulse duration (~50 fs), we obtained an input peak power of 5.4 GW per pulse.

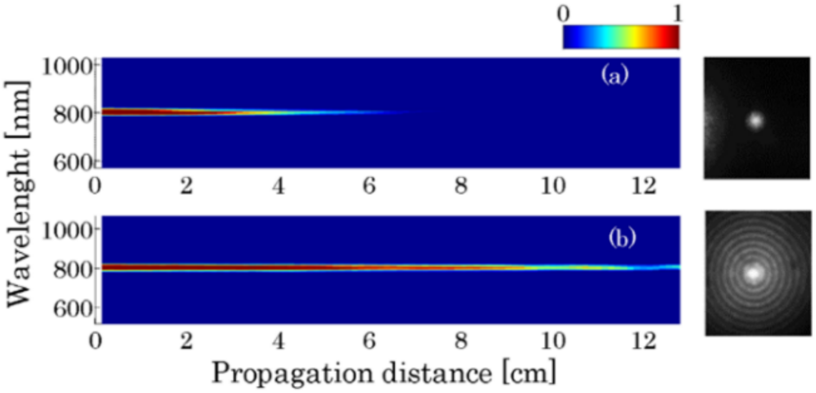

Figure 6.3 Spectral profiles of the (a) Gaussian beam and (b) Bessel-Gaussian beam measured over the central lobes as a function of the propagation distance. The corresponding experimentally created input beam modes are shown in the right panel.

When the initial power in the produced optical beam exceeds a critical value inside the optical medium, nonlinear optical self-focusing effects become important and initiate a catastrophic collapse of the beam, which is restrained by the plasma formation, inducing defocusing. The filamentation phenomena occur with the resulting dynamic balance of self-focusing and plasma defocusing. For this reason, the sufficient peak power of P_{in} =5.4

GW, which is much larger than the critical power for self-focusing in water, P_{cr} =3.6 MW, assured filament formation in water, as was observed previously [172,173]. Indeed, hot spots in the beam producing white light corresponding to multiple filament formation were directly observed in our experiments. When the regime of multifilamentation is reached, since each sub-filament dies out at a similar rate as the single filament, dissipative processes quickly deplete the filament. A well as any undesirable beam break-up into multiple filaments, much care was also taken to ensure that the produced beams had similar peak intensities, pulse durations, and beam diameters. The peak intensity and diameter were determined from the measurements with a power meter interchanged with a CCD camera; the measurements with the latter required additional neutral-density filters in front of it. We kept the distance between the SLM and the glass cell as short as possible to minimize the diffraction of the beams [78]. The beams were passed through a 13 cm-long glass cell, which was arranged vertically to allow us to measure the power and spectrum as a function of the propagation distance by changing the water level in the cell with a programmable infuse/withdraw syringe pump (Harvard PHD 2000). A mechanical iris was used to select the central portion of the beam. An optical flat was positioned after the cell to reflect a small portion of the beam into the integration cavity. Spectral measurements were taken as a function of the propagation distance by collecting the radiation in the cavity with an Ocean Optics USB-2000 spectrometer. Simultaneously, power measurements were obtained using a photodiode power meter head (Ophir PD300-IR) with a spectral range within 700-1800 nm. In order to measure the incident beam power after the water cell, a long-pass glass filter (RG-780) was placed in front of the power meter to filter out white-light (Figure 6.2). A LabVIEW code was used to control the infusing and withdrawing of water via a syringe pump, and to acquire the values from the power meter and the spectrum. Figure 6.3 shows spectra of the Gaussian Beam and Bessel-Gaussian Beam, which were obtained by measuring over the central lobe of the beams as a function of the propagation distance. The corresponding experimentally created beam modes are shown in the right panel of Figure 6.3.

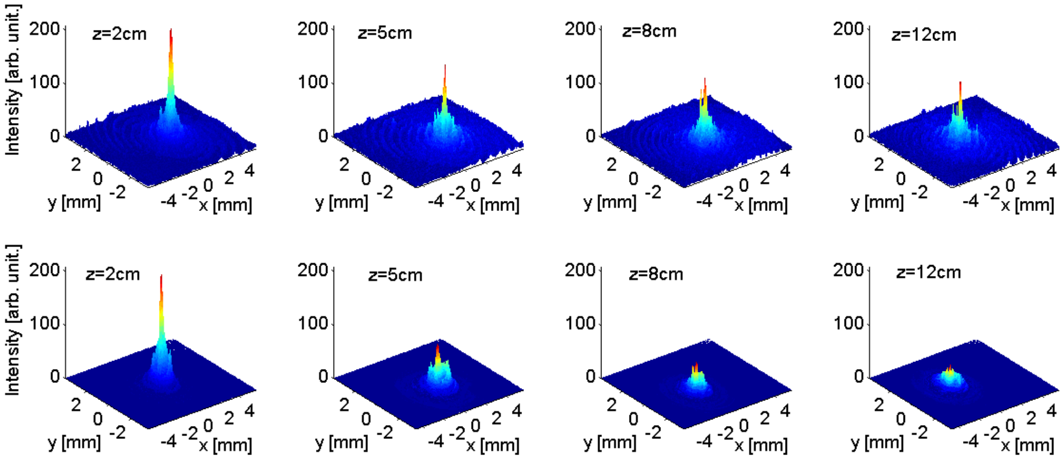

Figure 6.4 Measured IR distributions of the laser intensity in the (a) Bessel-Gaussian and (b) Gaussian beams at the different propagation distances.

The self-focusing effect took place near the entrance of the beam into the cell (self-focusing length of ~ 2cm), and the changes due to nonlinear effects in the spectral profiles of all two types of beams were observed during subsequent propagation. The spectrum for the incident Gaussian Beam mode has more depletion than the incident Bessel-Gaussian beam as the pulse propagates in the nonlinear medium.

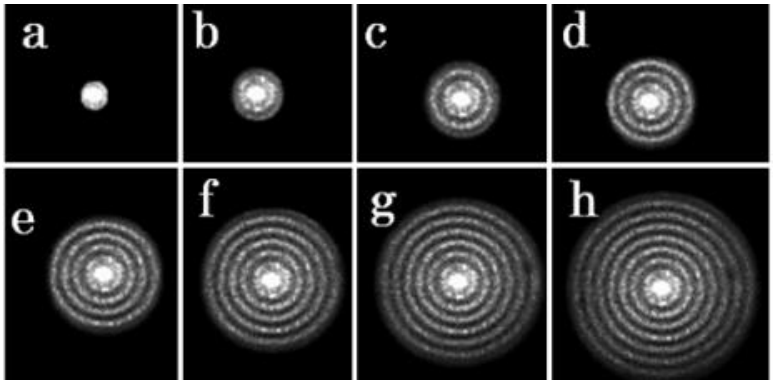

Figure 6.5 Experimentally created modes of the incident Bessel-Gaussian beam: (a) central peak of the beam with no lobes and (b-h) central peak with additional radial lobes.

As shown in Figure 6.4, the distributions of the laser intensity filtered out white-light with RG-780 filter were taken by a monochromatic CCD camera in the Gaussian and Bessel-Gaussian beams at different propagation distances. The profile of the incident Gaussian beam has more depletion than the incident Bessel-Gaussian beam as the pulse propagates in the nonlinear medium.

To better understand the propagation of a Bessel-Gaussian beam, we investigated their propagation dynamics by varying the number of radial lobes. Figure 6.5 depicts the experimentally created beams. The desired number of lobes of Bessel-Gaussian Beam was determined by using a radial holographic knife-edge realized with a computer generated hologram on SLM [63]. The power and spectrum were measured from only the central lobe of the resulting Bessel-Gaussian beam.

The central part of the beam had a diameter of 300μm and was similar to the FWHM of the Gaussian Beam. This portion of the beam was selected by the mechanical iris positioned after the water cell and in front of the power meter or the opening of the integration cavity. The spectra measured for Bessel-Gaussian beam as functions of propagation distance are shown in Figure 6.6. The effect of increasing number of radial lobes can be seen by an increase in the propagation distance of the central part of the beam. This increase is most noticeable when 1, 2 or 3 lobes are added.

In Figure 6.7, we show the infrared power measured for only the central peak of the Bessel-Gaussian beam with different number of radial lobes as a function of the propagation distance. With each additional radial lobe we observe the trend of an increasing power delivered to a given propagation distance within the range of distances 2-6 cm. At distances 6-8 cm the delivered power for beams with small number of lobes (1-2) decreases faster, while the beams with multiple lobes (>2) show similar power decay rate, but maintain a higher power, as compared to the beam with just a single central peak. For distances longer than 10cm the delivered power from the beams with 1 and 2 additional lobes (Figure 6.5(b, c)) is close to the power of the beam with no lobes (Figure 6.5(a)), while the power of the beams with multiple lobes (>3) preserves a level higher than that for the beam with no lobes.

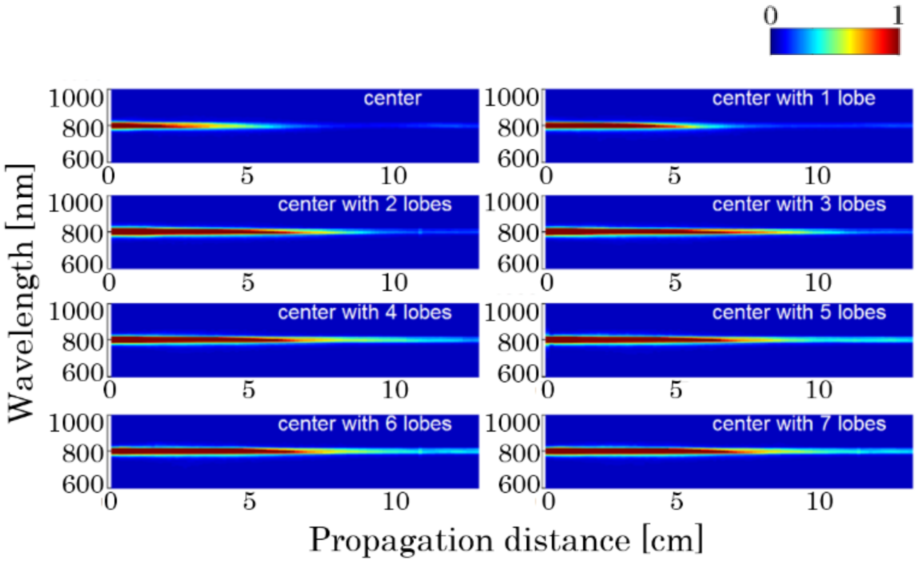

Figure 6.6 Spectra of the central lobe of the Bessel-Gaussian beams with different number of radial lobes and measured as a function of the propagation distance.

Since interaction between the central peak and secondary low-intensity ‘surrounding lobes’ beam starts with initial filament formation (self-focusing length of ~ 2cm) in the central peak, after initial filament formation, suitable addition of the surrounding lobes beam (with low intensity to produce a filament) serves to compensate dissipative effects. This results in a much longer extension of the filament.

The trend of propagation distance elongation was recently demonstrated experimentally by using dressed beams, where the central Gaussian beam is surrounded by auxiliary dressing beam, which is wider and has a lower intensity [169]. Since a Bessel-like beam, which has an annular structure, possesses an inward energy flux towards its optical axis [174], it is expected to be well suited to replenish the filament core, as is confirmed by our measurements. Also, when we compare our results with recent theoretical studies on filamentation of femtosecond beams with different transverse modes in Ar gas [167,168], we see a similar effect that the central core in Bessel-Gaussian beam mode is sustained for a longer propagation distance (compared to Gaussian beam). In addition, we have shown that increasing the outer part of the Bessel-Gaussian Beam helps to maintain the energy in the central peak, thus this outer part serves as an energy reservoir for the filaments formed in the central portion of the beam.

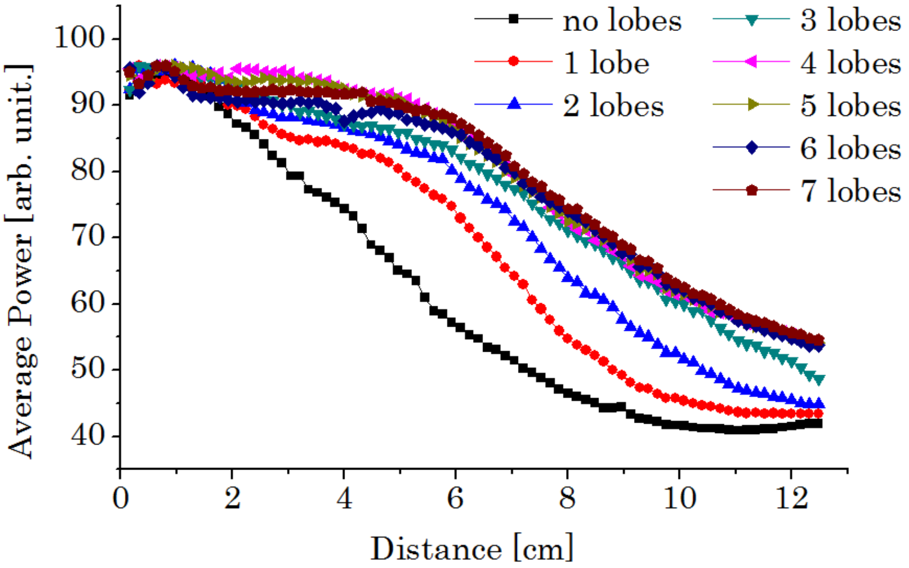

Figure 6.7 Average IR power measured for the central peak of the Bessel-Gaussian beam with the different number of radial lobes as a function of the propagation distance.

6.3 Conclusion

We experimentally investigated the propagation of intense femtosecond pulses in water for two different incident beam profile configurations. Between the two different transverse modes (Gaussian beam and Bessel-Gaussian beam), the length of propagation of Bessel-Gaussian beam for similar characteristics of the central part of the beam (peak intensity, pulse duration, and beam diameter) is considerably longer than for the other beam as determined by the measurements of the decay of the spectral and total power. A more detailed study of the Bessel-Gaussian beam with different number of the radial lobes indicates that the outer part of the Bessel-Gaussian beam, surrounded by a low-intensity reservoir of photons, serves as an energy reservoir that can suitably replenish the unavoidable dissipative losses of the filament core, so that the filaments formed at the inner part can persist for a long propagation distance with increasing number of radial lobes. One can in fact obtain a moderate improvement in the filament length by directly using a Bessel beam for filament generation. Our findings clearly indicate the high potential of Bessel-Gaussian Beam for various nonlinear optics applications involving the propagation of ultrafast pulses in a Kerr medium.

CHAPTER VII

TIME-SLICED 3D MOMENTUM IMAGING OF H_2^+ PHOTODISSOCIATION

For our long term goal of studying hydrogen molecular ion and its interaction with a white-light source in the ion beam apparatus, this chapter gives the results of reconstruction of the laser-induced photo-dissociation of H_2^+ with 800nm by employing a time-sliced 3D imaging technique.

7.1 Introduction

Both fast timing and simultaneous 2D position determination capabilities of new ion detector systems have generated new interest in understanding of many problems in molecular dynamics such as photoionization and photo-dissociation processes. In experimental study of dissociation processes, it is now possible to measure the 3D (three-dimensional) momentum vector with high resolution and efficiency for each charged fragment by combining large-diameter MCP (microchannel plate) detectors with delay-line anodes [57,58,175]. The performance of such detector systems has been further improved with the advent of anodes having three delay-line layers, better precision of the time digitizers, and advanced signal-reconstruction algorithms in especially coincidence measurements involving two or more charged fragments [59]. The detection resolution, efficiency, and reliability are increased with these improvements and a dead time is significantly decreased. Now, it is also possible to distinguish clearly between the signals producing from two charged fragments that hit the detector at the same position and time, as long as their spatial separation and the difference between their time of impact are more than some small directly measureable values [176].

For few years we have in our laboratory an ion beam apparatus that was obtained from Dr. Figger (Max-Planck-Institute of Quantum Optics). Together with others Dr. Figger has performed groundbreaking work with this apparatus ranging from spectroscopy on helium hydride [177] to strong-field dissociation of H_2^+ [178-184]. The apparatus can produce an intense beam of many kinds of molecular ions. We have measured current densities of more than 0.35 μA/mm^2 for H_2^+. We upgraded the ion beam apparatus with the detector that features position and time resolution.

Despite the unique information that can be gained by using H_2^+ targets, these studies are rare due to the additional complexity of using an ion beam as a target. Theoreticians commonly study these effects in H_2^+ due to its simplicity (see [185,186]), but experimentalists study instead the readily available H_2 (see [187,188]). Some H_2^+ studies have tailored the experimental conditions to enable the study of the transient H_2^+ formed early in the laser pulse (see [189,190]. However, much of the physics of H_2^+ in an intense laser fields is more easily understood starting from H_2^+ directly [191]. The dissociation of H_2^+ produced from H_2 in a laser pulse is not possible for lower intensities than that needed to first ionize the H_2 target, but H_2^+ can dissociate at much lower intensities. Therefore, dissociation of H_2^+ from an ion beam can be expected to differ from that of H_2^+ produced in the same laser pulse from H_2.

In this section of dissertation, we show preliminary results such as the photodissociation of H_2^+ with central wavelength 800nm, 50fs laser pulses by employing a time-sliced 3D imaging technique (a measurement of all three momentum components). We experimentally reconstruct the laser-induced photodissociation of H_2^+ molecular ions prepared by an electric discharge while neutral molecules are used as a target in the most experiment. We test our ion beam apparatus for its future applications.

7.2 Photodissociation of the hydrogen molecular ion

When the laser interacts with hydrogen molecular ion, a hydrogen atom and a proton are produced:

$$\mathrm{H}_2^+ + nh\nu \rightarrow \mathrm{H}+\mathrm{H}^+ \quad . \tag{7.1}$$

The laser pulses couple the attractive ground state $1s\sigma_g$ and the repulsive first excited state $2p\sigma_u$ with potential energy curves at the internuclear separation (Figure 7.1). The higher states energies is more than 11 eV which are much larger than the photon energy of 1.55 eV (800 nm), which was used in the experiment. Therefore they will not be considered here.

The difference between the photon energy $h\nu$ and the bounding energy of a particular vibrational level gives the kinetic energy of the fragments H and H^+:

$$E_{Diss}(\upsilon) = (nh\nu - |E_\upsilon|)/2 \tag{7.2}$$

Energies of vibrational levels are described as

$$E_{\upsilon} = \omega_e\left(\upsilon + \frac{1}{2}\right) - \omega_e x_e\left(\upsilon + \frac{1}{2}\right)^2 + \dots \tag{7.3}$$

where vibrational constants ω_e =2321.7 and $\omega_e x_e$ =66.2 for H_2^+ [192].

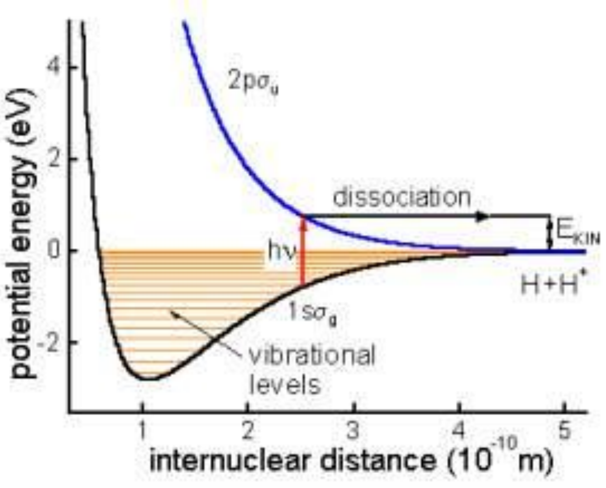

Figure 7.1 Potential energy curves of the two lowest states of hydrogen molecular ion in a weak field [178].

.

The coupling between the ground $1s\sigma_g$ and the first excited state $2p\sigma_u$ becomes very strong at intensities higher than 10^{12} W/cm^2. In this regime molecule-light system is usually described by potential curves "dressed" with photons or with so-called light-induced potential curves (Figure 7.2). Since the outer turning point almost coincides with the resonant internuclear separation of 2.54×10^{-10} m, the Franck-Condon factor for this transition is largest for the vibrational level $\upsilon = 9$. These curves are avoided crossing, so a gap opens up near the vibrational level which is resonant with the laser radiation (υ =9). The gap starts a process, normally forbidden, dissociation of molecular vibrational levels that lie below the resonant level. It is known as molecular bond-softening.

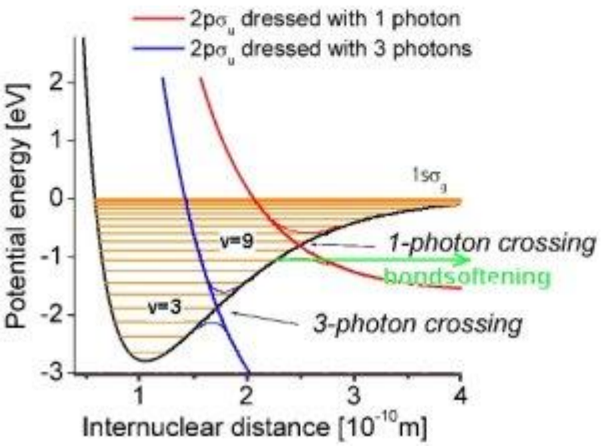

Figure 7.2 Potential energy curves of the photon dressed states. At I>10^{12} W/cm^2 the coupling between the ground 1sσ_g and the first excited state 2pσ_u becomes very strong [178].

At higher intensities three-photon absorption can take place and another gap opens. A molecule absorbs three photons but reemits one photon. Because the molecule absorbs more photons than needed for its dissociation, it is called ATD (above-threshold dissociation), [178].

7.3 Ion beam apparatus

As it is shown in Figure 7.3, our ion beam apparatus has three vacuum chambers and each chamber is pumped by a turbo molecular pump. The main components are an ion source, a magnet for mass selection, different size apertures to steer and collimate the ion beam, and faraday cups to measure the ion current.

In our experiment, a duoplasmatron ion source with a dc electric discharge was used to generate the molecular ions [193,194]. Neutral hydrogen gas is sent in the region between a hollow cathode and an anode. The emitted electrons from the hollow cathode are accelerated towards the anode by a potential difference of 450–600V. The intermediate electrode with respect to the anode is held at a potential of -100V, so it electrostatically focuses the electrons. In addition, we have a ferromagnetic intermediate electrode and a solenoid magnet (stabilized current typically in the range of 1 to 1.8 A) surrounding the ion source. The formed magnetic field constricts the plasma. The strength of the magnetic field increases towards the anode. When the electrons goes close to the anode, their radial velocity component increases while the axial component decreases. Hence, the electrons density is getting higher near the anode, so this increases the efficiency of neutral Hydrogen molecules ionization. A high potential difference between the anode and an extraction electrode extracts and accelerates molecular ions in the plasma. The whole ion source was held at a positive acceleration voltage 12 kV while the rest of the apparatus was grounded in order to extract the positive ions. The ions current is typically around 100 μA with an anode with an aperture of 150 μm. This extracted current could be optimized by adjusting of the solenoid magnet current surrounding the ion source.

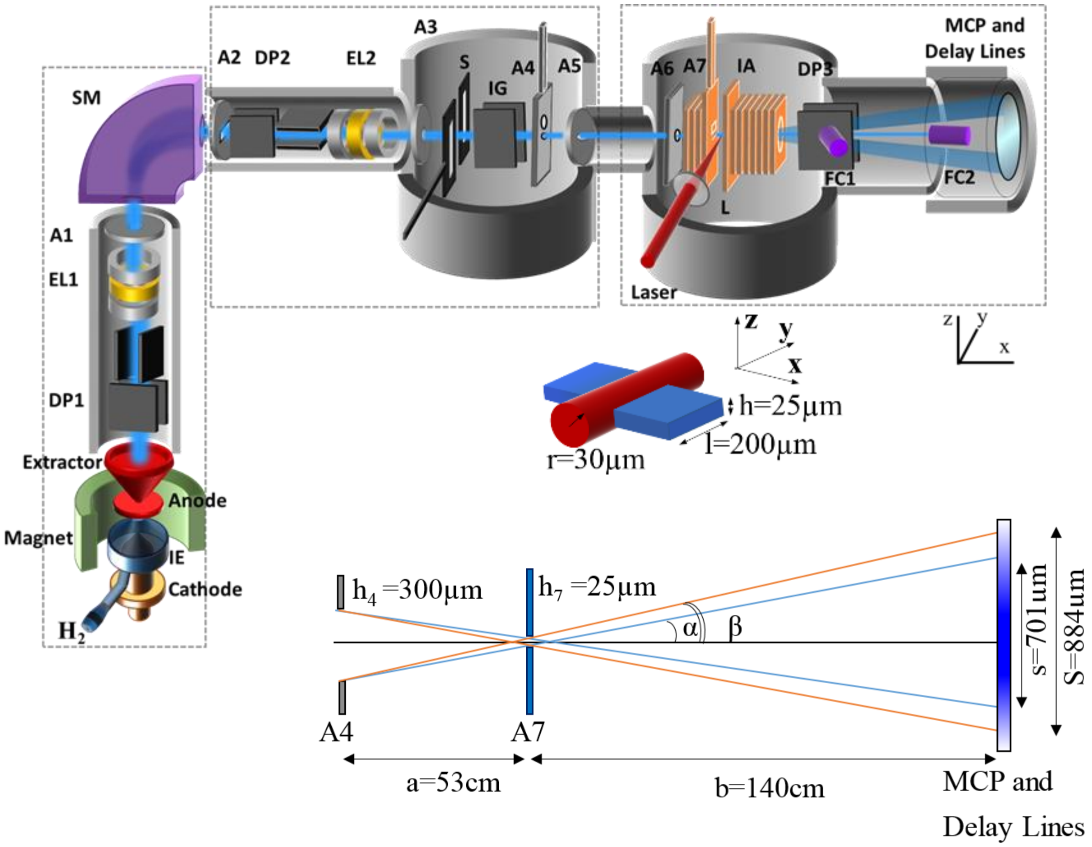

Figure 7.3 Layout of the ion beam apparatus. DP: deflection plates (13mm x 22.5mm x 0.85mm); EL: Einzel lenses; SM: sector magnet, R=150, B=10G, 8A, A: apertures; A3: 60mm circular plate with 2mm circular hole, A4: 60mm x 60mm square plate with 300µ circular hole, A5: 8mm circular hole, A6: 60mm x 60mm square plate with 3mm circular hole, A7: 25 x 200 slit and 1mm x 1mm square hole , IA, ion accelerator, S: vertical slit 0.75mm Gap, IG: Ion gate 92mm x 40mm high deflection plates with 5mm separation, L: focusing lens; FC: Faraday cup; MCP: microchannel plate detector. Inset (a) Interaction volume defined by the intersection of a laser beam (shown as a cylinder) and an ion beam (box). Inset (b) shows schematic diagram of the geometry employed for collimation along the x axis.

We used the horizontal and vertical electrostatic deflection plates (DP1) and an Einzel lens (EL1) in order to direct the extracted positive molecular ions into a sector magnet (SM) through entrance slit A1 (width of 5 mm). Then by adjusting the magnetic field of the sector magnet, we deflected the H_2^+ molecular ions by 90◦ to pass through exit slit A2 (width of 5 mm). A second set of electrostatic deflection plates (DP2) is used to steer the selected ion beam. Then it enters Einzel lens EL2. In combination with Einzel lens EL1, EL2 is used as an electrostatic telescope to collimate the ion beam and maximize the ion beam current.

To achieve the alignment of the ion beam, the ion current is measured at different points along the beam path. There are two collimating apertures A4 (300 μm circular aperture) and A7 (a 300×25μm aperture), and auxiliary pre-apertures A3 and A6 with diameters of 2 mm and 1 mm, respectively, were placed in front of each collimating apertures to make the alignment easier. All insulated apertures and Faraday cups FC1 and FC2 were connected to an electrometer (Keithley Instruments, model 617).

First, we found a right combination of voltages on the deflection plates, Einzel lenses and sector magnet by optimizing the ion current on aperture A4 and its pre-aperture. After that, we followed the same procedure for aperture A7 and its pre-aperture. Finally, we maximized the current on Faraday cup FC2. We repeated the all procedure several times with similar initial settings to achieve a sufficient ion current.

The experimental resolution depends on the width and divergence of the ion beam. They are calculated by the sizes of the collimating apertures along the laser polarization axis (z axis) and the positions of the apertures and detector on the ion beam axis. The collimation geometry in the x-z plane is shown in inset of Figure 7.3. The outer lines pair shows a maximum allowed divergence of the beam, the inner lines illustrates an optimally collimated ion beam. The widths on the detector are indicated by letters s and S. The divergence angles and widths of the ion beam can be easily calculated as angles of α=0.25 mrad and β=0.30 mrad and widths of s=701 μm, S=884 μm from similarity of the triangles. By using a 300 μm circular aperture A4 and a 300 μm ×25 μm aperture size A7 for collimation the ion beam, we could optimize the current of a 12keV H_2^+ beam measured on Faraday cup FC2 up to 3–4 nA.

The collimated H_2^+ beam was crossed by the focused laser beam at a right angle. The focal position of femtosecond laser beam is adjusted by the position of the laser breakdown in air. Overlap of the laser and ion beam is optimized by using a vertically adjustable 50 μm pinhole placed under 45◦ with respect to the both beams. Therefore, we easily crossed the laser beam and the ion beam that passes through apertures A4 and A7.

In order to reduce the intensity volume effect, we setup the focus diameter of the laser pulses greater than the height of the rectangular molecular ion beam (25 µm). Rayleigh lengths were large compared to the width of the molecular beam (300 µm) (see the inset of Figure 7.3). The number of molecular ions can be roughly estimated to ~40 for a typical current of about 80 nA in the interaction region, a laser beam diameter of 60µm and a molecular ions velocity of $1.5\times10^{6}\,\mathrm{m/s}$. The distance between the interaction point and the detector is 1400 mm.

All TOF information is measured relative to the start signal from a photodiode that is triggered by the laser pulse. The dissociated fragments of H_2^+ were detected in coincidence by an 80 mm diameter microchannel plate (MCP) detector. In addition, coincidence with the laser pulse registered by a photo-diode detector was required for the true events by using the coincidence time of flight (TOF) technique. The MCP detector signals provide position (using a three-layer hexagonal design delay-line anode) and time of arrival information for each fragment, thus allowing the evaluation of the velocity of both fragments.

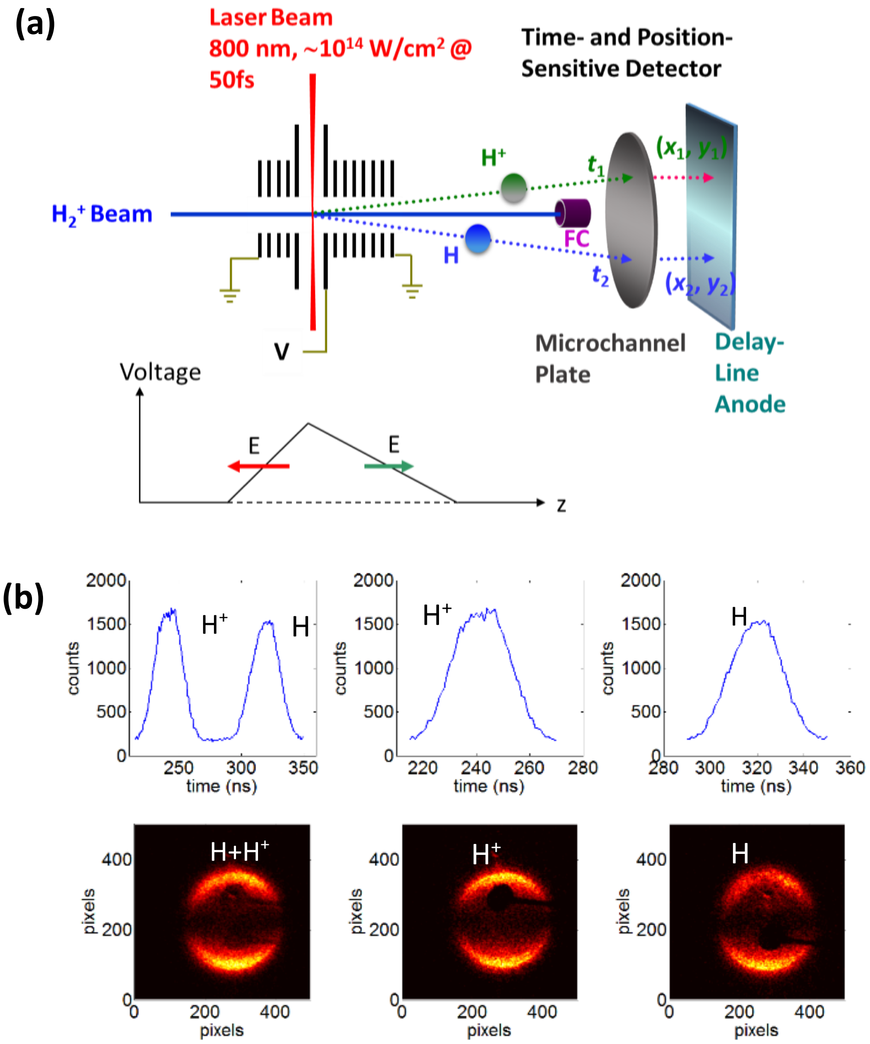

Figure 7.4 (a) Schematic view of the spectrometer, (b) after applying ion accelerator voltage +750V for Δt=60ns separation, TOF spectrums of the neutral and charged fragments resulting from the photodissociation of H_2^+ (upper graphs), related accumulated frames of the fragments for TOF between 220ns-340ns, 220-280 ns and 280-340ns (lower graphs). 1pixel=25μm.

7.4 Result and discussion

The laser field is linearly polarized along the direction perpendicular to the ion beam. Upon dissociation the two fragments, namely hydrogen atom and proton, obtain a relative momentum and so spatially separation. We applied a weak longitudinal electric field (typically 20–30 V/mm) along the ion-beam direction to accelerate the ionic fragments in the spectrometer (a schematic view of the spectrometer is shown in Figure 7.4(a)) in order to clearly distinguish the charged and neutral fragments from each other. To separate the fragments, we applied ion accelerator voltage +750V. The results in two distinct peaks in the Time-of-Flight spectrums for the neutral and charged fragments resulting from the H_2^+ photo-dissociation are shown in the upper graphs of Figure 7.4(b), and their accumulated frames in TOF intervals between 220 ns-340 ns, 220-280 ns and 280-340 ns are given in the lower graphs of Figure 7.4(b).

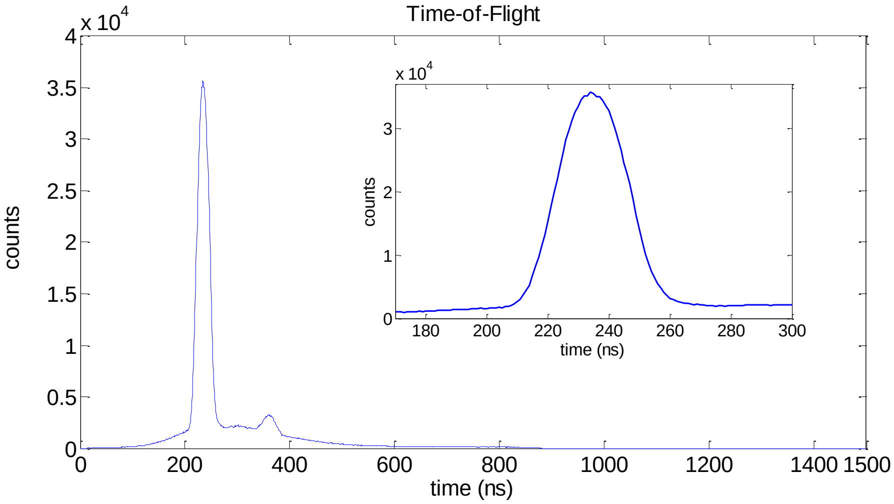

Figure 7.5 Time-of-flight spectrum of fragments from H_2^+ photo-dissociation. No voltage was applied to the electrostatic spectrometer.

In order to reconstruct experimentally the laser-induced photo-fragmentation of H_2^+, we applied no voltage to the electrostatic spectrometer for detection of both charged and neutral fragments. Time-of-flight spectrum of photo-dissociation of H_2^+ at 800 nm is recorded (Figure 7.5). Figure 7.6 displays a series of slices through the H_2^+ fragments velocity sphere after photo-dissociation of H_2^+ at 800 nm. The numbers in the bottom of the images indicate the time-of-flight time intervals used to generate the images. Time intervals of 230–240 ns correspond to the center of the distribution (maximum of the symmetric curve in Figure 7.5). This center slice (230 ns-240 ns) of the TOF distribution in the inset of Figure 7.6 is clearly sharper than the momentum distribution of the full data set (197 ns-274 ns), which allows to resolve the peaks corresponding to different vibrational states of H_2^+.

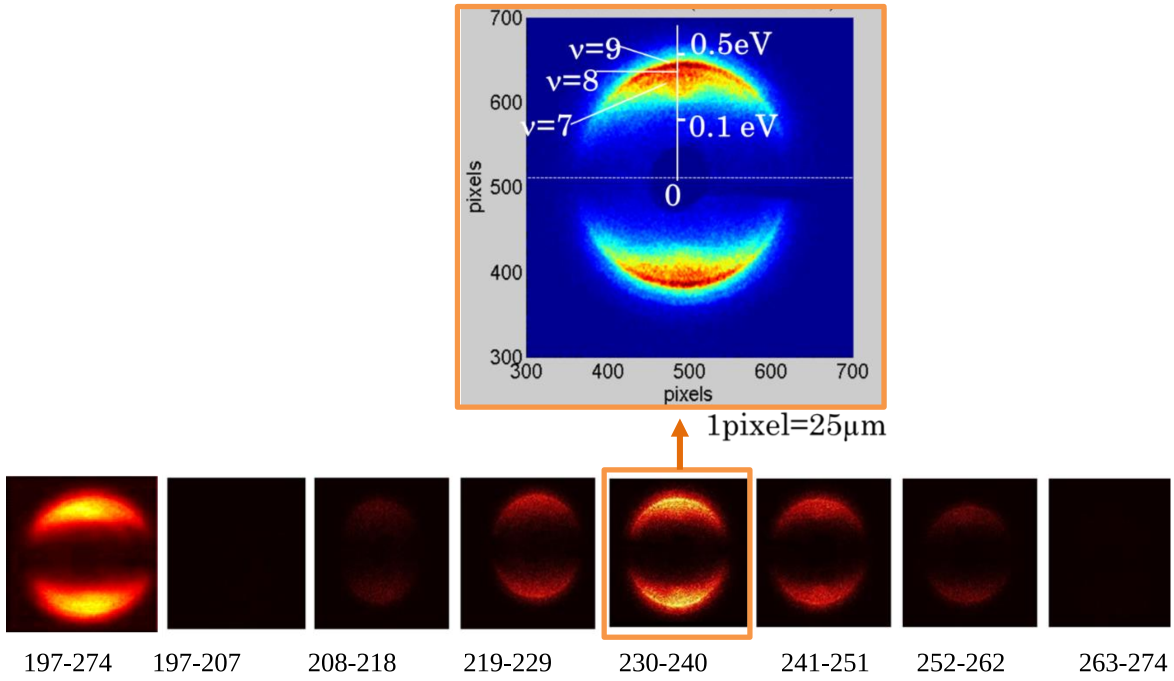

Figure 7.6 Series of time slices (10 ns intervals between 197 ns and 274 ns) through the H_2^+ momentum distribution. The momentum distribution of the center slice (230 ns–240 ns) is clearly sharper than the momentum distribution of the full data set (197 ns-274 ns).

7.5 Conclusion

Using the ion beam apparatus with the upgraded detector now features position and time resolution, we obtained results for the fragmentation of H_2^+ with 800 nm, 50 fs laser pulses by employing a time-sliced 3D imaging (a measurement of all three momentum components). According to the results of the photo-dissociation of H_2^+ with 800 nm, 50 fs laser pulses by employing a time-sliced 3D imaging technique, a series of slices through the H_2^+ momentum sphere after photodissociation indicates that the center slice of the TOF distribution is clearly sharper than the momentum distribution of the full data set, which allows to resolve the peaks corresponding to different vibrational states of H_2^+. Consequently, the developed detection system is well-suited for 3D imaging of the fragment momentum distribution and is a promising tool for imaging studies of photo fragmentation of atomic and molecular systems.

CHAPTER VIII

OVERALL CONCLUSIONS

In this dissertation, a laser beam analysis method based on a holographic knife-edge was applied to a holographically created paraxial beam. Good agreement is found with experimental results of the measured power from both holographic and mechanical knife-edge methods. A high fidelity Hermite-Gaussian and Laguerre-Gaussian modes were produced by using the same method to that used to holographically knife-edge (phase-amplitude encoding). In order to analyze these modes, theoretical knife-edge equations were derived to fit to the measured data. From the derived equations we were able to determine beam characteristics such as the waist and the distribution of intensities between the modal lobes. All measured data showed good agreement with the theoretically predicted curves. In principle, the outlined method can be used to create virtually any desired shape for the characterization of optical beams. We used this method to tomographically reconstruct, in situ, a broadband optical beam in a folded-2f setup.

White-light generation using spatially- structured beams of femtosecond radiation were studied. We showed that $HG_{0,1}$, $HG_{1,0}$, $HG_{1,1}$, and higher modes can be produced by using a 1D spatial light modulator. Such beams exhibit phase discontinuities and steeper intensity gradients and were produced by imposing spatial phase masks on the initial Gaussian beam. The laser intensity distributions were theoretically described and found to be in good agreement with experiment. When the spatial phase of an initial Gaussian beam (showing no significant white-light generation) was changed to that of a $HG_{0,1}$, or $HG_{1,1}$ mode, significant amounts of white-light were produced and controlled.

The two-beam interaction on white-light generation is studied in details. We saw the effect of enhancement of the white light generation due to interaction of the beams. It is observed that at zero delay the white light level goes to the level that is equal or sometimes below the level found for large delays when pulses do not overlap. The enhancement of the white light generation happens in the beam that is lagging, since the first beam introduces changes in the medium, which then affect the following second pulse. For the positive dispersion, which is usual for glass, the leading part of pulses is of lower frequency. Then the results are found consistent with transmission of energy from higher frequency part of one beam to the lower frequency part of the other beam. It is emphasized that the reduction of the power of each of the IR beams near zero delay can be related to the mutual refraction and diffraction, so the white light generation was suppressed near zero delay.

In the study of filament propagation length of femtosecond pulses with holographically created different transverse modes, we found that the length of propagation of Bessel-Gaussian beam for similar characteristics is considerably longer than for the other beams. The study with Bessel-Gaussian beams having different number of the radial lobes indicates that the outer part of the Bessel-Gaussian beam serves as an energy reservoir, so that the filaments formed at the inner part can persist for a long propagation distance with increasing number of radial lobes.

In the last part of the dissertation, we described the ion beam apparatus, which was upgraded with the detector, featuring position and time resolution. We show results of the fragmentation of H_2^+ with 800 nm, 50 fs laser pulses by employing a time-sliced 3D imaging as a first stage of the long term future study on the coherent control and manipulation of the interaction of femtosecond radiation with molecular systems.

REFERENCES

[1] M. Nisoli, G. Sansone, S. Stagira, S.D. Silvestri, C. Vozzi, M. Pascolini, L. Poletto, P. Villoresi, and G. Tondello, Phys. Rev. Lett. 91 (2003) 213905.

[2] I.J. Kim, C.M. Kim, H.T. Kim, G.H. Lee, Y.S. Lee, J.Y. Park, D.J. Cho, and C.H. Nam, Phys. Rev. Lett. 94 (2005) 243901.

[3] P.P. Corso, E. Fiordilino, and F. Persico, J. Phys. B: At. Mol. Opt. Phys. 40 (2007) 1383.

[4] E. Gagnon, P. Ranitovic, X.M. Tong, C.L. Cocke, M.M. Murnane, H.C. Kapteyn, and A.S. Sandhu, Science 317 (2007) 1374.

[5] A.D. Bandrauk, S. Barmaki, and G.L. Kamta, Phys. Rev. Lett. 98 (2007) 013001

[6] P.M. Paul, E.S. Toma, P. Breger, G. Mullot, F. Augé, P. Balcou, H.G. Muller, P. Agostini, Science 292 (2001) 1689.

[7] M. Hentschel, R. Keinberger, C. Spielmann, G.A. Reider, N. Milosevic, T. Brabec, P. Corkum, U. Heinzmann, M. Dresher, and F. Krausz, Nature 414 (2001) 509.

[8] R. Keinberger, E. Gouliemakis, M. Uiberacker, A. Baltuska, V. Yakovlev, F. Bammwe, A. Scrinzi, T. Westerwalbesloh, U. Kleinebeg, U. Heinzmann, M. Drescher, and F. Krausz, Nature 427 (2004) 817.

[9] P.B. Corkum and F. Krausz, Nat. Phys. 3 (2007) 381.

[10] P. Agostini, F. Fabre, G. Mainfray, G. Petite, N. K. Rahman, Phys. Rev. Lett. 42 (1979) 1127.

[11] R.R. Freeman, P.H. Bucksbaum, H. Milchberg, S. Darack, D. Schumacher, and M.E. Geusic, Phys. Rev. Lett. 59 (1987) 1092.

[12] P.B. Corkum, Phys. Rev. Lett. 71 (1993) 1994.

[13] N.A. Hart, J. Strohaber, G. Kaya, N. Kaya, A.A. Kolomenskii, and H.A. Schuessler, Phys. Rev. A 89 (2014) 053414.

[14] R.R. Alfano and S.L. Shapiro, Phys. Rev. Lett. 24 (1970) 584.

[15] R.R. Alfano, The Supercontinuum Laser Source: Fundamentals with Updated References, 2nd edition, Springer Science+Business Media, Inc., New York, 2006.

[16] N. Bloembergen, Opt. Commun. 8 (1973) 285.

[17] W.L. Smith, P. Liu, and N. Bloembergen, Phys. Rev. A 15 (1977) 2396.

[18] R.L. Fork, C.V. Shank, C. Hirlimann, R. Yen, and W.J. Tomlinson, Opt. Lett. 8 (1983) 1.

[19] G. Yang and Y.R. Shen, Opt. Lett. 9 (1984) 510.

[20] P.B. Corkum, C. Rolland, and T. Srinivasan-Rao, Phys. Rev. Lett. 57 (1986) 2268.

[21] P.B. Corkum and C. Rolland, IEEE J. Quantum Electron. 25 (1989) 2634.

[22] F.A. Ilkov, L.S. Ilkova, and S.L. Chin, Opt. Lett. 18 (1993) 681.

[23] V. François, F.A. Ilkov, and S.L. Chin, Opt. Commun. 99 (1993) 241.

[24] A. Brodeur, F.A. Ilkov, and S.L. Chin, Opt. Commun. 129 (1996) 193.

[25] G.S. He, G.C. Xu, Y. Cui, and P.N. Prasad, Appl. Opt. 32 (1993) 4507.

[26] S.L. Chin, S.A. Hosseini, W. Liu, Q. Luo, F. Theberge, N. Aközbek, A. Becker, V.P. Kandidov, O.G. Kosareva, and H. Schroeder, Can. J. Phys. 83 (2005) 863.

[27] A. Couairon, and A. Mysyrowicz, Phys. Rep. 44 (2007) 47.

[28] A. Braun, G. Korn, X. Liu, D. Du, J. Squier, and G. Mourou, Opt. Lett. 20 (1995) 73.

[29] L. Bergé, S. Skupin, R. Nuter, J. Kasparian, and J. P. Wolf, Rep. Prog. Phys. 70 (2007) 1633.

[30] J. Kasparian and J.P. Wolf, Opt. Express 16 (2008) 466.

[31] V.P. Kandidov, S.A. Shlenov, and O.G. Kosareva, Quantum Electron. 39 (2009) 205.

[32] S.L. Chin, Femtosecond Laser Filamentation, Springer, New York, 2010.

[33] R.W. Boyd, S.G. Lukishova, Y.R. Shen, Self-focusing: Past and Present: Fundamentals and Prospects, Springer, New York, 2009.

[34] S.L. Chin, T.J. Wang, C. Marceau, J. Wu, J.S. Liu, O. Kosareva, N. Panov, Y.P. Chen, J.F. Daigle, S. Yuan, A. Azarm, W.W. Liu, T. Seideman, H.P. Zeng, M. Richardson, R. Li, and Z.Z. Xu, Laser Phys. 1–53 (2012) 22.

[35] L. Bergé, S. Skupin, C. Köhler, I. Babushkin, and J. Herrmann, Phys. Rev. Lett. 110 (2013) 073901.

[36] K.C. Kulander, F.H. Mies, and K.J. Schafer, Phys. Rev. A 53 (1996) 2562.

[37] J.T. Lin and T.F. Jiang, Phys. Rev. A 63 (2000) 013408.

[38] J. McKenna, A.M. Sayler, F. Anis, B. Gaire, N.G. Johnson, E. Parke, J.J. Hua, H. Mashiko, C.M. Nakamura, E. Moon, Z. Chang, K.D. Carnes, B.D. Esry, and I. Ben-Itzhak, Phys. Rev. Lett. 100 (2008) 133001.

[39] J. Ludwig, H. Rottke, and W. Sandner, Phys. Rev. A 56 (1997) 2168

[40] A. Giusti-Suzor, F.H. Mies, L.F. DiMauro, E. Charron, and B. Yang, J. Phys. B: At. Mol. Opt. Phys. 28 (1995) 309

[41] K. Vijayalakshmi, A. Talebpour, T.T. Nguyen-Dang, J. Yang, A.D. Bandrauk, and S.L. Chin, Phys. Rev. A 62 (2000) 053408

[42] J.H. Posthumus, Rep. Prog. Phys. 67 (2004) 623.

[43] A.D. Bandrauk and H.Z. Lu, Phys. Rev. A 73 (2006) 013412.

[44] A. Rudenko, B. Feuerstein, K. Zrost, V.L.B. de Jesus, T. Ergler, C. Dimopoulou, C.D. Schröter, R. Moshammer, and J. Ullrich, J. Phys. B: At. Mol. Opt. Phys. 38 (2005) 487.

[45] M.Y. Shverdin, D.R. Walker, D.D. Yavuz, G.Y. Yin, and S.E. Harris, Phys. Rev. Lett. 94 (2005) 033904.

[46] A. Gürtler, F. Robicheaux, W.J.v.d. Zande, and L.D. Noordam, Phys. Rev. Lett. 92 (2004) 033002.

[47] G.G. Paulus, F. Grasbon, H. Walther, P. Villoresi, M. Nisoli, S. Stagira, E. Priori, and S.D. Silvestri, Nature 414 (2001) 182.

[48] V. Roudnev and B.D. Esry, Phys. Rev. Lett. 99 (2007) 220406

[49] M.F. Kling, C. Siedschlag, A.J. Verhoef, J.I. Khan, M. Schultze, T. Uphues, Y. Ni, M. Uiberacker, M. Drescher, F. Krausz and M.J.J. Vrakking, Science 312 (2006) 246.

[50] T. Rathje, A.M. Sayler, S. Zeng, P. Wustelt, H. Figger, B.D. Esry, and G.G. Paulus, Phys. Rev. Lett. 111 (2013) 093002.

[51] J. Bethge, C. Bree, H. Redlin, G. Stibenz, P. Staudt, G. Steinmeyer, A. Demircan, and S. Duesterer, J. Opt. 13 (2011) 055203.

[52] L. Berge, S. Skupin, and G. Steinmeyer, Phys. Rev. Lett. 101 (2008) 213901.

[53] Q. Luo, H.L. Xu, S.A. Hosseini, J.F. Daigle, F. Théberge, M. Sharifi, and S.L. Chin, Appl. Phys. B 82 (2006) 105.

[54] C.P. Hauri, W. Kornelis, F.W. Helbing, A. Heinrich, A. Couairon, A. Mysyrowicz, J. Biegert, and U. Keller, Appl. Phys. B 79 (2004) 673.

[55] J. Kasparian, R. Ackermann, Y.-B. André, G. Méchain, G. Méjean, B. Prade, P. Rohwetter, E. Salmon, K. Stelmaszczyk, J. Yu, A. Mysyrowicz, R. Sauerbrey, L. Woeste, and J.P. Wolf, Optics Express 16 (2008) 5757.

[56] C. D'Amico, A. Houard, M. Franco, B. Prade, A. Mysyrowicz, A. Couairon, V.T. Tikhonchuk, Phys. Rev. Lett. 98 (2007) 235002.

[57] J. Ullrich, R. Moshammer, A. Dorn, R. Dörner, L.P.H. Schmidt, and H. Schmidt-Böcking, Rep. Prog. Phys. 66 (2003) 1463.

[58] R. Dörner, V. Mergel, O. Jagutzki, L. Spielberger, J. Ullrich, R. Moshammer, and H. Schmidt-Böcking, Phys. Rep. 330 (2000) 95.

[59] Roentdek delay line detector with hexanode, www.roentdek.com/ . Accessed 11-05-13.

[60] J.C. Diels and W. Rudolph, Ultrashort laser pulse phenomena, Academic press, Burlington, 2006.

[61] R. Trebino, K.W. DeLong, D.N. Fittinghoff, J.N. Sweetser, M.A. Krumbügel, B.A. Richman, and D.J. Kane, Rev. Sci. Instrum. 68 (1997) 3277.

[62] A simplified FROG device, GRENOUILLE, www.swampoptics.com/tutorials_GRENOUILLE.htm. Accessed 06-17-14.

[63] J. Strohaber, G. Kaya, N. Kaya, N. Hart, A.A. Kolomenskii, G.G. Paulus, and H.A. Schuessler, Opt. Express 19 (2011) 14321.

[64] M. Babiker, W.L. Power, and L. Allen, Phys. Rev. Lett. 73 (1994) 1239.

[65] A. Picón, J. Mompart, J.R. Vázquez de Aldana, L. Plaja, G.F. Calvo, and L. Roso, Opt. Express 18 (2010) 3660.

[66] A. Alexandrescu, D. Cojoc, and E.D. Fabrizio, Phys. Rev. Lett. 96 (2006) 243001.

[67] E. Serabyn, D. Mawet, and R. Burruss, Nature 464 (2010) 1018.

[68] J.H. Lee, G. Foo, E.G. Johnson, and G.A. Swartzlander, Phys. Rev. Lett. 97 (2006) 053901.

[69] J.-Y. Vinet, Phys. Rev. D 82 (2010) 042003.

[70] L.T. Vuong, T.D. Grow, A. Ishaaya, A.L. Gaeta, G.W. ’t Hooft, E.R. Eliel, and G. Fibich, Phys. Rev. Lett. 96 (2006) 133901.

[71] J. Ng, Z. Lin, and C.T. Chan, Phys. Rev. Lett. 104 (2010) 103601.

[72] M.A. Bandres and J. Gutiérrez-Vega, Opt. Letters 29 (2004) 144.

[73] J. Strohaber, C. Petersen, and C.J.G.J. Uiterwaal, Optics Letters 32 (2007) 2387.

[74] J. Leach, M.R. Dennis, J. Courtial, and M.J. Padgett, Nature 432 (2004) 165.

[75] K. Bezuhanov, A. Dreischuh, G.G. Paulus, M.G. Schätzel, and H. Walther, Opt. Lett. 29 (2004) 1942.

[76] I. Mariyenko, J. Strohaber, C. Uiterwaal, Opt. Express 13 (2005) 7599.

[77] I. Zeylikovich, H.I. Sztul, V. Kartazaev, T. Le, and R.R. Alfano, Opt. Lett. 32 (2007) 2025.

[78] J. Strohaber, T.D. Scarborough, and C.J.G.J. Uiterwaal, Appl. Opt. 46 (2007) 8583.

[79] The Nobel Prize in Physics 1971 for invention and development of the holographic method, www.nobelprize.org/nobel_prizes/physics/laureates/1971/. Accessed 03-01-10.

[80] J.W. Goodman, and R.S.C. Gustafson, Opt. Eng. 35 (1996) 1513.

[81] J. Strohaber, PhD, University of Nebraska, Lincoln, 2008.

[82] LCOS-SLM (Optical Phase Modulator) X10468-01, www.hamamatsu.com/us/en/product/alpha/P/4015/X10468-02/index.html. Accessed on 08-21-12.

[83] J.A. Davis, D.M. Cottrell, J. Campos, M.J. Yzuel, and I. Moreno, Appl. Opt. 38 (1999) 5004.

[84] J.B. Bentley, J.A. Davis, M.A. Bandres, and J.C. Gutiérrez-Vega, Opt. Lett. 31 (2006) 649.

[85] J.F. James, A Student's Guide to Fourier Transforms: With Applications in Physics and Engineering, Cambridge University Press, New York, 2011.

[86] J.M. Khosrofian and B.A. Garetz, Appl. Opt. 22 (1983) 3406.

[87] O. Mendoza-Yero and M. Arronte, J. Phys.: Conf. Ser. 59 (2007) 497.

[88] J. Soto, M. Rendón, and M. Martín, Appl. Opt. 36 (1997) 7450.

[89] S. Quabis, R. Dorn, M. Eberler, O. Glöckl, and G. Leuchs, Appl. Phys. B 72 (2001) 109.

[90] N. Kaya, J. Strohaber, A.A. Kolomenskii, G. Kaya, H. Schroeder, and H.A. Schuessler, Opt. Express 20 (2012) 13337.

[91] J.H. Glownia, J. Misewich, and P.P. Sorokin, J. Opt. Soc. Am. B 3 (1986) 1573.

[92] S. Cussat-Blanc, A. Ivanov, D. Lupinski, and E. Freysz, Appl. Phys. B 70 (2000).

[93] T. Kobayashi and A. Shirakawa, App. Phys. B 70 (2000) S239.

[94] T. Kobayashi, T. Saito, and H. Ohtani, Nature 414 (2001) 531.

[95] P.-L. Hsiung, Y. Chen, T.H. Ko, J.G. Fujimoto, C.J.S.d. Matos, S.V. Popov, J.R. Taylor, and V.P. Gapontsev, Opt. Express 12 (2004) 5287

[96] E. Hugonnot, M. Somekh, D. Villate, F. Salin, and E. Freysz, Opt. Express 12 (2004) 2397

[97] K.R. Wilson and V.V. Yakovlev, J. Opt. Soc. Am. B 14 (1997) 444.

[98] E.N. Glezer, Y. Siegal, L. Huang, and E. Mazur, Phys. Rev. B 51 (1995) 6959.

[99] M. Wittmann and A. Penzkofer, Opt. Commun. 126 (1996) 308.

[100] J. Ranka, R.W. Schirmer, and A. Gaeta, Phys. Rev. Lett. 77 (1996) 3783.

[101] A. Brodeur and S.L. Chin, Phys. Rev. Lett. 80 (1998) 4406.

[102] A. Brodeur and S.L. Chin, J. Opt. Soc. Am. B 16 (1999) 637.

[103] A. Couairon and A. Mysyrowicz, Phys. Rep. 441 (2007) 47.

[104] J.H. Marburger, Prog. Quant. Electron. 4 (1975) 35.

[105] A. Dharmadhikari, F. Rajgara, D. Mathur, H. Schroeder, and J. Liu, Opt. Express 13 (2005) 8555.

[106] H. Schroeder, J. Liu, and S. Chin, Opt. Express 12 (2004) 4768.

[107] M.P. Poudel, 3384310 Ph.D., Texas A&M University, Ann Arbor, 2009.

[108] L. Allen, M.W. Beijersbergen, R.J.C. Spreeuw, and J.P. Woerdman, Phys. Rev. A 45 (1992) 8185.

[109] A.E. Siegman, Lasers, University Science Books, Sausalito CA, 1986.

[110] J. Peatross, M. Ware, Physics of Light and Optics, Brigham Young University Textbook, Provo UT, 2011 edition, available at optics.byu.edu.

[111] K. Cook, R. McGeorge, A.K. Kar, M.R. Taghizadeh, and R.A. Lamb, Appl. Phys. Lett. 86 (2005) 021105.

[112] Y. Silberberg and I. Bar-Joseph, Phys. Rev. Lett. 48 (1982) 1541.

[113] Y. Silberberg and I. Bar-Joseph, J. Opt. Soc. Am. B 1 (1982) 662.

[114] R. Righini, Science 262 (1993) 1386.

[115] J.E. Aber, M.C. Newstein, and B.A. Garetz, J. Opt. Soc. Am. B 17 (2000) 120.

[116] J.M. Harbold, F.Ö. Ilday, F.W. Wise, B.G. Aitken, IEEE Photon. Technol. Lett. 14 (2002) 822.

[117] G. Lenz, J. Zimmermann, T. Katsufuji, M.E. Lines, H.Y. Hwang, S. Spalter, R.E. Slusher, S.W. Cheong, S. Sanghera, and I.D. Aggarwal, Opt. Lett. 25 (2000) 254.

[118] M. Asobe, T.Kanamori, and K. Kubodera, IEEE Photon. Technol. Lett. 4 (1992) 362.

[119] V.K. Tikhomirov and S.R. Elliott, J. Phys.: Condens. Matter 7 (1995) 1737.

[120] M.A. Duguay and A.T. Mattick, Appl. Opt. 10 (1971) 2162.

[121] C.V. Shank, Science 233 (1986) 1276.

[122] R. Nakamura and Y. Kanematsu, Rev. Sci. Instrum. 75 (2005) 636.

[123] R.Y. Chiao, E. Garmire, and C.H. Townes, Phys. Rev. Lett. 13 (1964) 479.

[124] Y.R. Shen, Prog. Quantum Electron. 4 (1975) 1.

[125] F. Shimizu, Phys. Rev. Lett. 19 (1967) 1097.

[126] F. DeMartini, C.H. Townes, T.K. Gustafson, and P.L. Kelley, Phys. Rev. 164 (1967) 312.

[127] R.R. Alfano and S.L. Shapiro, Phys. Rev. Lett. 24 (1970) 592.

[128] J. Reintjes, R.L. Carman, and F. Shimizu, Phys. Rev. A 8, 1486 8 (1973) 1486.

[129] T.D. Grow, A.A. Ishaaya, L.T. Vuong, A.L. Gaeta, N. Gavish, and G. Fibich, Opt. Express 14 (2006) 5468.

[130] L. Bergé, S. Skupin, F. Lederer, G. Méjean, J. Yu, J. Kasparian, E. Salmon, J.P. Wolf, M. Rodriguez, L. Wöste, R. Bourayou, and R. Sauerbrey, Phys. Rev. Lett. 92 (2004) 225002.

[131] S.L. Chin, F. Théberge, and W. Liu, Appl. Phys. B 86 (2007) 477.

[132] A. Brodeur, C.Y. Chien, F.A. Ilkov, S.L. Chin, O.G. Kosareva, and V.P. Kandidov, Opt. Lett. 22 (1997) 304.

[133] H. Schroeder and S.L. Chin, Opt. Commun. 234, (2004) 399.

[134] E.T.J. Nibbering, P.F. Curley, G. Grillon, B.S. Prade, M.A. Franco, F. Salin, and A. Mysyrowicz, Opt. Lett. 21 (1996) 62.

[135] V.P. Kandidov, O.G. Kosareva, I.S. Golubtsov, W. Liu, A. Becker, N. Akozbek, C.M. Bowden, and S.L. Chin, Appl. Phys. B 77 (2003) 149.

[136] A.B. Fedotov, E.E. Serebryannikov, A.A. Ivanov, and A.M. Zheltikov, Appl. Opt. 45 (2006) 6823.

[137] S. Coen, A.H.L. Chau, R. Leonhardt, J.D. Harvey, J.C. Knight, W.J. Wadsworth, and P.S.J. Russell, J. Opt. Soc. Am. B 19 (2002) 753.

[138] J. Darginavičius, G. Tamošauskas, G. Valiulis, and A. Dubietis, Opt. Commun. 282 (2009) 2995.

[139] A. Dubietis, G. Tamosauskas, P. Polesana, G. Valiulis, H. Valtna, D. Faccio, P. Di Trapani, A. Piskarskas, Opt. Express. 15 (2007) 11126.

[140] A. Dubietis, G. Tamošauskas, G. Valiulis, and A. Piskarskas, Laser Chem. 2008 (2008) 9.

[141] A.C. Bernstein, M. McCormick, G.M. Dyer, J.C. Sanders, and T. Ditmire, Phys Rev Lett. 102 (2009) 123902.

[142] Y. Liu, M. Durand, S. Chen, A. Houard, B. Prade, B. Forestier, and A. Mysyrowicz, Phys. Rev. Lett. 105 (2010) 055003

[143] B.D. Strycker, M. Springer, C. Trendafilova, X. Hua, M. Zhi, A.A. Kolomenskii, H. Schroeder, J. Strohaber, H.A. Schuessler, G.W. Kattawar, and A.V. Sokolov, Opt. Lett. 37 (2012) 16.

[144] L. Mees, K.F. Ren, G. Gréhan, and G. Gouesbet, Appl. Opt. 38 (1999) 1867.

[145] L.M. Sanchez-Breaa and E. Bernabeua, Optik - International Journal for Light and Electron Optics 112 (2001) 169.

[146] L.M. Sanchez-Brea and F.J. Salgado-Remacha, Appl. Opt. 47 (2008) 4804.

[147] R.W. Boyd, Nonlinear Optics, 3rd ed., Academic Press, Burlington MA, 2008.

[148] R.H. Stolen and C. Lin, Phys. Rev. A 17 (1978) 1448.

[149] A. Couairon and A. Mysyrowicz, Phys. Rep. 441 (2007) 47.

[150] M. Mlejnek, E.M. Wright, and J.V. Moloney, Opt. Lett. 23 (1998) 382.

[151] H.L. Xu, and S.L. Chin, Sensors 11 (2011) 32.

[152] J. Kasparian, M. Rodriguez, G. Méjean, J. Yu, E. Salmon, H. Wille, R. Bourayou, S. Frey, Y.-B. André, A. Mysyrowicz, R. Sauerbrey, J.-P. Wolf, and L. Wöste, Science 301 (2003) 61.

[153] F. Krausz and M. Ivanov, Rev. Mod. Phys. 81 (2009) 163.

[154] A. Pierre, F.D. Louis, Rep. Prog. Phys. 67 (2004) 813.

[155] E. Goulielmakis, M. Schultze, M. Hofstetter, V.S. Yakovlev, J. Gagnon, M. Uiberacker, A.L. Aquila, E.M. Gullikson, D.T. Attwood, R. Kienberger, F. Krausz, and U. Kleineberg, Science 320 (2008) 1614.

[156] R. Ackermann, G. Méchain, G. Méjean, R. Bourayou, M. Rodriguez, K. Stelmaszczyk, J. Kasparian, J. Yu, E. Salmon, S. Tzortzakis, Y.B. André, J.F. Bourrillon, L. Tamin, J.P. Cascelli, C. Campo, C. Davoise, A. Mysyrowicz, R. Sauerbrey, L. Wöste, and J.P. Wolf, Appl. Phys. B 82 (2006) 561.

[157] P. Polynkin, M. Kolesik, A. Roberts, D. Faccio, P. Di Trapani, and J. Moloney, Opt. Express 16 (2008) 15733.

[158] O.G. Kosareva, A.V. Grigor'evskii, and V.P. Kandidov, Quantum Electron. 35 (2005) 1013.

[159] S. Akturk, B. Zhou, M. Franco, A. Couairon, and A. Mysyrowicz, Opt. Commun. 282 (2009) 129.

[160] A. Schweinsberg, J. Kuper, and R.W. Boyd, Phys. Rev. A 84 (2011) 053837.

[161] S.L. Chin, W. Liu, F. Théberge, Q. Luo, S.A. Hosseini, V.P. Kandidov, O.G. Kosareva, N. Aközbek, A. Becker, H. Schroeder, Progress in Ultrafast Intense Laser Science III, Springer, Heidelberg, 2008.

[162] J. Durnin, J.J. Miceli, and J.H. Eberly, Phys. Rev. Lett. 58 (1987) 1499.

[163] J. Durnin, J. Opt. Soc. Am. A 4 (1987) 651.

[164] F.O. Fahrbach, P. Simon, and A. Rohrbach, Nat. Photonics 4 (2010) 780.

[165] J. Arlt, K. Dholakia, L. Allen, and M.J. Padgett, Phys. Rev. A 60 (1999) 2438.

[166] J. Durnin, J.H. Eberly, and J.J. Miceli, Opt. Lett. 13 (1988) 79.

[167] Z. Song, Z. Zhang, and T. Nakajima, Opt. Express 17 (2009) 12217.

[168] Z. Song and T. Nakajima, Opt. Express 18 (2010) 12923.

[169] M. Scheller, M.S. Mills, M.A. Miri, W.B. Cheng, J.V. Moloney, M. Kolesik, P. Polynkin, and D.N. Christodoulides, Nat. Photonics 8 (2014) 297.

[170] J.H. Marburger, Prog. Quant. Electron. 4, (1975) 35.

[171] J. Turunen, A. Vasara, and A.T. Friberg, Appl. Opt. 27 (1988) 3959.

[172] A. Brodeur and S.L. Chin, J. Opt. Soc. Am. B 16 (1999) 637.

[173] N. Kaya, J. Strohaber, A.A. Kolomenskii, G. Kaya, H. Schroeder, and H.A. Schuessler, Opt. Express 20 (2012) 13337.

[174] G. Steinmeyer, and C. Bree, Nat. Photonics 8 (2014) 271.

[175] V. Horvat, R.L. Watson, Phys. Rev. A 88 (2013) 022703.

[176] O. Jagutzki, A. Cerezo, A. Czasch, R. Dorner, M. Hattass, M. Huang, V. Mergel, U. Spillmann, K. Ullmann-Pfleger, T. Weber, H. Schmidt-Bocking, G. Smith, Nucl. Sci. Symp. Conf. Record, 2001 IEEE, 2001.

[177] W. Ketterle, H. Figger, and H. Walther, Phys. Rev. Lett. 55 (1985) 2941.

[178] D. Pavicic, PhD Dissertation, LMU Munich, 2004.

[179] C. Wunderlich, E. Kobler, H. Figger, and T.W. Hänsch, Phys. Rev. Lett. 78 (1997) 2333.

[180] K. Sändig, H. Figger, and T.W. Hänsch, Phys. Rev. Lett. 85 (2000) 4876.

[181] D. Pavičić, A. Kiess, T.W. Hänsch, and H. Figger, Phys. Rev. Lett. 94 (2005) 163002.

[182] D. Pavicic, A. Kiess, T.W. Hänsch, and H. Figger, Eur. Phys. J. D 26 (2003) 39.

[183] D. Pavičić, T.W. Hänsch, and H. Figger, Phys. Rev. A 72 (2005) 053413.

[184] A. Staudte, D. Pavičić, S. Chelkowski, D. Zeidler, M. Meckel, H. Niikura, M. Schöffler, S. Schössler, B. Ulrich, P.P. Rajeev, T. Weber, T. Jahnke, D.M. Villeneuve, A.D. Bandrauk, C.L. Cocke, P.B. Corkum, and R. Dörner, Phys. Rev. Lett. 98 (2007) 073003.

[185] S. Chelkowski, P.B. Corkum, and A.D. Bandrauk, Phys. Rev. Lett. 82 (1999) 3416.

[186] B. Feuerstein and U. Thumm, Phys. Rev. A 67 (2003) 043405.

[187] A.S. Alnaser, X.M. Tong, T. Osipov, S. Voss, C.M. Maharjan, P. Ranitovic, B. Ulrich, B. Shan, Z. Chang, C.D. Lin, and C.L. Cocke, Phys. Rev. Lett. 93 (2004) 183202.

[188] A. Staudte, C.L. Cocke, M.H. Prior, A. Belkacem, C. Ray, H.W. Chong, T.E. Glover, R.W. Schoenlein, and U. Saalmann, Phys. Rev. A 65 (2002) 020703.

[189] G.N. Gibson, M. Li, C. Guo, and J. Neira, Phys. Rev. Lett. 79 (1997) 2022.

[190] J.H. Posthumus, J. Plumridge, L.J. Frasinski, K. Codling, E.J. Divall, A.J. Langley, and P.F. Taday, J. Phys. B-At. Mol. Opt. 33 (2000) L563.

[191] I. Ben-Itzhak, P.Q. Wang, J.F. Xia, A.M. Sayler, M.A. Smith, K.D. Carnes, and B.D. Esry, Phys. Rev. Lett. 95 (2005) 073002.

[192] G. Herzberg, K.P. Huber, Molecular spectra and molecular structure, Van Nostrand Reinhold company, New York, 1979.

[193] H. Liebl and W.W. Harrison, Int. J. Mass Spectrom. and Ion Phys. 22 (1976) 237.

[194] H. Zhang, Ion Sources, Science Press, Beijing, 1999.

APPENDIX A

Gallery of Femtosecond Paraxial Modes (Experimental Data)

Hermite-Gaussian Modes

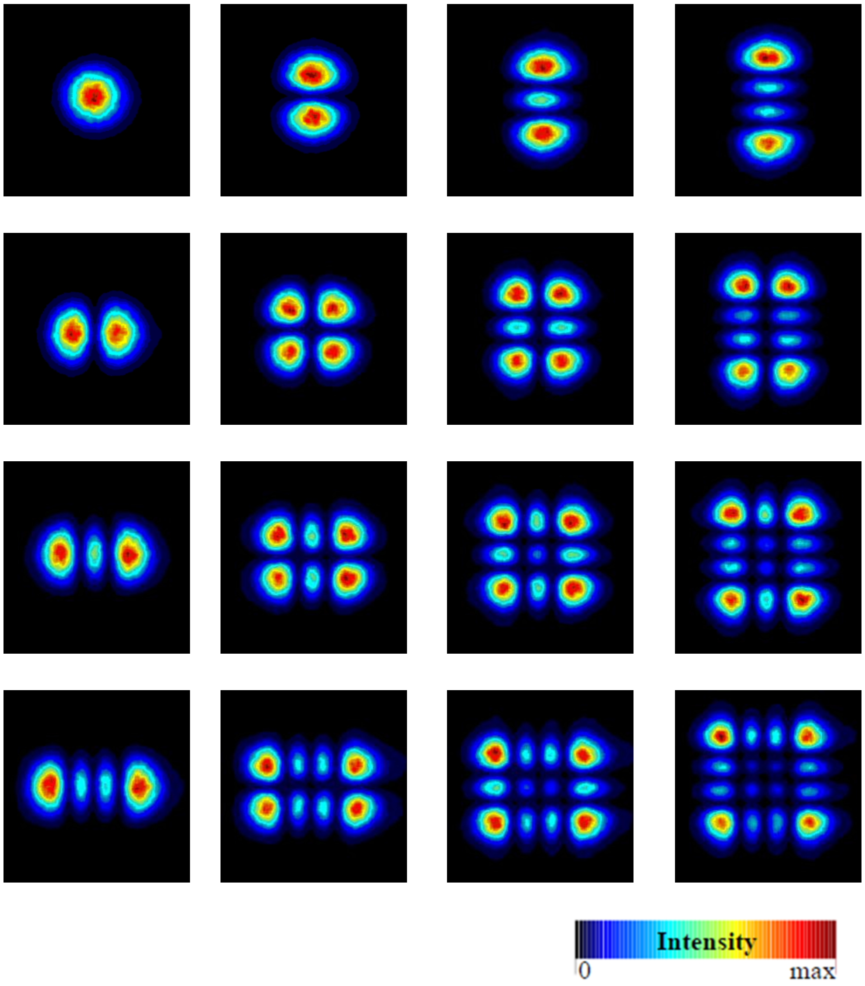

	$(0,0)$	$(0,1)$	$(0,2)$	$(0,3)$
mode key	$(1,0)$	$(1,1)$	$(1,2)$	$(1,3)$
(n,m)	$(2,0)$	$(2,1)$	$(2,2)$	$(2,3)$
	$(3,0)$	$(3,1)$	$(3,2)$	$(3,3)$

Laguerre-Gaussian Modes

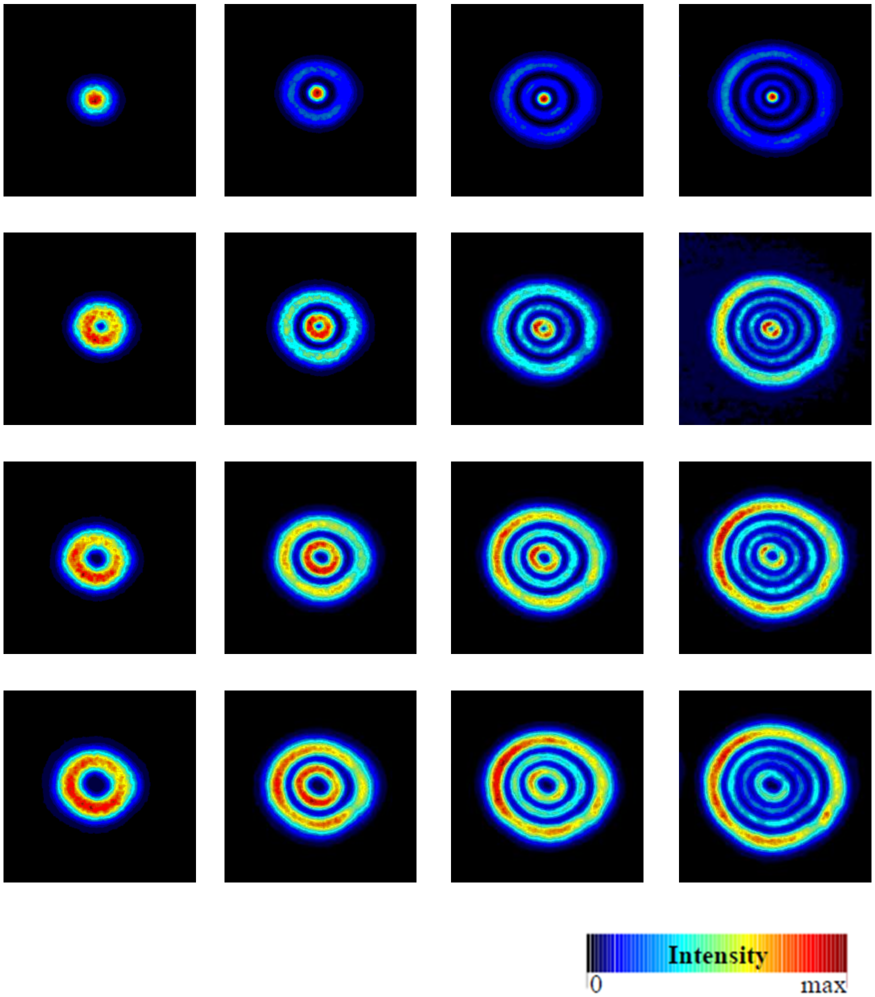

$$\begin{array}{cc} \text{mode key} & \begin{array}{cccc} (0,0) & (0,1) & (0,2) & (0,3) \\ (1,0) & (1,1) & (1,2) & (1,3) \\ (2,0) & (2,1) & (2,2) & (2,3) \\ (3,0) & (3,1) & (3,2) & (3,3) \end{array} \\ (p,l) & \end{array}$$

Even Laguerre-Gaussian Modes

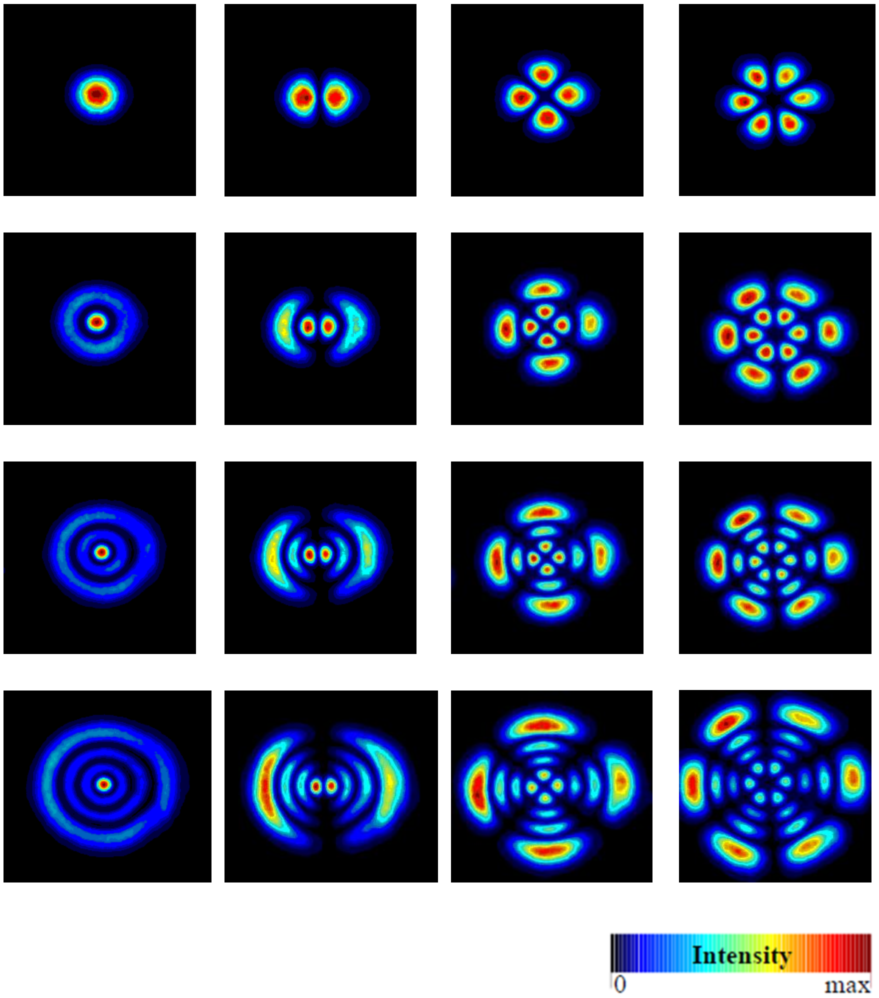

	$(0,0)$	$(0,1)$	$(0,2)$	$(0,3)$
mode key	$(1,0)$	$(1,1)$	$(1,2)$	$(1,3)$
(p,l)	$(2,0)$	$(2,1)$	$(2,2)$	$(2,3)$
	$(3,0)$	$(3,1)$	$(3,2)$	$(3,3)$

Odd Laguerre-Gaussian Modes

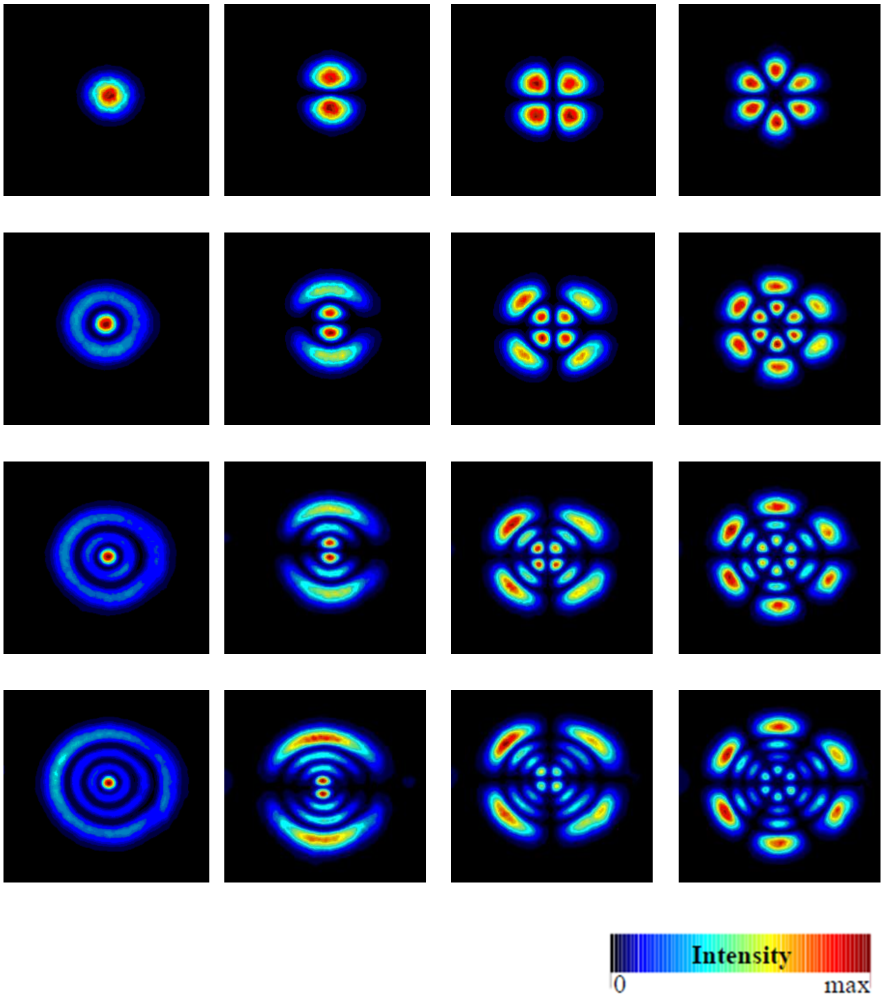

$$\begin{array}{ccccc} & (0,0) & (0,1) & (0,2) & (0,3) \\ \text{mode key} & (1,0) & (1,1) & (1,2) & (1,3) \\ (p,l) & (2,0) & (2,1) & (2,2) & (2,3) \\ & (3,0) & (3,1) & (3,2) & (3,3) \end{array}$$

APPENDIX B

Hermite-Gaussian hologram and Cartesian Knife-Edge code

```
%%
clear, clc
StepX=(0:90:360);
for QQQ=1:length(StepX)
    %HOLOGRAM PART %%%%%%%%%%%%%%%%%%%%%%%%%%%%%%%%%%%%%%%%%%%%%%%%%%%%%
    %%%%%%%%%%%%%%%%%%%%%%%%%%%%%%%%%%%%%%%%%%%%%%%%%%%%%%%%%%%%%%%%%%%%
    %Input Parameters %%%%%%%%%%%%%%%%%%%%%%%%%%%%%%%%%%%%%%%%%%%%%%
    K=8;% in lines per mm                                              %
    n=2;                                                               %
    m=1;                                                               %
    w=0.7;%waist in mm
%%%%%%%%%%%%%%%%%%%%%%%%%%%%%%%%%%%%%%%%%%%%%%%%%%%%%%%%%%%%%%%%%%%%%%%%
    %Conversion Stuff %%%%%%%%%%%%%%%%%%%%%%%%%%%%%%%%%%%%%%%%%%%%%%%%%%
    LCDsize=20.; %in mm                                                %
    Conversion=LCDsize/768; %mm per pixels                             %
    dx=792/4;%792/4 in pixels                                          %
    dy=600/2;%in pixels                                                %
    w=w/Conversion;% waist in pixels                                   %
%%%%%%%%%%%%%%%%%%%%%%%%%%%%%%%%%%%%%%%%%%%%%%%%%%%%%%%%%%%%%%%%%%%%%%%%

    %x,y,r,and theta for the hologram %%%%%%%%%%%%%%%%%%%%%%%%%%%%%%%%%%
    [X,Y] = meshgrid(-dx:1:dx-1,-dy:1:dy-1);
    [theta,r] = cart2pol(X,Y);                                         %
    r2=r.^2;
    %[X,Y] = meshgrid(-d:1:d,-d2:1:d2); theta=atan2(Y,X); r=X.^2+Y.^2;%

%%%%%%%%%%%%%%%%%%%%%%%%%%%%%%%%%%%%%%%%%%%%%%%%%%%%%%%%%%%%%%%%%%%%%%%%

    %Hermite Guassian %%%%%%%%%%%%%%%%%%%%%%%%%%%%%%%%%%%%%%%%%%%%%%%%%%
    Hn=HermitePoly(                                                    %
    Hm=HermitePoly(m);                                                 %
    amp1=0;                                                            %
    subamp1=0;                                                         %
    for k=1:length(Hn)
        subamp=Hn(k)*((sqrt(2)*X/w).^(n-2*(k-1))).*exp(-(r/w).^2);     %
        subamp1=subamp1+subamp;                                        %
    end
    for k=1:length(Hm)
        amp=Hm(k)*((sqrt(2)*Y/w).^(m-2*(k-1))).*subamp1;               %
        amp1=amp1+amp;                                                 %
    end
    amp1=amp1/(max(max(amp1)));                                        %
    amp2=abs(amp1);                                                    %

%%%%%%%%%%%%%%%%%%%%%%%%%%%%%%%%%%%%%%%%%%%%%%%%%%%%%%%%%%%%%%%%%%%%%%%%

    %Transmission Function %%%%%%%%%%%%%%%%%%%%%%%%%%%%%%%%%%%%%%%%%%%%%
    T=0.5*sawtooth(2*pi*K*Conversion*X+1*(0.5*sign(amp1)+0.5)*pi);     %
```

```
    MD2=0.5;                                                          %
    MM=MD2.*(amp2).*T+0.5; %for intensity masking                     %
    %MM=0.2.*(T+0.5); %for intensity masking                          %

%%%%%%%%%%%%%%%%%%%%%%%%%%%%%%%%%%%%%%%%%%%%%%%%%%%%%%%%%%%%%%%%%%%%%%%

    % KNIFE EDGING HALF OF SLM %%%%%%%%%%%%%%%%%%%%%%%%%%%%%%%%%%%%%%%
%%%%%%%%%%%%%%%%%%%%%%%%%%%%%%%%%%%%%%%%%%%%%%%%%%%%%%%%%%%%%%%%%%%%%%%
    MD=0.4;% modulation depth                                         %
    NP=4;% number of pixels per period                                %
    L1=600;%number of pixels in one dimension                         %
    L2=792/2;%number of pixels in the other dimension
    s=(MD/(NP-1));                                                    %
    TT=zeros(L1,NP);                                                  %
    yy=s*(0:1:NP-1);                                                  %
    for i=1:NP
        TT(:,i)=yy(i);                                                %
    end
    TTT=TT;                                                           %
    for i=1:ceil(L2/NP)
        TTT=[TTT TT];                                                 %
    end
    MM2=TTT(1:L1,1:L2);                                               %
    %%%%%%
    %Cartesian KnifeEdge %%%%%%%%%%%%%%%%%%%%%%%%%%%%%%%%%%%%%%%%%%%%%%
    X=StepX(QQQ); % in pixels                                         %
    %knifeedge in the x direction                                     %
    MM2(:,1:X)=0;                                                     %
    %knifeedge in the y direction                                     %
    %MM2(1:Y,:)=0;                                                    %

    %%%%%%%%%%%%%%%%%%%%%%%%%%%%%%%%%%%%%%%%%%%%%%%%%%%%%%%%%%%%%%%%%%%
    MM3=[fliplr(MM) MM2];                                             %
    %Plotting and Saving Images %%%%%%%%%%%%%%%%%%%%%%%%%%%%%%%%%%%%%%%
    figure, %                                                         %
    CA=[0 1]; %                                                       %
    surf(MM3),shading flat,caxis(CA),colormap(gray),view(2); axis
      equal,grid off%;%axis([1,L2*2,1,L1])         %
    imwrite(MM3,['C:\Documents and
      Settings\data\n',num2str(n),'_m',num2str(m),'_X',num2str(X),'.bmp
      '])  %
  %%
end
%%%%%%%%%%%%%%%%%%%%%%%%%%%%%%%%%%%%%%%%%%%%%%%%%%%%%%%%%%%%%%%%%%%%%%%
```

Required subroutine (HermitePoly)

```
function Hn = HermitePoly(n)

I=floor(n/2);
Hn = zeros(I+1,1);
for k=0:I
```

```
    Hn(k+1) = (-1)^k *(2)^(n-2*k) *
factorial(n)/factorial(k)/factorial(n-2*k);
end
```

Laguerre-Gaussian hologram and Radial and Azimuthal Knife-Edge code

```
%%
clear, clc
step=20;
StepX=(0:step:300);

for QQQ=1:length(StepX)

    %HOLOGRAM PART %%%%%%%%%%%%%%%%%%%%%%%%%%%%%%%%%%%%%%%%%%%%%%%%%%%%

%%%%%%%%%%%%%%%%%%%%%%%%%%%%%%%%%%%%%%%%%%%%%%%%%%%%%%%%%%%%%%%%%%%%%%%
    %Input Parameters %%%%%%%%%%%%%%%%%%%%%%%%%%%%%%%%%%%%%%%%%%%%%%%%%
    K=6;% in lines per mm                                             %
    m=2;%azimuzal mode number                                         %
    p=2;%radial mode number                                           %
    w=1.4;%%waist in mm                                               %

%%%%%%%%%%%%%%%%%%%%%%%%%%%%%%%%%%%%%%%%%%%%%%%%%%%%%%%%%%%%%%%%%%%%%%%

    %Conversion Stuff %%%%%%%%%%%%%%%%%%%%%%%%%%%%%%%%%%%%%%%%%%%%%%%%%
    LCDsize=20.; %in mm                                               %
    Conversion=LCDsize/768; %mm per pixels                            %
    dx=792/4;%d=768/2;%in pixels                                      %
    dy=600/2;                                                         %
    w=w/Conversion;%waist in pixels                                   %

%%%%%%%%%%%%%%%%%%%%%%%%%%%%%%%%%%%%%%%%%%%%%%%%%%%%%%%%%%%%%%%%%%%%%%%

    %X,Y,R,and theta for the hologram %%%%%%%%%%%%%%%%%%%%%%%%%%%%%%%%%
    [X,Y] = meshgrid(-dx:1:dx-1,-dy:1:dy-1);                          %
    [theta,r] = cart2pol(X,Y);                                        %
    r2=r.^2;                                                          %
    E=sqrt(2)*r/w;                                                    %

%%%%%%%%%%%%%%%%%%%%%%%%%%%%%%%%%%%%%%%%%%%%%%%%%%%%%%%%%%%%%%%%%%%%%%%

    %Amplitude Function %%%%%%%%%%%%%%%%%%%%%%%%%%%%%%%%%%%%%%%%%%%%%%%
    %coefficients of the Laguerre poly nomilas                        %
    Cpm=AssociatedLaguerrePoly(p,m);
    if m>0                                                            %
        Cpm=flipud(Cpm);%check to see if these were created backwards %
    end                                                               %
    amp1=0;                                                           %
    for k=0:length(Cpm)-1   %this builds the polynomials with the
coefficients Cpm                                                      %
        amp=Cpm(k+1)*(E.^2).^k;                                       %
        amp1=amp1+amp;                                                %
    end                                                               %
    G=(E.^m).*exp(-(r/w).^2);                                         %
    amp1=amp1.*G;                                                     %
    amp1=amp1/(max(max(amp1)));                                       %
```

```
%%%%%%%%%%%%%%%%%%%%%%%%%%%%%%%%%%%%%%%%%%%%%%%%%%%%%%%%%%%%%%%%%%%%%%%%
%%%%

    %add fresnel lens %%%%%%%%%%%%%%%%%%%%%%%%%%%%%%%%%%%%%%%%%%%%%%%%%%
    focus=1.5;                                                         %
    lambda=800e-6;                                                     %
    R=focus*lambda*1000;                                               %
    lens=0*pi*Conversion^2*r2/R;                                       %

%%%%%%%%%%%%%%%%%%%%%%%%%%%%%%%%%%%%%%%%%%%%%%%%%%%%%%%%%%%%%%%%%%%%%%%%
%%%

    %The transmission function
    T=5*cos(m*theta+2*pi*K*Conversion*X+(0.5*sign(amp1)+0.5)*pi+lens);%
    MM=0.2.*abs(amp1).*T+0.5; %for intensity masking

    %KNIFE EDGING HALF OF SLM %%%%%%%%%%%%%%%%%%%%%%%%%%%%%%%%%%%%%%%%%%
%%%%%%%%%%%%%%%%%%%%%%%%%%%%%%%%%%%%%%%%%%%%%%%%%%%%%%%%%%%%%%%%%%%%%%%%
    MD=1; %modulation depth                                            %
    NP=6; %number of pixels per period                                 %
    L1=600; %number of pixels in one dimension                         %
    L2=792/2; %number of pixels in the other dimension                 %
    s=(MD/(NP-1));                                                     %
    TT=zeros(L1,NP);                                                   %
    yy=s*(0:1:NP-1);                                                   %
    for i=1:NP                                                         %
        TT(:,i)=yy(i);                                                 %
    end                                                                %
    TTT=TT;                                                            %
    for i=1:ceil(L2/NP)                                                %
        TTT=[TTT TT];                                                  %
    end                                                                %
    MM2=TTT(1:L1,1:L2);                                                %

%%%%%%%%%%%%%%%%%%%%%%%%%%%%%%%%%%%%%%%%%%%%%%%%%%%%%%%%%%%%%%%%%%%%%%%%

    %Radial KnifeEdge%%%%%%%%%%%%%%%%%%%%%%%%%%%%%%%%%%%%%%%%%%%%%%%%%%%
    Rad=StepX(QQQ);                                                    %
    [XX YY]=meshgrid(1:1:L1,1:1:L2);                                   %
    [theta R]=cart2pol(XX-L1/2,YY-L2/2);                               %
    ZZ=abs(R);                                                         %
    mask=zeros(L1,L2);                                                 %
    ZZ(ZZ<=Rad)=1;                                                     %
    ZZ(ZZ>Rad)=0;                                                      %
    ZZ=ZZ';                                                            %
    MM2=MM2.*ZZ;                                                       %

    %Azimuthal KnifeEdge %%%%%%%%%%%%%%%%%%%%%%%%%%%%%%%%%%%%%%%%%%%%%%%
    Ang=StepX(QQQ); AN=Ang/360;                                        %
    mask=zeros(L1,L2);                                                 %
    ZZ=(theta+pi)/2/pi;                                                %
    ZZ(ZZ<=AN)=0;                                                      %
```

```
    ZZ(ZZ>AN)=1;                                                      %
    ZZ=ZZ';                                                           %
    %MM2=MM2.*ZZ;                                                     %
    %%%%%%%%%%%%%%%%%%%%%%%%%%%%%%%%%%%%%%%%%%%%%%%%%%%%%%%%%%%%%%%%%%%
    MM=[MM MM2];                                                      %
    %Plotting and Saving Images %%%%%%%%%%%%%%%%%%%%%%%%%%%%%%%%%%%%%%%
    figure,                                                           %
    CA=[0 1];                                                         %
    surf(MM),shading flat,caxis(CA),colormap(gray), view(2); axis
      equal,grid off%;%axis([1,L2*2,1,L1])
    %imwrite(MM,['C:\Users\necati\Desktop\necati\a.bmp'])
    %%%
end
%%%%%%%%%%%%%%%%%%%%%%%%%%%%%%%%%%%%%%%%%%%%%%%%%%%%%%%%%%%%%%%%%%%%%%%
```

Required subroutine (AssociatedLaguerrePoly)

```
function Lnk = AssociatedLaguerrePoly(n,k)

if k==0
    Lnk = zeros(n+1,1);
    for t=0:n
        Lnk(t+1) = (-1)^t*factorial(n)/factorial(n-
t)/((factorial(t))^2);
    end
else
    Lnk = zeros(n+1,1);

    for m=0:n
        Lnk(n+1-m) = (-1)^m * factorial(k+n)/factorial(n-
m)/factorial(k+m)/factorial(m);
    end

end
```

LG_1^1 hologram and two orthogonal knife-edge code for tomographic reconstruction

```
clear,clc

%HOLOGRAM
PART%%%%%%%%%%%%%%%%%%%%%%%%%%%%%%%%%%%%%%%%%%%%%%%%%%%%%%%%%%%%%%%%%%%%
%%%%%%%%%%%%%%%%%%%%%%%%%%%%%%%%%%%%%%%%%%%%%%%%%%%%%%%%%%%%%%%%%%%%%%%%
%Input Parameters   %%%%%%%%%%%%%%%%%%%%%%%%%%%%%%%%%%%%%%%%%%%%%%%%%%%%
K=8;%8 in lines per                                                    %
m=2;%azimuzal mode number                                              %
p=1;%radial mode number                                                %
w=1.4;%1.2;%waist in mm                                                %
%%%%%%%%%%%%%%%%%%%%%%%%%%%%%%%%%%%%%%%%%%%%%%%%%%%%%%%%%%%%%%%%%%%%%%%%
%Conversion Stuff %%%%%%%%%%%%%%%%%%%%%%%%%%%%%%%%%%%%%%%%%%%%%%%%%%%%%%
LCDsize=20.; %in mm                                                    %
Conversion=LCDsize/768; %mm per pixels                                 %
dx=792/4;%d=768/2;%in pixels                                           %
dy=600/2;
w=w/Conversion;%waist in pixels                                        %
%%%%%%%%%%%%%%%%%%%%%%%%%%%%%%%%%%%%%%%%%%%%%%%%%%%%%%%%%%%%%%%%%%%%%%%%
%X,Y,R,and theta for the hologram %%%%%%%%%%%%%%%%%%%%%%%%%%%%%%%%%%%%%%
[X,Y] = meshgrid(-dx:1:dx-1,-dy:1:dy-1);                               %
[theta,r] = cart2pol(X,Y);                                             %
r2=r.^2;                                                               %
E=sqrt(2)*r/w;
%%%%%%%%%%%%%%%%%%%%%%%%%%%%%%%%%%%%%%%%%%%%%%%%%%%%%%%%%%%%%%%%%%%%%%%%
%Amplitude Function %%%%%%%%%%%%%%%%%%%%%%%%%%%%%%%%%%%%%%%%%%%%%%%%%%%%
%coefficients of the Laguerre polynomials                              %
Cpm=AssociatedLaguerrePoly(p,m);
if m>0                                                                 %
    Cpm=flipud(Cpm);%check to see if these were created backwards      %
end                                                                    %
amp1=0;                                                                %
for k=0:length(Cpm)-1        %this builds the polynomials with the
coefficients Cpm                                                       %
    amp=Cpm(k+1)*(E.^2).^k;                                            %
    amp1=amp1+amp;                                                     %
end                                                                    %
G=(E.^m).*exp(-(r/w).^2);                                              %
amp1=amp1.*G;                                                          %
amp1=amp1/(max(max(amp1)));                                            %
%%%%%%%%%%%%%%%%%%%%%%%%%%%%%%%%%%%%%%%%%%%%%%%%%%%%%%%%%%%%%%%%%%%%%%%%
%The transmission function                                             %
T=cos(m*theta+2*pi*K*Conversion*X+(0.5*sign(amp1)+0.5)*pi);
MM1=abs(amp1).*T+0.5;
%%%%%%%%%%%%%%%%%%%%%%%%%%%%%%%%%%%%%%%%%%%%%%%%%%%%%%%%%%%%%%%%%%%%%%%%
%DOUBLE-KNIFE-EDGING HALF OF SLM
%%%%%%%%%%%%%%%%%%%%%%%%%%%%%%%%%%%%%%%%%%
nx=120;   ny=80;
ResX=600; ResY=400;
MD=1.2;          %modulation depth
NP=6;             %number of pixels per period
```

```
L1=ResX;        %number of pixels in one dimension
L2=ResY;        %number of pixels in the other dimension
s=(MD/(NP-1));    %slope of a line
TT=zeros(L1,NP);

yy=s*(0:1:NP-1);  %equation of a line
for i=1:NP
    TT(:,i)=yy(i);
end
TTT=TT;
for i=1:ceil(L2/NP)
    TTT=[TTT TT];
end
MM=TTT(1:L1,1:L2);
%%%%%%

for I1=1:nx
    StepY=(ResY/ny)*I1;
    for I2=1:ny
        StepX=(ResX/nx)*I2;

        X=StepX; Y=StepY; % in pixels
        %knifeedge in the x direction
        MM2=MM;
        MM2(:,1:X)=0;
        %knifeedge in the y direction
        MM2(1:Y,:)=0;
        %%%%%%%%%
        CA=[0,1];
        MM3=[MM1 MM2];
        surf(MM3,'linestyle','none');caxis(CA); axis off; axis equal;
view(2); colormap gray
        III=(I1-1)*nx+I2
        F(III)=getframe;
    end
end
%%%%saving%%%%%%%%%%%%%%%%%%%%%%%%%%%%%%%%%%%%%%%%%%%%%%%%%%%%%%%%%%%%%
movie2avi(F,'C:\Users\necat_001\Desktop\test\test1','fps',30);        %
%%%%%%%%%%%%%%%%%%%%%%%%%%%%%%%%%%%%%%%%%%%%%%%%
%M(k) = getframe(gcf); in a loop over index k.
%movie2avi(M,'movie2','fps',10,'quality',75,'videoname','movie2','compr
ession','cvid'),
```

Required subroutine (AssociatedLaguerrePoly)

```
function Lnk = AssociatedLaguerrePoly(n,k)

if k==0
    Lnk = zeros(n+1,1);
    for t=0:n
```

```
        Lnk(t+1) = (-1)^t*factorial(n)/factorial(n-
t)/((factorial(t))^2);
    end
else
    Lnk = zeros(n+1,1);

    for m=0:n
        Lnk(n+1-m) = (-1)^m * factorial(k+n)/factorial(n-
m)/factorial(k+m)/factorial(m);
    end

end
```

APPENDIX C

Duoplasmatron ion source parts and its electronic circuit connections

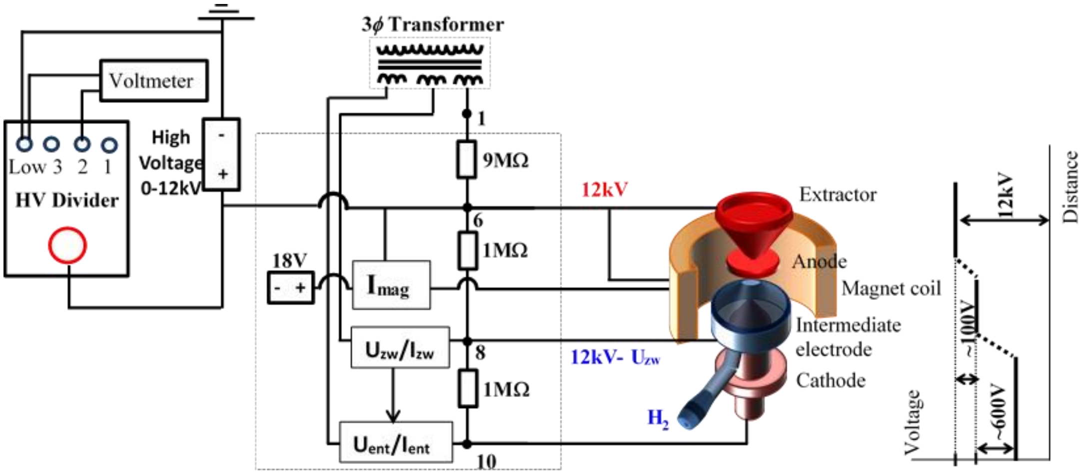

Main ion source parts and its electronic circuit connections. The duoplasmatron ion source consists two plasma regions; the lower density plasma between the cathode and the intermediate electrode (IE) and the high density plasma between the IE and the anode. I_{mag}: current through the electromagnet (Magnet coil) to create a magnetic field for ionization efficiency (0.0-2.5A).

U_a: positive acceleration voltage (Extractor electrode) to extract the positive ions U_a =12kV.

I_s: current from extractor electrode I_s ~0.100mA.

U_{zw}: Voltage on the IE (0-100V).

I_{zw}: current from the IE (-300-0-+300mA).

U_{ent}: Voltage on the cathode (Hollow cathode) to create and accelerate free electrons (0 -600V).

I_{ent}: current of electrons from the cathode (0-400mA).

APPENDIX D

In situ tomography of femtosecond optical beams with a holographic knife-edge

This journal article is reprinted with permission from The Optical Society. This journal article can be found at http://dx.doi.org/10.1364/OE.19.014321.

In situ tomography of femtosecond optical beams with a holographic knife-edge

J. Strohaber,[1,*] G. Kaya,[1] N. Kaya,[1]
N. Hart,[1] A. A. Kolomenskii,[1] G. G. Paulus,[1,2] and H. A. Schuessler[1]

[1]Department of Physics, Texas A&M University, College Station, TX 77843-4242, USA
[2]Institut für Optik und Quantenelektronik, Max-Wien-Platz 1, 07743 Jena, Germany
[*]jstroha1@physics.tamu.edu

Abstract: We present an in situ beam characterization technique to analyze femtosecond optical beams in a folded version of a 2f-2f setup. This technique makes use of a two-dimensional spatial light modulator (SLM) to holographically redirect radiation between different diffraction orders. This manipulation of light between diffraction orders is carried out locally within the beam. Because SLMs can withstand intensities of up to $I \sim 10^{11}$ W/cm^2, this makes them suitable for amplified femtosecond radiation. The flexibility of the SLM was demonstrated by producing a diverse assortment of "soft apertures" that are mechanically difficult or impossible to reproduce. We test our method by holographically knife-edging and tomographically reconstructing both continuous wave and broadband radiation in transverse optical modes.

OCIS codes: (090.1760) Computer holography; (050.1590) Chirping; (050.1950) Diffraction gratings; (140.3300) Laser beam shaping; (320.7090) Ultrafast lasers; (050.4865) Optical vortices.

References and links

1. M. Babiker, W. L. Power, and L. Allen, "Light-induced torque on moving atoms," Phys. Rev. Lett. **73**(9), 1239–1242 (1994).
2. A. Picón, J. Mompart, J. R. Vázquez de Aldana, L. Plaja, G. F. Calvo, and L. Roso, "Photoionization with orbital angular momentum beams," Opt. Express **18**(4), 3660–3671 (2010).
3. A. Alexandrescu, D. Cojoc, and E. Di Fabrizio, "Mechanism of angular momentum exchange between molecules and Laguerre-Gaussian beams," Phys. Rev. Lett. **96**(24), 243001 (2006).
4. E. Serabyn, D. Mawet, and R. Burruss, "An image of an exoplanet separated by two diffraction beamwidths from a star," Nature **464**(7291), 1018–1020 (2010).
5. J. H. Lee, G. Foo, E. G. Johnson, and G. A. Swartzlander, Jr., "Experimental verification of an optical vortex coronagraph," Phys. Rev. Lett. **97**(5), 053901 (2006).
6. J. Y. Vinet, "Thermal noise in advanced gravitational wave interferometer antennas: A comparison between arbitrary order Hermite and Laguerre Gasussian modes," Phys. Rev. D Part. Fields Gravit. Cosmol. **82**(4), 042003 (2010).
7. L. T. Vuong, T. D. Grow, A. Ishaaya, A. L. Gaeta, G. W. 't Hooft, E. R. Eliel, and G. Fibich, "Collapse of optical vortices," Phys. Rev. Lett. **96**(13), 133901 (2006).
8. J. Ng, Z. Lin, and C. T. Chan, "Theory of optical trapping by an optical vortex beam," Phys. Rev. Lett. **104**(10), 103601 (2010).
9. M. A. Bandres and J. C. Gutiérrez-Vega, "Ince-Gaussian beams," Opt. Lett. **29**(2), 144–146 (2004).
10. J. Strohaber, C. Petersen, and C. J. G. J. Uiterwaal, "Efficient angular dispersion compensation in holographic generation of intense ultrashort paraxial beam modes," Opt. Lett. **32**(16), 2387–2389 (2007).
11. J. Leach, M. R. Dennis, J. Courtial, and M. J. Padgett, "Laser beams: knotted threads of darkness," Nature **432**(7014), 165 (2004).
12. K. Bezuhanov, A. Dreischuh, G. G. Paulus, M. G. Schätzel, and H. Walther, "Vortices in femtosecond laser fields," Opt. Lett. **29**(16), 1942–1944 (2004).
13. I. G. Mariyenko, J. Strohaber, and C. J. G. J. Uiterwaal, "Creation of optical vortices in femtosecond pulses," Opt. Express **13**(19), 7599–7608 (2005).
14. I. Zeylikovich, H. I. Sztul, V. Kartazaev, T. Le, and R. R. Alfano, "Ultrashort Laguerre-Gaussian pulses with angular and group velocity dispersion compensation," Opt. Lett. **32**(14), 2025–2027 (2007).
15. J. Strohaber, T. D. Scarborough, and C. J. G. J. Uiterwaal, "Ultrashort intense-field optical vortices produced with laser-etched mirrors," Appl. Opt. **46**(36), 8583–8590 (2007).

#146202 - $15.00 USD Received 19 Apr 2011; revised 2 Jul 2011; accepted 2 Jul 2011; published 12 Jul 2011

16. J. A. Davis, D. M. Cottrell, J. Campos, M. J. Yzuel, and I. Moreno, "Encoding amplitude information onto phase-only filters," Appl. Opt. **38**(23), 5004–5013 (1999).
17. J. B. Bentley, J. A. Davis, M. A. Bandres, and J. C. Gutiérrez-Vega, "Generation of helical Ince-Gaussian beams with a liquid-crystal display," Opt. Lett. **31**(5), 649–651 (2006).
18. J.W. Goodman, *Introduction to Fourier Optics*, 2nd Ed. (McGraw-Hill,New York, 1996).
19. J. F. James, *A Student's Guide tothe Fourier Transform* (Cambridge U. Press, 1995).
20. J. M. Khosrofian and B. A. Garetz, "Measurement of a Gaussian laser beam diameter through the direct inversion of knife-edge data," Appl. Opt. **22**(21), 3406–3410 (1983).
21. O. Mendoza-Yero and M. Arronte, "Determination of Hermite Gaussian modes using moving knife-edge," J. Phys: Conference Series **59**, 497–500 (2007).
22. J. Soto, M. Rendón, and M. Martín, "Experimental demonstration of tomographic slit technique for measurement of arbitrary intensity profiles of light beams," Appl. Opt. **36**(29), 7450–7454 (1997).
23. S. Quabis, R. Dorn, M. Eberler, O. Glöckl, and G. Leuchs, "The focus of light- theoretical calculation and experimental tomographic reconstruction," Appl. Phys. B **72**, 109–113 (2001).

1. Introduction

Optical beam modes have drawn considerable interest in the scientific community over the past few decades. These transverse optical modes, which are eigensolutions of the paraxial wave equation in different coordinate geometries, consist of the Hermite-Gaussian, Laguerre-Gaussian and more recently the Ince-Gaussian beams. Radiation in these transverse modes have been used in a broad range of disciplines having applications in the optical manipulation of atomic and molecular systems [1–3], optical vortex coronagraph for the direct imaging of exoplanets, thermal noise in gravitation wave interferometric antennas [4–6], ultrashort intense-field filamentation experiments [7], and optical trapping [8]. The Laguerre-Gaussian beams are of considerable interest because radiation in these transverse modes carries, in addition to intrinsic angular momentum, a sharp quantized amount of optical orbital angular momentum equal to $\ell\hbar$ per photon. Recent theoretical work has suggested that this additional angular momentum can couple to the internal degrees of freedom of a molecular system in addition to external degrees of freedoms as in [3]. Our plans are to produce intense femtosecond optical vortices in a "pure" transversal mode such that the angular momentum per photon is sharp i.e., beams which are not in a superposition of eigenmodes having different angular momentum quantum numbers.

When producing optical beam modes, a common approach is to use gratings, where phase and amplitude information about the mode is encoded within the grating structure [9,10]. This approach works well when the light used is monochromatic [11], however, when polychromatic light such as femtosecond radiation is used a compensation technique is needed in order to correct for angular dispersion. This need for compensation has been met with a variety of successful experimental techniques [12–15]. In most of these experimental setups, a second dispersive optical element was used as the compensator. In this paper, we introduce a method for the in situ analysis of optical beams by using the needed second pass of the folded version of a 2*f*-2*f* setup (folded-2*f*) to "holographically knife-edge" optical beams, which were produced in the first pass of the setup [15]. As a note, in principle our technique can be used in a folded version of the 4f-setup [14]. The focusing element in the 2*f*-2*f* or folded-2*f* setup reverses the sign of the angular dispersion causing the dispersed broadband beam to exhibit a zero amount of *spatial dispersion* at the position of the second grating [13]. At all other positions within the setup, except at the position of the first grating, the beam will exhibit some degree of "blurriness" in the dispersion plane. Because of this—while the beam still exhibits *angular dispersion*—it is possible to knife-edge and tomographically reconstruct the beam it situ at the position of the second grating pass. In this paper, we will show how this can be carried out using holographic techniques

There are several attractive aspects of this it situ beam characterization. Compared to CCD beam profilers and cameras, SLM's can withstand intensities of up to $I \sim 10^{11}$ W/cm^2 because laser radiation is transmitted instead of absorbed by them, and the active area of a SLM's LCD is typically larger than that found for the CCD chips in beam profilers and cameras. Compared to mechanical knife-edge methods such as razor blades and irises (hard apertures), SLMs are highly flexible having no moving parts; multiple knife-edge directions

#146202 - $15.00 USD Received 19 Apr 2011; revised 2 Jul 2011; accepted 2 Jul 2011; published 12 Jul 2011

can be performed without the need of a spinning drum perforated with holes. SLMs can be used to generate complex two-dimensional shapes, and because their pixels are fixed there is a high degree of reproducibility. We will show that SLM's can produce virtually any desired geometric aperture using its LCD (soft aperture). Furthermore, The SLM has a refresh rate of 60 Hz allowing for measurements to be taken in real time. In addition to tomographic reconstruction, a few beam characteristics such as the beam waist and the relative power between modal lobes can be determined by using only a few knife-edge measurements—as long as the beam is nearly ideal.

2. Spatial Light Modulator (SLM)

The SLM (Hamamatsu LCOS-SLM X10468-02) used in this work was designed to function optimally for wavelengths within the range of 750 nm to 850 nm meaning that the antireflective coating and dielectric retroreflecting mirror (R>95%) are optimized for operation in this wavelength range. Some of our future goals involve the use of continuous wave radiation from a He-Ne source in addition to 800-nm femtosecond from a broadband radiation source. The difference in wavelength is expected to affect the reflectivity due to the spectral response of the SLM's optics. In contrast to the programmable phase modulator (PPM) used in [13], the LCOS-SLM is a pixelated device, which consequently results in a loss of power due to parasitic diffraction effects. In all experiments carried out in this work, noticeable amount of light was observed in higher diffraction orders. For the above mentioned reasons, the reflectivity of the SLM for the He-Ne wavelength was determined by taking the ratio of the spectrally reflected (zero order) and incident laser powers when a constant phase modulation was displayed on the SLM's LCD (encoded in the grayscale value of a picture). The reflectivity was found to be $R \approx 76\%$.

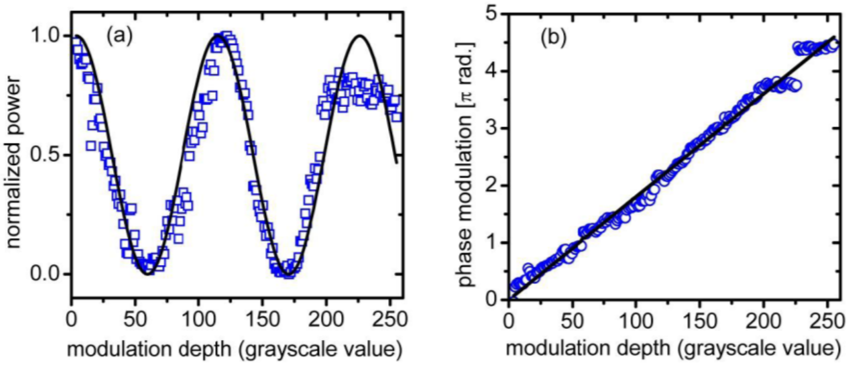

Fig. 1. (a) Measured output power of a Michelson interferometer versus modulation depth (blue squares). The SLM was positioned in one arm of the interferometer and introduced a phase-modulation encoded as a grayscale value. The solid curve is the theoretically expected result. (b) Phase modulation retrieved from the data and theoretical curve shown in panel (a).

Besides the spectral response of the optical coatings, another consideration is the induced phase modulation as a function of the applied voltage or programmed grayscale value when using 633 nm radiation instead of 800 nm. The phase modulation of the SLM was factory-calibrated using 800 nm and was shown to produce over 2π radians of phase modulation. A quick calculation shows that for the 633 nm He-Ne wavelength a larger phase modulation is expected $\Delta\varphi_{633} = 3.2\pi$. To experimentally determine the phase modulation as a function of displayed grayscale value, the SLM was incorporated into one arm of a Michelson interferometer. This interferometer was constructed with fixed arms, so that phase changes are introduced only by the SLM. A uniform grayscale image (600 × 792 pixels) was computer

#146202 - $15.00 USD Received 19 Apr 2011; revised 2 Jul 2011; accepted 2 Jul 2011; published 12 Jul 2011

generated having a specific grayscale value between 0 and 255. This image was subsequently displayed on the SLM through a digital visual interface (DVI) connection and the output power of the interferometer was measured (Ophir PD300-UV) as a function of grayscale value. Recorded data (blue squares) are shown in Fig. 1(a) and have been fitted to the theoretically expected result $P = P_0 \cos^2(\varphi/2)$ (solid black curve). From this fit, the phase modulation as a function of grayscale value was determined from $\varphi = 2\arccos\left(\sqrt{P/P_0}\right)$. From this fit, the phase modulation as a function of grayscale value was determined from e^{iC}. Figure 1(b) shows the phase modulation given as a function of grayscale value. The phase modulation φ as a function of grayscale value χ was found to be described by a linear function $\varphi = m\chi \approx (1.8\pi/100)\chi$ with a maximum phase modulation of $\sim 4\pi$ radians for a grayscale value of $\chi = 200$, which is in rough agreement with our estimate. For grayscale values greater than ~200, the phase modulation introduced by the SLM exhibited a nearly constant behavior. This can be seen by the blue squares in Fig. 1(a) where the data points deviate from the theoretical curve. Consequently, as seen by the blue circles in Fig. 1(b), a gap appears in the data for phase modulation versus grayscale value. The reason for this is not known, but for experiments reported here, phase modulations of less than 2π radian, corresponding to grayscale values less than ~100, were used.

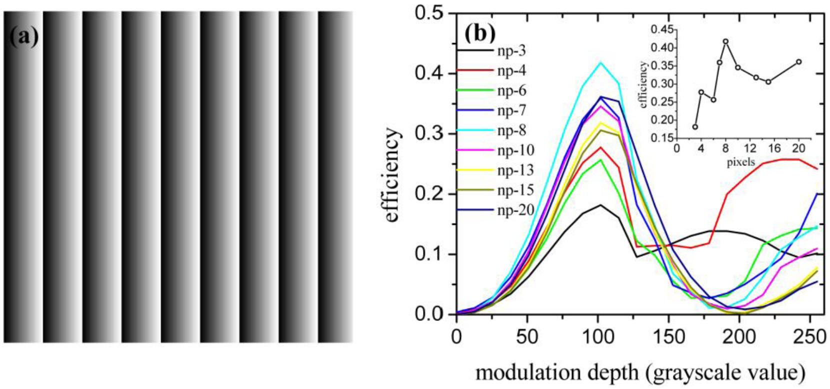

Fig. 2. (a) Illustration of a blazed phase grating having modulation depth m and spatial period Λ displayed on the SLM. (b) Blazing efficiency as a function of modulation depth measured as the ratio of the power in the first diffraction order to that in the zero order. Nine sets of data were obtained each having a different grating period and denoted by the number of pixels (np) used for the grating period. Each pixel is assumed to be equal to the pitch, which is 20 μm. All data sets show a peak at a grayscale value of ~100, which corresponds to a phase shift of 2π radian. The inset in panel (b) shows the efficiencies for the peak values (grayscale value of 100) demonstrating the best achieved diffraction efficiency for a grating period of 8 pixels.

Since we use our SLM in a folded version of a $2f-2f$ setup to compensate for angular dispersion [15], we find it convenient to use the second half of the SLM's LCD to characterize the amplitude-phase-modulated optical beams produced on the first pass of the setup. This was accomplished using an amplitude-phase encoding method on a phase-only device, which makes use of blazing techniques [10,16,17]. For these reasons, two parameters were explored in this experiment: the grating period Λ measured in pixels ($20\ \mu$m pitch) and the modulation depth m given in grayscale value. The purpose of this measurement was to experimentally determine the optimal blazing conditions. Nine sets of data were recorded; one for each value of the grating period $\Lambda = \{3,4,6,7,8,10,13,15,20\}$. For each data set, the first order diffraction efficiency was measured as a function of modulation depth. For all data sets, each having a different grating constant, the maximum efficiency was found to correspond to a modulation depth having a grayscale value of roughly 105, which from the calibration data is a phase modulation of $\sim 2\pi$ radians. The peak in the diffraction efficiency curves at this value of the phase is in agreement with that expected from diffraction theory when using blazed grating [18,19]. The diffraction efficiency is expected to increase with increasing number of steps [18]. This increase is experimentally observed; however, the data in the inset shows that in the first diffraction order, the efficiency was found to be optimal for a grating period of 8 pixels or $\Lambda = 160\mu m$ and then decreased. Based on the results shown in Fig. 2 all gratings used in this work were designed to have a grating period of $\Lambda = 160\mu m$, which corresponded to a diffraction angle of $\theta \approx 4 mrad$ for 633 nm, and a phase modulation depth of 2π or less.

3. Equivalence between Holographic and Mechanical Knife-Edge Methods

In this work, we employ a technique that uses a phase hologram encoded with phase and amplitude information to knife edge eigenmodes of the paraxial wave equation. The commonly-known knife-edge measurements use hard apertures and are amplitude modulators. It will be shown that by using off-axis holography from a phase-only modulator, the first order diffracted beam from a knife-edge hologram is proportional to an amplitude knife-edge.

Immediately preceding a mechanical knife edge or holographic grating, the electric field is assumed to have a constant phase e^{iC} and an arbitrary amplitude profile $\psi(x)$, i.e., Gaussian. For the mechanical knife edge, the radiation is modified such that only the spatial amplitude has changed and immediately following the knife-edge the electric field is $E_{\text{mech}} = H(x-\xi)\psi(x)$, where $H(x-\xi)$ is the Heaviside function, and ξ is the position of the knife-edge. For the holographic knife-edge, as shown in Fig. 3(a), the electric field immediately following the grating is phase modulated only, but due to the choice in phase modulation the electric field amplitude in different diffraction orders can be modified locally. In this work, blazed gratings are used to control local diffraction efficiencies; however, to keep the present analysis tractable sinusoidal gratings are used [18]. The field directly following the grating can be written as the sum of a constant phase (left half of grating in Fig. 3(a)) and a sinusoidal phase modulation (right half of grating in Fig. 1(b)),

$$E_{\text{holo}} = \left(H(\xi - x) + H(x-\xi) \sum_{q=-\infty}^{\infty} J_q\left(\frac{m}{2}\right) e^{iqKx} \right) \psi(x). \tag{1}$$

Here the Jacobi-Anger expansion has been used in the second term to expand the sinusoidal phase grating $\exp[i(m/2)\sin(Kx)]$ in terms of plane waves with coefficients given by Bessel functions of the first kind $J_q(x)$. The modulation depth of the sinusoidal phase grating is giving by m and $K = 2\pi/\Lambda$ is the grating constant having a spatial period of Λ. The first term in Eq. (1) is the electric field amplitude $\psi(x)$ that has been "cut" by the holographic knife-edge function $H(\xi - x)$. This first term and the $q = 0$ term direct light into the zero order. All terms in the sum with $q \neq 0$ are responsible for redirecting radiation into higher diffraction orders. This can be seen from the argument of the exponential qK. If the diffraction orders are allowed to separate, then to a good approximation the electric field in

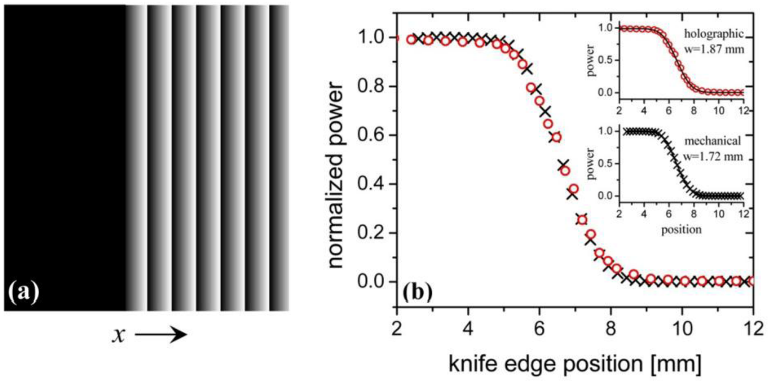

Fig. 3. (a) Illustration of a hologram used to create a holographic knife-edge. The solid black color on the left side of hologram denotes a constant phase modulation and the right side of the hologram is that of a blazed grating. (b) Measured power as a function of knife-edge position. The black crosses represent the measured power from a mechanical knife-edge position at the location of the SLM, and the red circles are that obtained from the holographic knife-edge. Both mechanical and holographic knife-edge measurements are in good agreement. The insets are fits of the data to theoretical curves.

the first diffraction order can be taken as $E_{\text{holo}} \approx H(x-\xi)J_1(m/2)e^{iKx}\psi(x)$. Because this separation is possible and because the exact intensity profile is unimportant since it is integrated over by a power meter, it is not necessary to propagate this field using the Huygens-Fresnel-Kirchhoff integral. As can be seen, this field consists of the field from the mechanical knife edge $E_{\text{mech}} = H(x-\xi)\psi(x)$, therefore we can combined both equations and take the modulus squared to determine the intensity going into the first diffraction order $I_{\text{holo}}(x;\xi) = J_1^2(m/2)I_{\text{mech}}(x;\xi)$. Since $J_1(m/2)$ is a constant, this last result states that the intensity of the holographic knife-edge is proportional to that of the mechanical knife-edge. The power is then found by integrating over all space $P_{\text{holo}}(\xi) = J_1^2(m/2)P_{\text{mech}}(\xi)$. As a note, the proportionality factor will be different for different types of gratings such as a blazed grating. The zero and higher orders also contain knife-edge information, but these orders contain residual angular dispersion and for this reason may not be the best choice to measure the power. Additionally, the corrected first order can be imaged with a CCD camera for further analysis.

To experimentally investigate the equivalence between the holographic knife-edge and the more traditional mechanical knife-edge, the fundamental Gaussian laser beam from a He-Ne laser was used for comparison of the two methods. Figure 3 shows the results of both measurements. The mechanical knife-edge was performed at the position of the SLM. The holographic knife-edge was performed using a grating similar to that shown in Fig. 3(a) with $\Lambda = 160\,\mu\text{m}$ and $\varphi = 2\pi$. The discontinuity at x was scanned, and the knife-edge data was recorded by a photodiode. The waist of the Gaussian beam was found to be roughly ~2 mm, which was obtained by fitting the data with $P = P_0\text{erfc}(\sqrt{2}x/w)/2$. This is in agreement with the size of the output of the He-Ne laser (~0.5 mm) after passing through a beam expander, which had a magnification of four times (~2 mm). More precisely these values were found to be 1.87 mm and 1.72 mm for the holographic and mechanical knife edge measurements respectively, inset in Fig. 3(b). The two sets of data are in good agreement, demonstrating that the holographic knife-edge can be effectively used to characterize laser beams. To further demonstrate the utility of this method, a number of different optical modes were created and analyzed using this knife-edge method. To the best of our knowledge, knife-edge equations

Received 19 Apr 2011; revised 2 Jul 2011; accepted 2 Jul 2011; published 12 Jul 2011

for the Hermite and Laguerre Gaussian modes have not been shown in the literature. The derivation of these equations is the topic of the subsequent sections. There exists another family of solutions to the paraxial wave equation known as the Ince-Gaussian modes. These solutions are mathematically somewhat more difficult to deal with than the HG and LG modes and for this reason will not be considered here. However, it is noted that the IG modes are an excellent example where a "soft aperture" is easier to make than a "hard aperture". This is because the natural choice for knife-edging these beams consists of confocal ellipses and hyperbolas.

4. Experimental Setup

Figure 4 shows an illustration of the experimental setup used to generate and analyze the paraxial beams used in this work. Since only a single SLM was used in this experiment, the SLM's display was divided into halves, each half having a different hologram: the first hologram was encoded with phase-amplitude information to produce a desired optical beam, and the second was encoded with the holographic knife-edge. An example hologram is shown in the inset of Fig. 4.

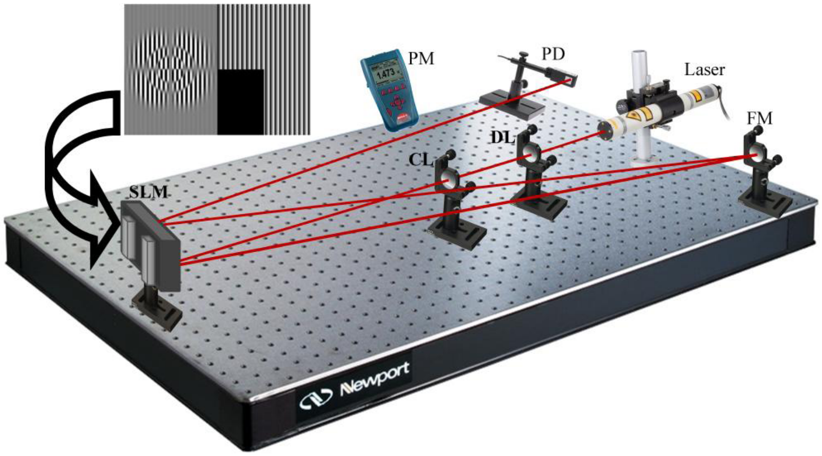

Fig. 4. Experimental setup. Laser radiation from either a He-Ne or Ti:sapphire laser enters the setup from the right. DL = 50 cm diverging lens, CL = 200 cm converging lens, SLM = spatial light modulator, FM = folding mirror placed a distance of $f = 100\text{ cm}$ away from the SLM, PD = photodiode power meter head, PM = power meter. The upper left inset is an example-hologram to create a $LG^{o}_{2,2}$ beam followed by an angular knife-edge.

This setup is similar in design to the folded-2f setup used in [15]. Laser light from two different sources were used in this work. Monochromatic radiation was from a He-Ne laser (Melles Griot) having a maximum output power of 2.5 mW, a wavelength of 633 nm and a $e^{1/2}$ beam waist of 0.5 mm. Broadband radiation was produced from a KMLabs femtosecond oscillator having a repetition rate of ~80 MHz, ~50 nm of bandwidth with a center wavelength of 800 nm and an output power of ~400 mW. This radiation was magnified by a telescoping beam expander consisting of a 50 mm diverging lens (DL) and a 200 mm converging lens (CL) to give a magnification of $M = 4$ and resulting in a final beam size of ~2 mm. This beam waist was verified by mechanical and holographic knife-edge measurements. The expanded beam was shone onto a spatial light modulator (Hamamatsu LCOS-SLM X10468). The SLM was a parallel aligned liquid crystal on silicon (LCOS) spatial light modulator having a resolution of 800x600 pixels (16 mm x 12 mm), and a maximum reflectivity of >95% for radiation between 750 nm and 850 nm. The SLM was capable of modulating the

#146202 - $15.00 USD Received 19 Apr 2011; revised 2 Jul 2011; accepted 2 Jul 2011; published 12 Jul 2011

local phase within the beam by over 2π radian for radiation within the specified wavelength range. Grayscale computer generated holograms CGHs were displayed on the SLM's LCD via a digital visual interface DVI connection. Phase modulated beams from the SLM in the first diffraction order were reflected back onto the SLM where they were analyzed by the second half of the hologram. Power measurements were obtained using a photodiode power meter head (Orphir PD300-UV) having a spectral response of 200 nm to 1100 nm.

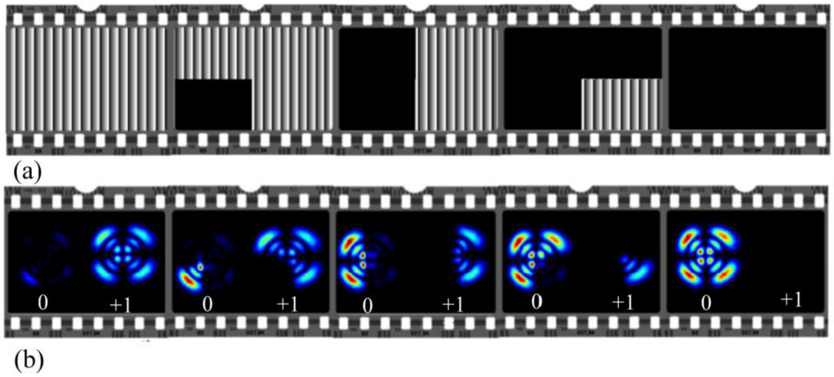

Fig. 5. Intensity profiles of a $LG^{o}_{2,2}$ beam being azimuthally knife-edged. (a) This sequence of frames shows the holograms used to perform an angular knife-edge measurement with an angular step size of 90 degrees. (b) CCD images of radiation from a He-Ne source after passing through the corresponding grating in sequence (a). Each frame shows both the zero and first diffraction orders. As the area of constant phase (denoted by the blackened areas in (a)) increases, the corresponding local radiation in the first diffraction order is directed into the zero order until the radiation is gone.

The knife-edge data, shown in this work, is the result of integrating the spatial intensity profile by a power meter. To qualitatively illustrate the performance of the holographic knife-edge, images of the zero and first orders for an odd $LG^{o}_{2,2}$ beam produced with He-Ne wavelengths were recorded with a CCD camera. In Fig. 5, the knife-edge measurement was performed in an azimuthal direction. For illustration purposes, the angular step size was taken to be 90 degrees. The upper sequence Fig. 5(a) is a representation of holograms with angular knife-edge angles of 0, 90, 180, 270 and 360 degrees. This grating was blazed according to optimal conditions shown in Fig. 2. In the lower sequence, the images were taken with a CCD camera and show the intensity profiles in the zero and first orders. In the first frame, the grating is that of a regular blazed grating showing only a fraction of the power in the zero order compared to that in the first order. When a section of the holographic grating is set to a constant phase, this part of the beam will be directed into the zero order. It can be seen that the radiation in the first diffraction order, corresponding to this region, has been removed and appears in that region of the zero order. In the remaining frames of the sequence, the azimuthal knife-edge is increased in steps of 90 degrees, and with each step a portion of the optical mode is redirected into the zero order until the beam in the first diffraction order vanishes, and the grating becomes that of a constant phase plate.

5. Knife-Edge Equations for the Hermite-Gaussian Beams

In contrast to theoretically obtained knife-edge curves, experimental measurements yield data that is not always monotonically increasing or decreasing. Due to noise such as laser fluctuations, differentiation of experimental data may lead to noisy and/or unphysical results. For this reason, it is advantageous to fit experimentally obtained data with theoretical curves in which one can extract quantitative beam parameters needed to characterize the beam. This is commonly practiced by experimentalists when performing knife-edge measurements for

Gaussian beams [20]. For more complex beams such as that shown in Fig. 5, one can readily determine the relative power and spatial extent within each modal lobe by observing the plateau regions of a knife-edge measurement of the beam.

The Hermite-Gaussian modes are eigensolutions of the paraxial wave equation in Cartesian coordinates. Because of their rectangular geometry, a straight-edge presents a natural choice for characterizing such beams. Theoretical knife-edge curves for the Hermite-Gaussian modes have been presented in the literature [21]. The authors in this work, however, stated that they were unable to obtain a general analytical form for the knife-edge equations and therefore presented numerical solutions. Using numerical solutions complicates fitting routines when obtaining beam parameters from experimental data. For this reason, we present the derivation of these analytical solutions. The electric field amplitude of the Hermite-Gaussian modes is,

$$E_{\mathrm{HG}_{n,m}} = N_{n.m} E_0 \frac{w_0}{w} \mathrm{H}_n\left(\frac{\sqrt{2}x}{w(z)}\right) \mathrm{H}_m\left(\frac{\sqrt{2}y}{w(z)}\right) e^{-(r^2/w^2)} e^{i\left[\frac{kr^2}{2R}-(n+m+1)\varphi_{\mathrm{G}}+kz\right]}. \tag{2}$$

Here w_0, $w(z)$ and $z_0 = \pi w_0^2/\lambda$ are the beam waist and size and Rayleigh range respectively; $\varphi_{\mathrm{G}}(z) = \arctan(z/z_0)$ is the Gouy phase, $R(z) = z + z_0^2/z$ is the radius of curvature, and H_n are the Hermite Polynomials in which n and m are mode numbers. The normalization factor $N_{n,m} = \sqrt{1/(2^{n+m} n! m!)}$ is chosen such that the integral of $I_{\mathrm{HG}_{0,0}} = \left|E_{\mathrm{HG}_{0,0}}\right|^2$ over all space leads to $P_0 = \pi I_0 w_0^2/2$. The measured position-dependent power is found from,

$$P_{\mathrm{HG}_n}(x) = \int_x^{\infty}\int_{-\infty}^{\infty} I_{\mathrm{HG}_{n,m}}(x', y', z')dx'dy'. \tag{3}$$

A similar expression can be written for a knife-edge measurement performed in the y direction; however, the functional form of the solution is the same as that found for the x direction. To find the power as a function of the knife-edge position, it is advantageous to make the following substitutions $\xi = \sqrt{2}x/w$ and $\eta = \sqrt{2}y/w$ to Eq. (2) prior to integration,

$$P_{\mathrm{HG}_n}(x) = N_{n.m}^2 I_0 w_0^2 \frac{1}{2}\int_{-\infty}^{\infty} \mathrm{H}_m^2(\eta) e^{-\eta^2} d\eta \int_x^{\infty} \mathrm{H}_n^2(\xi) e^{-\xi^2} d\xi = N_{n.m}^2 I_0 w_0^2 \frac{1}{2} I_\eta I_\xi(x). \tag{4}$$

Here I_η is the integral over the y direction, and its solution is well-known from the normalization of H_m to be $I_\eta = m! 2^m \sqrt{\pi}$. Because the Hermite polynomials are indexed by a single mode number and because the position-dependent power depends on the integral I_ξ, the knife-edge measurement over a single coordinate direction depends only on the mode number in that direction. To solve the I_ξ integral, we use Rodrigues formula $H_n(\xi) = (-1)^n e^{\xi^2} d^n(e^{-\xi^2})/d\xi$ for the Hermite Polynomials,

$$I_\xi = (-1)^n \int_x^{\infty} \mathrm{H}_n(\xi) \frac{d^n}{d\xi^n}\left(e^{-\xi^2}\right) d\xi. \tag{5}$$

Integrating by parts one time and using the Appell sequence $H_n' = 2nH_{n-1}$, where $n = 1, 2, 3, \ldots$, Eq. (5) becomes,

$$I_\xi = (-1)^n \left[-\mathrm{H}_n(\xi) \frac{d^{n-1}}{d\xi^{n-1}}\left(e^{-\xi^2}\right) - 2n\int_x^{\infty} \mathrm{H}_{n-1}(\xi) \frac{d^{n-1}}{d\xi^{n-1}}\left(e^{-\xi^2}\right) d\xi \right]. \tag{6}$$

Rodrigues formula can be used once again to remove the derivative in the first term, showing how the first term in a sequence of terms is found,

#146202 - $15.00 USD Received 19 Apr 2011; revised 2 Jul 2011; accepted 2 Jul 2011; published 12 Jul 2011

$$I_{\xi} = (-1)^{n}\left[(-1)^{n} e^{-\xi^{2}} H_{n-1}(\xi)\mathrm{H}_{n}(\xi) - 2n\int_{x}^{\infty}\mathrm{H}_{n-1}(\xi)\frac{d^{n-1}}{d\xi^{n-1}}\left(e^{-\xi^{2}}\right)d\xi\right]. \qquad (7)$$

Continuing in this fashion n times, the position-dependent power can be obtained. Upon restoring the contribution from the y-integral, the measured power from the knife-edge experiment reduces to the finite sum,

$$P_{\mathrm{HG}_n}(x) = \frac{1}{2}P_0\left\{e^{-\xi^{2}}\sqrt{\frac{1}{\pi}}\sum_{k=1}^{n}\frac{2^{k-n}}{(n+1-k)!}H_{n-k+1}(\xi)H_{n-k}(\xi) + \mathrm{erfc}(\xi)\right\}. \qquad (8)$$

Here $\xi(x) = \sqrt{2}x/w$, and the last term is the complimentary error function $\mathrm{erfc}(\xi) = 1 - \mathrm{erf}(\xi)$. The total power P_0 is that from the integration over all space. From Eq. (8), it can be seen that the position-dependent power is independent of the mode number governing the y-dependent part of the beam profile. When $n = 0$, the term in Eq. (8) containing the sum vanishes, and Eq. (8) reduces to the well-known knife-edge formula for a Gaussian beam $P_{\mathrm{HG}_n}(x) = P_0\mathrm{erfc}(\xi)/2$.

In Figs. 6(a-b), knife-edge measurements of higher-order Hermite-Gaussian beam are shown along with fit-curves based on Eq. (8). The squares (circles) are from knife-edge measurements in the $x(y)$ direction. In the data, some curves can be seen to have plateaus. These plateaus correspond to nodes of the beam, and are equal in number to the mode numbers. In the x knife-edge, the number of plateaus corresponds to mode number n in Eq. (2), and in the y direction to mode number m. The ratio of the powers between the plateaus gives an indication of the symmetry of the modal structure. The red curves were obtained by fitting to the data using Eq. (8). In general good agreement is found between experiment and theory. Since the beam size $w(z)$ is independent of the mode numbers, the $\mathrm{HG}_{2,2}$ mode has the same beam size as that of the $\mathrm{HG}_{0,0}$ mode. The beam size in the x and y directions was found to ~52 pixels or ~1 mm.

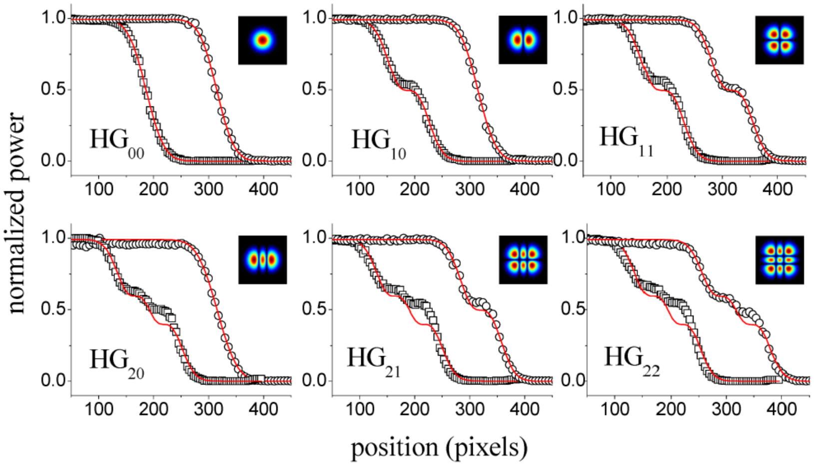

Fig. 6. Cartesian knife-edge measurements of the Hermite-Gaussian modes. The modality of each mode is given as the label of the panel. The black opened squares are data taken from knife-edge measurements in the x direction and the black opened circles are that in the y direction. The number of plateaus is equal to the mode number. The red curves were obtained by fitting the data with theoretical curves presented in the text. From this fit the beam size was determined.

#146202 - $15.00 USD Received 19 Apr 2011; revised 2 Jul 2011; accepted 2 Jul 2011; published 12 Jul 2011

6. Knife-Edge Equations for the Laguerre-Gaussian Beams

Similar to the knife-edge measurements for the Hermite-Gaussian modes, there exist preferable knife-edge geometries when considering beams in cylindrical polar coordinates: azimuthal and radial. The radial knife edge measurement is similar to closing an iris down on a beam. Less familiar is the azimuthal knife edge, which mechanically would be similar to the opening of a folding fan. The azimuthal knife-edge is a prime example of a knife edge geometry which is difficult to mechanically reproduce. An example of a more difficult knife-edge is that used for the Ince-Guassian beams. The azimuthal and radial knife-edge analogues for the Ince-Gaussians beams correspond to the mechanically difficult to reproduce hyperbola and ellipses—these geometries; however, are readily produced using computers.

The radial-knife equation is found in a similar form to that carried out for the Hermite-Gaussian knife-edge equations. The electric field of the Laguerre-Gaussian beam is

$$E_{\mathrm{LG}_{l,p}} = N_{l.p} E_0 \frac{w_0}{w} \left(\frac{\sqrt{2} r}{w(z)} \right)^l L_p^l \left(\frac{2r^2}{w^2(z)} \right) e^{-(r^2/w^2)} e^{il\theta} e^{i\left[\frac{kr^2}{2R} - (2p+l+1)\varphi_G + kz \right]}. \tag{9}$$

The normalization factor $N_{l,p}$ is chosen such that the integral of $I_{\mathrm{LG}} = |E_{\mathrm{LG}}|^2$ over all space leads to $P_0 = \pi I_0 w_0^2 / 2$. The measured position-dependent power is found from the volume integration of the intensity,

$$P_{\mathrm{LG}}(r) = \int_0^r \int_0^{2\pi} I_{\mathrm{LG}}(r') r' dr' d\theta'. \tag{10}$$

To find the power as a function of the knife-edge position, it is advantageous to make the following substitution $\xi = 2r^2 / w^2$ to Eq. (9),

$$P_{\mathrm{LG}_{l,p}}(r) = \frac{\pi}{2} I_0 w_0^2 N_{l.p}^2 \int_0^r \xi^l L_p^l(\xi) L_p^l(\xi) e^{-\xi} d\xi = \frac{\pi}{2} I_0 w_0^2 N_{l.p}^2 I_\xi(r). \tag{11}$$

The solution to the integral $I_\xi(r)$ from zero to infinity is well-known from normalization of the associated Laguerre polynomials to be $(p+l)!/p!$. Unlike the HG$_{n,m}$ modes, the position-dependent power for the radial knife-edge of the LG modes depends on both the radial p and azimuthal ℓ mode numbers. To solve for the integral, we use Rodrigues formula $L_p^l(\xi) = (\xi^{-l} e^{\xi} / p!) d^p (\xi^{p+l} e^{-\xi}) / d\xi^p$ for one of the Laguerre Polynomials,

$$I_\xi = \frac{1}{p!} \int_0^r \frac{d^p}{d\xi^p} (\xi^{p+l} e^{-\xi}) L_p^l(\xi) d\xi. \tag{12}$$

Integrating by parts one time and using the differential relation $L_p^{l}{}' = -L_{p-1}^{l+1}$,

$$I_\xi = \frac{1}{p!} \left[L_p^l(\xi) \frac{d^{p-1}}{d\xi^{p-1}} (\xi^{p+l} e^{-\xi}) - \int_0^r L_p^{l}{}'(\xi) \frac{d^{p-}}{d\xi^{p-1}} (\xi^{p+l} e^{-\xi}) d\xi \right]. \tag{13}$$

Rodrigues formula can be used once again to remove the derivative in the first term,

$$I_\xi = \frac{1}{p!} \left[(p-1)! \xi^{l+1} e^{-\xi} L_p^l(\xi) L_{p-1}^{l+1}(\xi) - (-1) \int_0^r L_{p-1}^{l+1}(\xi) \frac{d^{p-1}}{d\xi^{p-1}} (\xi^{p+l} e^{-\xi}) d\xi \right]. \tag{14}$$

Continuing in this fashion p times gives the position-dependent power in terms of a finite sum,

$$P_{\mathrm{LG}_p^l}(r)=P_0\left\{e^{-\xi}\sum_{k=1}^{p}(p-k)!\,\xi^{l+k}L_{p-k}^{l+k}(\xi)L_{p-k+1}^{l+k-1}(\xi)+\gamma(p+l+1,\xi)\right\}. \qquad (15)$$

Here $\xi = 2r^2/w^2$ and the last term is the incomplete gamma function. From Eq. (15), it can be shown that when $p,\ell = 0$, Eq. (15) returns the radial knife-edge formula for a Gaussian beam $P_{\mathrm{LG}}(r)=P_0\left(1-\exp(-2r^2/w^2)\right)$. In contrast to the knife-edge curves found for the Hermite-Gaussian beams, the radial knife-edge curves of the LG beams depend on both the radial and azimuthal mode numbers.

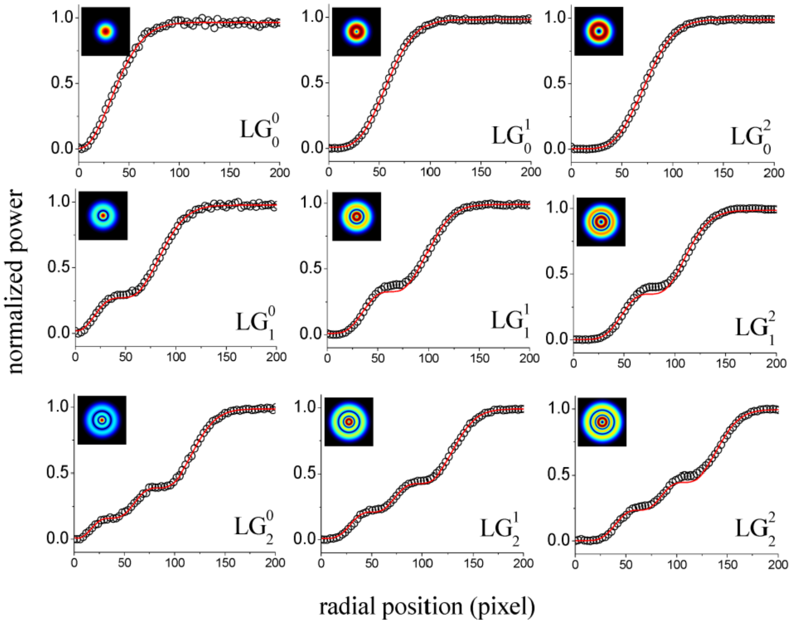

Fig. 7. Radial knife-edge measurements for an assortment of helical Laguerre-Gaussian beams. The number of plateaus is equal to the radial mode number *p*. The waist of the beams can be determined by fitting the data to the theoretical equations given in the text. The fits are shown by the solid red curves. Unlike the HG beams, the radial knife-edge measurements depend on both radial and azimuthal mode numbers *p* and *l*. The dependence of the curve on the azimuthal mode number can be seen by the size of the initial plateau increasing from the leftmost column to the rightmost column

Figure 7 shows radial knife-edge measurements of nine LG_p^ℓ beams. Their modalities are denoted in the figures. Going from left to right in each column, it can be seen that the initial plateau (corresponding to the intensity profile near the vortex core) becomes increasingly extended with increasing angular mode number ℓ. This is expected since the peak position of the doughnut beam increases with angular mode number according to $r = w\sqrt{\ell/2}$.

Comparatively, the azimuthal knife-edge for the LG beams requires little calculational effort. In addition to the well-known helical LG beams, there also exist the even and odd solutions of the paraxial wave equation denoted by $\mathrm{LG}_{p,\ell}^{e}$ and $\mathrm{LG}_{p,\ell}^{o}$ respectively. Helical LG beams do not show parity in the azimuthal coordinate as do the even and odd solutions [10]. Because of this, all knife-edge curves in the azimuthal direction for the helical LG

Received 19 Apr 2011; revised 2 Jul 2011; accepted 2 Jul 2011; published 12 Jul 2011

beams will be identical and equal to $P_{\mathrm{LG}_p^\ell}(\theta)=P_0(1-\theta/2\pi)$ for all mode numbers p and ℓ. For the even and odd LG modes, which are related by a rotation of 90 degrees, the knife-edge curves are found from the integrals to be,

$$P_{\mathrm{LG}}(\theta)=P_0\left\{1-\frac{\theta}{2\pi}\left[1\pm\frac{\sin(2l\theta)}{2l\theta}\right]\right\}, \tag{16}$$

where +(−) stands for the even (odd) LG mode. Since $\mathrm{LG}^{o}_{p,\ell}$ contains $\sin(\ell\theta)$ Eq. (16) does not hold for the odd solutions when $\ell=0$. However, the even solutions contain $\cos(\ell\theta)$ so when $\ell=0$ Eq. (16) reduces to $P_{\mathrm{LG}}(\theta)=P_0(1-\theta/2\pi)$. Figure 8 shows the results for the azimuthal knife edge. The odd LG beams have been shown because they are related to the even LG beams by a rotation of 90 degrees. Unlike the radial knife-edge equation for the LG beams, the azimuthal knife-edge equation depends only on the azimuthal mode number ℓ and by itself cannot be used to obtain information about the radial structure of the beam such as the waist. However, this measurement can be used as an indication of the azimuthal purity of the beam.

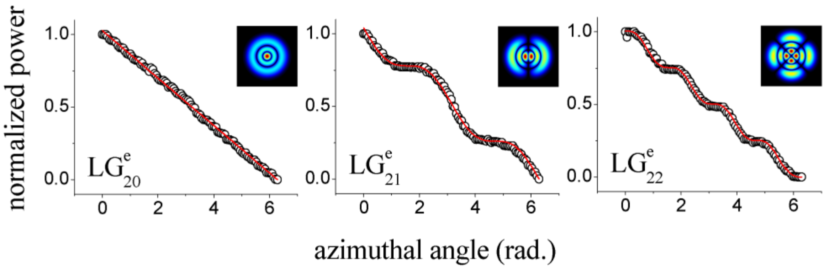

Fig. 8. Angular knife-edge measurements for an assortment of even LG beams having modalities as indicated. The number of plateaus is equal to twice the angular mode number $2l$. The waist of the beam cannot be determined from an angular knife-edge measurement, but this measurement can give an indication of the quality of the modal lobes.

7. Tomographic Reconstruction

We conclude this work with experimental results on the tomographic reconstruction of femtosecond $\mathrm{LG}_{p=1}^{\ell=1}$ optical modes. Even though we have chosen a known optical beam, it is important to note that this reconstruction can be applied to optical beams having an arbitrarily-shaped intensity profile. There exist techniques to tomographically reconstruct optical beam using knife-edge methods [22,23]. We reconstruct beams by using two orthogonal knife-edge measurements, i.e., one along the x direction and the other along the y direction were taken by stepping the first knife-edge by a single step, completely knife-edging with the second knife-edge and then stepping the first knife another step and so on until the process is completed. For convenience, we have chosen Cartesian knife-edging, but in principle other geometries are possible i.e., the radial and azimuthal knife-edge measurements of polar coordinates. In general, the measured power from a double-knife-edge procedure has the form of Eq. (3) with integration limits $(-\infty,x]$ and $(-\infty,y]$, and arbitrary intensity profile $I(x,y)$. To reconstruct the intensity profile from the measured data all that is needed is the double derivative of the power $\partial^2 P/\partial x\partial y=I(x,y)$.

Figures 9(a,c) shows raw double-knife-edge data for a broadband $\mathrm{LG}_{p=1}^{\ell=1}$ beam compensated and uncompensated for angular dispersion, which was achieved by using a

Received 19 Apr 2011; revised 2 Jul 2011; accepted 2 Jul 2011; published 12 Jul 2011

concave mirror $f = 100\,\text{cm}$ and a flat mirror as the folding mirror in the folded-2f setup. The resolution in the x and y directions is $\sim 30\,\mu\text{m}$ and $\sim 40\,\mu\text{m}$, respectively. Figures 9(b,d) are the tomographically reconstructed images according to our method. As mentioned previously, taking the derivative of experimental data can lead to noise in the resulting data.

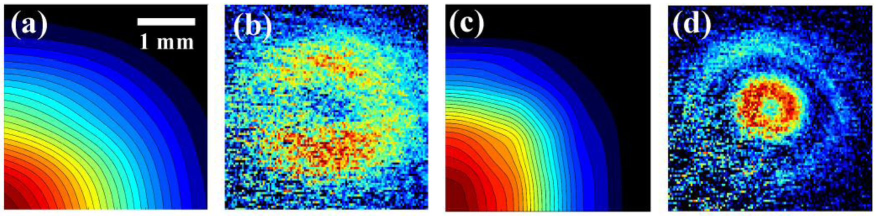

Fig. 9. Tomographic reconstruction of a femtosecond $\text{LG}_{p=1}^{\ell=1}$ beam in a folded-2f setup. All images are 200-by-200 pixels and have the same vertical and horizontal scaling. The dimension of the images is given by the scale in panel (a). (a, c) Raw double-knife-edge data recorded by stepping a knife-edge in one direction (i.e., x) by a single step, completing a full knife-edge in the other direction (i.e., y), and repeating this process until finished. The raw data shown in panel (a) is that obtained by not correcting for angular dispersion in the folded-2f setup, while that in panel (c) has been corrected. Panels (b) and (d) were obtained by taking the partial derivatives (see text) of the measured double-knife-edge power.

This was encountered when we reconstructed the beam images, and as a result, the raw data was sent through a mean filter before derivatives of the data were taken. As expected, the uncompensated beam exhibits a "blurring" in the dispersion plane similar to that shown in [10], while the compensated beam appears more "crisp" [13].

8. Conclusions

In summary we have demonstrated a beam analysis method based on a holographic knife-edge. Experimental results of the measured power from both holographic and mechanical knife-edge methods showed good agreement with each other. By using the same method to that used to holographically knife-edge (phase-amplitude encoding), high fidelity HG and LG modes were produced. To analyze these modes, we derived theoretical knife-edge equations to fit to the measured data. From the derived equations we were able to determine beam characteristics such as the waist and the distribution of intensities between the modal lobes. All measured data showed good agreement with the theoretically predicted curves. In principle, the method outlined here can be used to create virtually any desired shape for the characterization of optical beams. Finally, we used this method to tomographically reconstruct, in situ, a broadband optical beam in a folded-2f setup.

Acknowledgments

This work was partially supported by the Robert A. Welch Foundation (grant No. A1546), the National Science Foundation (NSF) (grants Nos. 0722800 and 0555568), the Qatar National Research Fund (grant NPRP30-6-7-35), and the United States Air Force Office of Scientific Research (USAFOSR) (grant FA9550-07-1-0069).

#146202 - $15.00 USD Received 19 Apr 2011; revised 2 Jul 2011; accepted 2 Jul 2011; published 12 Jul 2011

APPENDIX E

White-light generation using spatially-structured beams of femtosecond radiation

This journal article is reprinted with permission from The Optical Society. This journal article can be found at http://dx.doi.org/10.1364/OE.20.013337.

White-light generation using spatially-structured beams of femtosecond radiation

N. Kaya,[1,*] J. Strohaber,[1] A. A. Kolomenskii,[1] G. Kaya,[1] H. Schroeder,[2] and H. A. Schuessler,[1]

[1]*Department of Physics, Texas A&M University, College Station, TX 77843-4242, USA*
[2]*Max-Planck-Institut für Quantumoptik,Hans-Kopfermann-Strasse 1, DE-85748 Garching, Germany*
[*]*necati@physics.tamu.edu*

Abstract: We studied white-light generation in water using spatially-structured beams of femtosecond radiation. By changing the transverse spatial phase of an initial Gaussian beam with a 1D spatial light modulator to that of an Hermite-Gaussian ($HG_{n,m}$) mode, we were able to generate beams exhibiting phase discontinuities and steeper intensity gradients. When the spatial phase of an initial Gaussian beam (showing no significant white-light generation) was changed to that of a HG_{01}, or HG_{11} mode, significant amounts of white-light were produced. Because self-focusing is known to play an important role in white-light generation, the self-focusing lengths of the resulting transverse intensity profiles were used to qualitatively explain this production. Distributions of the laser intensity for beams having step-wise spatial phase variations were modeled using the Fresnel-Kirchhoff integral in the Fresnel approximation and found to be in good agreement with experiment.

OCIS codes: (190.5530) Pulse propagation and temporal solitons; (320.7110) Ultrafast nonlinear optics; (190.5940) Self-action effects.

References and links

1. R. R. Alfano and S. L. Shapiro, "Emission in the region 4000 to 7000 Å via four-photon coupling in glass," Phys. Rev. Lett. **24**(11), 584–587 (1970).
2. R. R. Alfano, *The Supercontinuum Laser Source: Fundamentals with Updated References*, 2nd ed. (Springer Science + Business Media, Inc., 2006).
3. N. Bloembergen, "The influence of electron plasma formation on superbroadening in light filaments," Opt. Commun. **8**(4), 285–288 (1973).
4. W. Lee Smith, P. Liu, and N. Bloembergen, "Superbroadening in H2O and D2O by self-focused picosecond pulses from a YAlG: Nd laser," Phys. Rev. A **15**(6), 2396–2403 (1977).
5. R. L. Fork, C. V. Shank, C. Hirlimann, R. Yen, and W. J. Tomlinson, "Femtosecond white-light continuum pulses," Opt. Lett. **8**(1), 1–3 (1983).
6. G. Yang and Y. R. Shen, "Spectral broadening of ultrashort pulses in a nonlinear medium," Opt. Lett. **9**(11), 510–512 (1984).
7. P. B. Corkum, C. Rolland, and T. Srinivasan-Rao, "Supercontinuum generation in gases," Phys. Rev. Lett. **57**(18), 2268–2271 (1986).
8. P. B. Corkum and C. Rolland, "Femtosecond continua produced in gases," IEEE J. Quantum Electron. **25**(12), 2634–2639 (1989).
9. F. A. Ilkov, L. Sh. Ilkova, and S. L. Chin, "Supercontinuum generation versus optical breakdown in CO(2) gas," Opt. Lett. **18**(9), 681–683 (1993).
10. V. François, F. A. Ilkov, and S. L. Chin, "Experimental study of the supercontinuum spectral width evolution in CO2 gas," Opt. Commun. **99**(3-4), 241–246 (1993).
11. G. S. He, G. C. Xu, Y. Cui, and P. N. Prasad, "Difference of spectral superbroadening behavior in Kerr-type and non-Kerr-type liquids pumped with ultrashort laser pulses," Appl. Opt. **32**(24), 4507–4512 (1993).
12. A. Brodeur, F. A. Ilkov, and S. L. Chin, "Beam filamentation and the white light continuum divergence," Opt. Commun. **129**(3-4), 193–198 (1996).
13. J. H. Glownia, J. Misewich, and P. P. Sorokin, "Ultrafast ultraviolet pump-probe apparatus," J. Opt. Soc. Am. B **3**(11), 1573–1579 (1986).

#167058 - $15.00 USD Received 18 Apr 2012; revised 19 May 2012; accepted 19 May 2012; published 30 May 2012

14. S. Cussat-Blanc, A. Ivanov, D. Lupinski, and E. Freysz, "KTiOPO4, KTiOAsO4, and KNbO3 crystals for mid-infrared femtosecond optical parametric amplifiers: analysis and comparison," Appl. Phys. B **70**(S1), S247–S252 (2000).
15. T. Kobayashi and A. Shirakawa, "Tunable visible and near-infrared pulse generator in a 5 fs regime," Appl. Phys. B **70**(S1), S239–S246 (2000).
16. T. Kobayashi, T. Saito, and H. Ohtani, "Real-time spectroscopy of transition states in bacteriorhodopsin during retinal isomerization," Nature **414**(6863), 531–534 (2001).
17. P.-L. Hsiung, Y. Chen, T. H. Ko, J. G. Fujimoto, C. J. S. de Matos, S. V. Popov, J. R. Taylor, and V. P. Gapontsev, "Optical coherence tomography using a continuous-wave, high-power, Raman continuum light source," Opt. Express **12**(22), 5287–5295 (2004).
18. E. Hugonnot, M. Somekh, D. Villate, F. Salin, and E. Freysz, "Optical parametric chirped pulse amplification and spectral shaping of a continuum generated in a photonic band gap fiber," Opt. Express **12**(11), 2397–2403 (2004).
19. K. R. Wilson and V. V. Yakovlev, "Ultrafast rainbow: tunable ultrashort pulses from a solid-state kilohertz system," J. Opt. Soc. Am. B **14**(2), 444–448 (1997).
20. E. N. Glezer, Y. Siegal, L. Huang, and E. Mazur, "Laser-induced band-gap collapse in GaAs," Phys. Rev. B Condens. Matter **51**(11), 6959–6970 (1995).
21. M. Wittmann and A. Penzkofer, "Spectral superbroadening of femtosecond laser pulses," Opt. Commun. **126**(4-6), 308–317 (1996).
22. J. K. Ranka, R. W. Schirmer, and A. L. Gaeta, "Observation of Pulse Splitting in Nonlinear Dispersive Media," Phys. Rev. Lett. **77**(18), 3783–3786 (1996).
23. A. Brodeur and S. L. Chin, "Band-gap dependence of the ultrafast white light continuum," Phys. Rev. Lett. **80**(20), 4406–4409 (1998).
24. A. Brodeur and S. L. Chin, "Ultrafast white-light continuum generation and self-focusing in transparent condensed media," J. Opt. Soc. Am. B **16**(4), 637–650 (1999).
25. A. Couairon and A. Mysyrowicz, "Femtosecond filamentation in transparent media," Phys. Rep. **441**(2-4), 47–189 (2007).
26. J. H. Marburger, "Self-focusing: theory," Prog. Quantum Electron. **4**, 35–110 (1975).
27. A. Dharmadhikari, F. Rajgara, D. Mathur, H. Schroeder, and J. Liu, "Efficient broadband emission from condensed media irradiated by low-intensity, unfocused, ultrashort laser light," Opt. Express **13**(21), 8555–8564 (2005).
28. H. Schroeder, J. Liu, and S. Chin, "From random to controlled small-scale filamentation in water," Opt. Express **12**(20), 4768–4774 (2004).
29. L. Allen, M. W. Beijersbergen, R. J. C. Spreeuw, and J. P. Woerdman, "Orbital angular momentum of light and the transformation of Laguerre-Gaussian laser modes," Phys. Rev. A **45**(11), 8185–8189 (1992).
30. A. E. Siegman, *Lasers* (University Science Books, 1986), p. 645.
31. J. Strohaber, G. Kaya, N. Kaya, N. Hart, A. A. Kolomenskii, G. G. Paulus, and H. A. Schuessler, "In situ tomography of femtosecond optical beams with a holographic knife-edge," Opt. Express **19**(15), 14321–14334 (2011).
32. J. Peatross and M. Ware, "Physics of Light and Optics," 2011 edition, available at optics.byu.edu.
33. K. Cook, R. McGeorge, A. K. Kar, M. R. Taghizadeh, and R. A. Lamb, "Coherent array of white-light continuum filaments produced by diffractive microlenses," Appl. Phys. Lett. **86**(2), 021105 (2005).

1. Introduction

An ultrashort pulse propagated through a transparent medium can be transformed into a white-light continuum which can extend from the ultraviolet to the infraredand, and this well-known phenomenon occurs in a wide variety of media [1–12]. The ultrafast white-light generation is useful for various applications such as femtosecond time-resolved spectroscopy, optical pulse compression for the generation of ultrashort pulses, or as a seed pulse for optical parametric amplifiers, and biomedical applications [2,13–20].

Self-phase modulation [5–7], self-steepening [21], and parametric four-photon mixing [6] are some of the mechanisms that have been invoked to explain the white-light generation. However, the primary process responsible for the phenomena of white-light generation is self-focusing, which causes the pulse to compress in space, resulting in a corresponding increase in the peak intensity [7]. When a threshold peak power for a white-light continuum P_{th}^{wl} is just above the input pulse power, the beam transformed into white-light continuum appears to the eye as a white spot. As the input peak power is increased to a few P_{th}^{wl}, a colorful ring pattern appears surrounding the central spot. The resulting beam appears to the eye as a white light disk surrounded by a distinct, concentric, rainbow-like pattern. Experiments have shown that

#167058 - $15.00 USD Received 18 Apr 2012; revised 19 May 2012; accepted 19 May 2012; published 30 May 2012

the threshold power P_{th}^{wl} for white-light generation coincides with the calculated critical power P_{crit} for self-focusing [4,7–10,22]. Experiments conducted by Brodeur and Chin [23,24] have confirmed that white-light generation is triggered by self-focusing. Comparison of the critical power for self-focusing P_{crit} and for white-light continuum P_{th}^{wl} in several media shows that $P_{crit} \simeq P_{th}^{wl}$ [24]. Therefore, it should then be noted that P_{crit} and P_{th}^{wl} are essentially equivalent.

Studies of white-light generation in liquids, which typically have nonlinear contributions to the refractive index about 10^3 times larger than that for gases, can reproduce many important features of the processes at much lower laser powers and on a much smaller scale under laboratory conditions [25]. According to Marburger's formula [26], it holds for the critical power of self-focusing

$$P_{crit} = 3.77 \frac{\lambda_0^2}{8\pi n_0 n_2} \qquad (1)$$

where $\lambda_0 = 800nm$, $n_0 = 1.33$, and $n_2 = 2\times10^{-16} cm^2/W$ [23] for water, and one obtains $P_{crit} = 3.6\,MW$. Here, λ_0 denotes the laser wavelength, n_0 is the linear refractive index of the medium, and n_2 is its nonlinear coefficient. The self-focusing length of the beam with a spatial Gaussian distribution of intensity at the input of the medium [26] is given by:

$$L_{sf} = \frac{0.734\pi n_0 a_0^{\,2}}{\lambda_0 \left[\left(\sqrt{P/P_{crit}} - 0.852 \right)^2 - 0.0219 \right]^{1/2}} \qquad (2)$$

where P is the beam power and a_0 is the radius of the beam profile at the 1/e level of intensity. The self-focusing length, L_{sf}, varies as a function of the beam radius, a_0, and the ratio of the peak power over the critical power for self-focusing, P/P_{crit}.

In the present paper we show that by changing the transverse spatial phase of an initial Gaussian beam to that of an Hermite-Gaussian ($HG_{n,m}$) mode, we were able to generate beams exhibiting phase discontinuities and steeper intensity gradients. The previous experiments emphasized that the locus of conical emission was controlled by local diffraction catastrophes produced by any kind of aperture [27,28]. In the present case the situation is much clearer. When the spatial phase of an initial Gaussian beam (showing no significant white-light generation) was changed to that of a HG_{01}, or HG_{11} mode, significant amounts of white-light were produced. The self-focusing lengths determined by the peak powers and radii of the lobes in the resulting transverse intensity profiles were used to qualitatively explain this production, because self-focusing is known to play an important role in white-light generation. Distributions of the laser intensity for beams having step-wise spatial phase variations were modeled using the Huygens-Fresnel-Kirchhoff diffraction formulation in the Fresnel approximation and were found to be in good agreement with experiment.

2. Experimental procedure

In the experiment, an 800nm Ti:sapphire laser system (Spitfire, Spectra Physics) with a typical power of about 1W and pulse duration ~50fs was employed. From Eq. (2), for constant beam power the self-focusing distance is proportional to the square of the beam size so decreasing the beam size decreases the self-focusing distance. Therefore, to shorten the length for white-light formation we reduced the beam size by using an optical telescope. For generating taylored phase variations we used a Spatial Light Modulator (SLM), Jenoptik SLM-S 640/12, which is a liquid crystal modulator with 640 stripe-shaped pixels and 12 bit

#167058 - $15.00 USD Received 18 Apr 2012; revised 19 May 2012; accepted 19 May 2012; published 30 May 2012

resolution to change the transverse spatial phase of an initial Gaussian beam to that of an $HG_{n,m}$ mode. Its active area is 63.7 mm x 7 mm, and the transmission for a wavelength range (430nm-800nm) is >75%. In the following the formation and recording of the resulting transverse intensity profiles together with their analytical form are presented. Subsequently the experiments of white-light generation of these beams are described.

2.1 Experimental formation of HG beams

HG modes are a family of stable transverse laser beam modes which are structured perpendicular to the propagation axis. These modes are approximate solutions of the wave equation, valid for weak focusing (paraxial approximation). The well-known normalized HG mode distributions are

$$\begin{aligned} E_{n_x,m_y}(x,y,z) = & \left(\frac{1}{2^{n_x+m_y} \pi n_x! m_y!} \right)^{1/2} \frac{1}{w_z} \\ & \times H_{n_x}(\frac{\sqrt{2}x}{w_z}) H_{m_y}(\frac{\sqrt{2}y}{w_z}) e^{-(r^2/w_z^2)} \\ & \times \exp i \left[\frac{kr^2}{2R_z} - (n_x+m_y+1)\phi_G(z) + kz \right]. \end{aligned} \tag{3}$$

where k, w_z, R_z, z_R, and H_n are the wave number, beam width, phase front curvature radius, Rayleigh range, and *n*th order Hermite polynomials, respectively. $\phi_G(z) = \arctan(z/z_R)$ is the Gouy phase [29–31].

The experimental setup to change the spatial phase of an initial Gaussian beam to that of a HG_{00}, HG_{01}, HG_{10}, or HG_{11} mode is shown in Fig. 1. HG beams were formed by using the SLM with a required phase mask. Since the SLM was used twice in the experiment to generate HG beams, the power incident on a cuvette with water (taking into account all optical losses) was reduced to 397mW. For the repetition rate of our laser system of 1 kHz and the pulse duration $\tau = 50 fs$ we obtain the input peak power of the laser pulse $P_{in} = 7.94GW$.

Since we used a 1D SLM, to generate the spatial phase of the HG_{11} the beam passed the mask twice, both times with the required horizontal polarization. The display of the SLM was divided into three parts with phases shifted by 180°, as is shown in the inset of Fig. 1, diagram (d). The center of the beam was positioned for the first pass at the border of the 1st and 2nd portions (pixel 118) of the mask, and for the second pass at the border of the 2nd and the 3rd portions (pixel 468) of the mask. Consequently, after two passes in the pairs of the left and right halves and the top and bottom halves of the beam the phases were shifted by 180°.

Although we are able to generate the spatial phases of HG_{00}, HG_{01} and HG_{10}, except for HG_{11}, without using the SLM twice, we used for all measurements the fixed geometry, utilized for the generation of HG_{11}, in order to have the same conditions for all HG beams. In this configuration, for obtaining the spatial phases of HG_{10} and HG_{01} beams the phases of the 1st (relative to the 2nd) and the 2nd (relative to the 3rd) portions of the mask were not changed. The liquid crystal phase masks to generate the spatial phases of HG_{00}, HG_{01}, HG_{10} and HG_{11} are shown as (a – d) in the inset of Fig. 1, respectively. Then, we recorded the images of the distribution of the laser intensity in HG beams by using a CCD camera with resolution 1392x1040 and pixel size 4.65 x4.65 at the position 1 (the entrance of the cuvette) in Fig. 1. Figure 2 demonstrates the distributions of the laser intensity in the HG_{00}, HG_{01}, HG_{10} and HG_{11} beams created with the phase masks (a-d) as shown in the inset of Fig. 1.

#167058 - $15.00 USD Received 18 Apr 2012; revised 19 May 2012; accepted 19 May 2012; published 30 May 2012

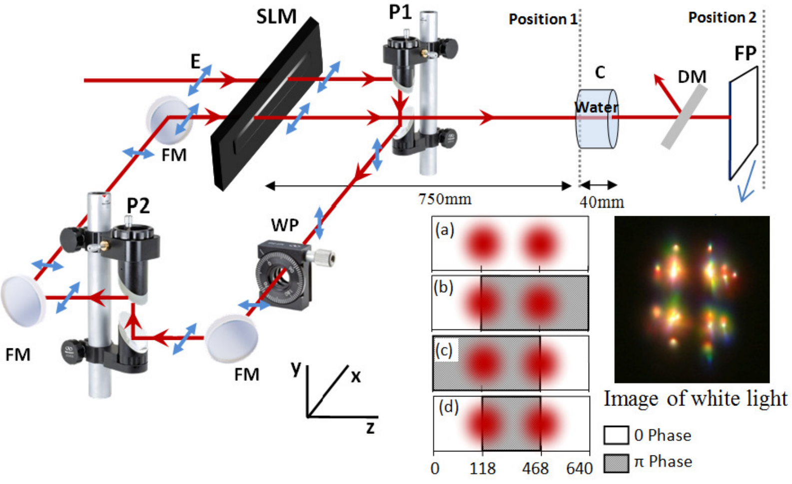

Fig. 1. Experimental setup to generate HG modes with the 1D SLM and for studies of white-light generation of HG beams in water. Laser radiation from the Ti:sapphire laser enters the setup from the left. Blue arrows (E) show the initial polarization of the beam and the changes of this polarization after the passage of the periscope P1 and a (λ/2) wave plate (WP). Other optical components used: P2-periscope to adjust the beam height, SLM - spatial light modulator, FM - folding mirror. Notice that in P1 the mirrors are rotated relative to each other in the horizontal plane by 90°, while in P2 the mirrors are parallel. The incident HG beam enters a 40mm long cuvette (C). A CCD camera for taking images is first placed at position 1 on the entrance of the cuvette to record the generated HG beam. Then the camera is placed at position 2 to record the generated white light on a frosted paper screen (FP) after the radiation of the pump beam is reflected by an 800nm dielectric mirror (DM). The colored picture of HG_{11} taken by a color digital camera at position 2 shows the strong white cores with colorful rings (conical emission) in the lower right inset. (a), (b), (c), and (d) present grey-scale encoded phase masks to create HG_{00}, HG_{01}, HG_{10} and HG_{11} beams, respectively.

The HG_{00} beam had an intensity distribution of the Gaussian with beam size w_{FWHM} = 1.93mm at a full width at half-maximum (FWHM). Using camera pixels, the value of w_{FWHM} is experimentally obtained from image of the HG_{00} beam (see panel (a) in Fig. 2) on the beam entrance of the cuvette. Because we modified only the phase within the initial Gaussian beam profile, the resulting HG modes are expected to be superposition of HG_{01}, HG_{10} and HG_{11} and higher modes. This can be seen in panels (b – d) in Fig. 2 by the appearance of side lobes.

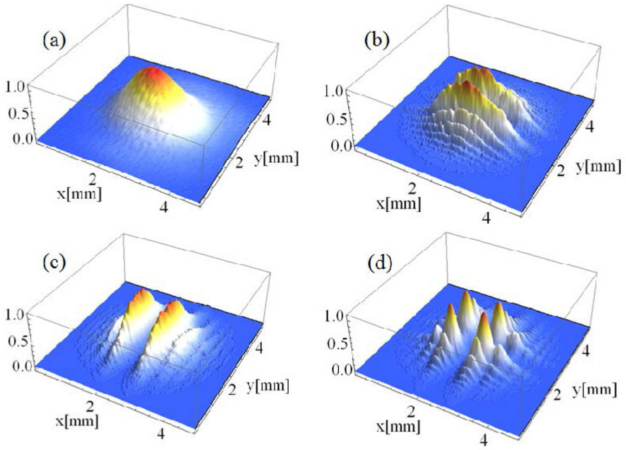

Fig. 2. The measured distributions of the laser intensity in the HG_{00}, HG_{01}, HG_{10} and HG_{11} beams. Each laser distribution has been peak normalized. HG beams in panels (a – d) are created with the phase masks (a – d) as shown in the inset of Fig. 1.

2.2 Calculations for HG modes: Apertures with phase changes

The analytical solutions of the distribution of the laser intensity in HG beams are obtained in the form of the diffraction integral by using the Fresnel approximation. In the Fresnel approximation [32], we have the expression

$$E(x,y,z=d) \cong -\frac{ie^{ikd}e^{i\frac{k}{2d}(x^2+y^2)}}{\lambda d}\iint\limits_{aperture} E(x',y',z=0)e^{i\frac{k}{2d}(x'^2+y'^2)}e^{-i\frac{k}{d}(xx'+yy')}dx'dy' \quad (4)$$

where $E(x',y',z=0)$ is the scalar amplitude of the initial beam at the position of the SLM, $k = 2\pi/\lambda$ is the wave number, λ is the wavelength of the beam, d is the distance in $\hat{z}$ direction after taking the changes of the phase on SLM. When we were generating the HG_{11} mode, there was a 20cm distance (Δd) between the 1st and 2nd passes. Because the distance Δd was much smaller than the Rayleigh range ($\Delta d << z_0$), we neglected the propagation of the beam over the distance Δd. The field before incidence on the SLM was assumed to be $E(x',y',z=0) = E_0 e^{-(x'^2+y'^2)/w_0^2}$ with beam size, w_0 ($w_0 = w_{FWHM}/\sqrt{2\ln 2}$). After the SLM, taking into account changes of the phase imposed by the SLM mask $\varphi(x',y')$, we obtain $E(x',y',z=0) = E_0 e^{-(x'^2+y'^2)/w_0^2} e^{i\varphi(x',y')}$. Consequently, we have the expression

$$E(x,y,z=d) \cong -\frac{ie^{ikd}e^{i\frac{k}{2d}(x^2+y^2)}}{\lambda d}\int_{-\infty}^{\infty}\int_{-\infty}^{\infty} E_0 e^{-\frac{x'^2+y'^2}{w_0^2}} e^{i\frac{k}{2d}(x'^2+y'^2)} e^{-i\frac{k}{d}(xx'+yy')} e^{i\varphi(x',y')}dx'dy'. \quad (5)$$

Since for HG modes, where the neighboring modal lobes are out of phase by π, we can factorize the phase factor as $e^{i\varphi(x',y')} = e^{i\varphi_x(x')}e^{i\varphi_y(y')}$, the integrals over x and y coordinates are independent. The expressions become completely defined after the phases for each HG mode are determined. As an example, the phases for HG_{11} mode for x and y directions were defined as

$$\varphi(x') = \begin{cases} \pi \rightarrow -\infty < x' < 0 \\ 0 \rightarrow 0 < x' < \infty \end{cases} \quad \text{and} \quad \varphi(y') = \begin{cases} 0 \rightarrow -\infty < y' < 0 \\ \pi \rightarrow 0 < y' < \infty \end{cases}. \tag{6}$$

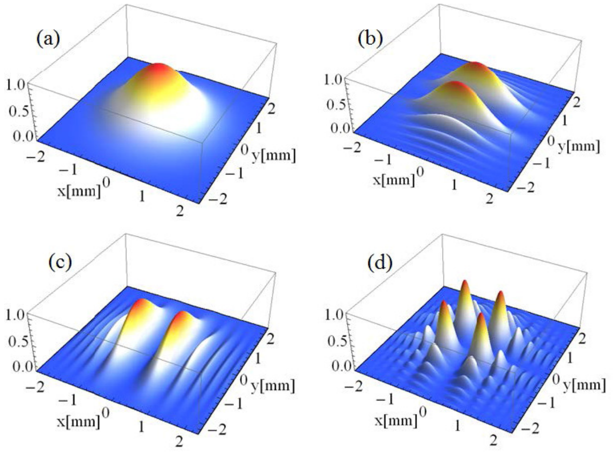

Fig. 3. The normalized distributions of the laser intensity in the cases of HG_{00}, HG_{01}, HG_{10} and HG_{11} beams calculated by the integrals with appropriate phase factors (Eqs. (5,6)).

For each mode, we calculated the integrals with appropriate phase factors, and presented them in Fig. 3. Because we modified only the phase within the initial Gaussian beam profile (panel (a) in Fig. 3), the resulting HG beams in panels (b – d) of Fig. 3 are expected to be the superposition of HG_{01}, HG_{10}, HG_{11} and higher modes similar to their experimental counterparts in panels (b – d) of Fig. 2. Numerical decomposition calculations for the modes produced in our setup have shown that for HG_{01} and HG_{10} phase configuration over 60% and for HG_{11} over 40% of the radiation sits in the desired mode; therefore we referred the resultant beams as HG_{01} and HG_{10}, HG_{11}. For the HG_{00} mode the phase is constant across the beam and the decomposition is 100% in the lowest order mode i.e., a Gaussian.

2.3 Experiments on white-light generation of HG beams in water

In order to generate white-light in water, the created HG_{01}, HG_{10}, or HG_{11} beams pass through a water cuvette of 40mm length placed at distance 750mm from the SLM as shown in Fig. 1. The images of white-light in water are projected on a frosted paper screen. A narrowband 800 nm mirror was inserted before the frosted paper to deflect the radiation of the pump beam and to obtain images of the generated white-light, avoiding also saturation of the CCD camera. The camera was placed at position 2 to record the white-light on the frosted paper screen.

Panels (a – d) in Fig. 4 show the images of the distribution of the measured light intensity on the CCD for all HG modes generated at the fixed geometry. No significant white-light formation took place in water for the HG_{00} mode (panel (a) in Fig. 4). However, if the phase masks, described above were imposed on the beam and the corresponding HG_{01}, HG_{10} and HG_{11} modes were generated, then the white-light generation took place. The alignment of white-light emissions closely follows the peaks of the intensity in the cross section of the respective laser beams (Fig. 2). For instance, for HG_{01} and HG_{10} modes the white-light emissions are formed along the crests of the intensity distribution, and for the HG_{11} mode the white-light emissions are concentrated in four lobes near the maxima of the intensity.

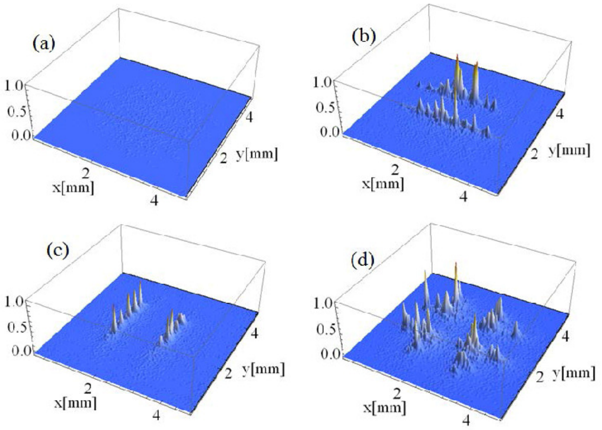

Fig. 4. The measured white-light intensity distributions on the CCD for all HG modes generated at the fixed geometry. Intensities are normalized respect to max white-light generation peak in HG_{11}.

3. Discussion

The generation of white-light that we observed can be justified in the following way. The resulting transverse intensity profiles of HG beams consist of several bright spots (intensity lobes), so we can assess strong white-light generation of the resulting HG beams by calculating the critical powers and self-focusing distances corresponding to these lobes. To trace these parameters for each of the observed lobes we presented each of the observed intensity distributions in top-view panels in Fig. 5.

The Gaussian beam (HG_{00}) on the entrance of the cuvette has a beam radius w_a = 1.16mm at 1/e value of the peak intensity (see panel (a) in Fig. 5). The value of w_a is obtained from the beam size w_{FWHM} = 1.93mm at FWHM by using the relation $w_a = w_{FWHM} / 2\sqrt{\ln 2}$. For the HG_{11} beam configuration the strong white-light generations are concentrated in four central lobes near the maxima of the intensity. We assume that the intensity distribution of each lobe can be approximated by a Gaussian profile (see panel (d) in Fig. 5). We measured the radius w_d = 0.17 w_a for one of the lobes of HG_{11} beam profile. For HG_{01} or HG_{10} beams the white-light generations are produced along the crests in the intensity distribution (see panels (b and c) in Fig. 5). One of the crests of HG_{01} has beam sizes at 1/e levels of 1.16mm and 0.19 mm in x and y directions of the crest respectively. One can count 5 well pronounced and partially overlapped intensity distribution peaks along x direction and choose one of the intense lobes on the one of the crests of HG_{01} as a Gaussian shaped sub-beam with a radius w_b = 0.19mm. Similarly, for HG_{10} the chosen Gaussian lobe radius is $w_c = w_b$. Again, the values of the beam radii refer to the 1/e levels of the lobes in the images. By using the radii and maximal intensities of the main lobes of HG_{01}, HG_{10} and HG_{11} beams, we calculate the corresponding input powers $P^a_{int} = 40.81P^b_{int} = 60.41P^d_{int}$ and $P^c_{int} \simeq P^b_{int}$.

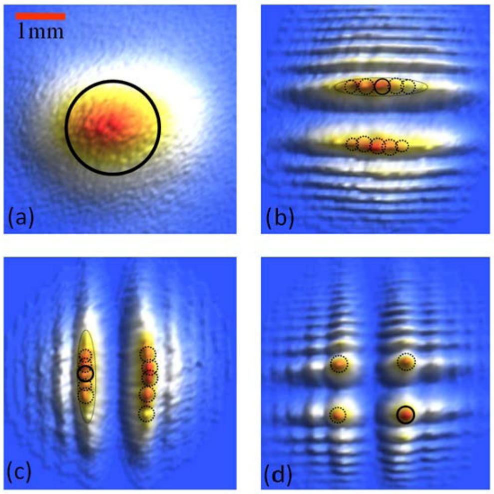

Fig. 5. The top view of the experimentally measured distributions of the laser intensity for the HG_{00}, HG_{01}, HG_{10} and HG_{11} beams from panels (a – d) of Fig. 2. The intensity lobes used for the calculation of the critical power and self-focusing distance of HG beams (main lobes) are shown with black solid circles in panels (a – d), drawn at FWHM values of the peak intensity; the dotted lines show the same for other peaks in the intensity distributions.

The critical power for water was calculated as 3.60MW by using Eq. (1). Inserting the input powers and radius of the lobes into Eq. (2), we obtained the self-focusing distances $L_{sf}^{a} = 11cm$, $L_{sf}^{b} \cong L_{sf}^{c} = 2.1cm$ and $L_{sf}^{d} = 2.6cm$ for the lobes with the highest intensities (main lobes), shown by solid circles in panels (a – d) in Fig. 5. We can see that for the Gaussian beam, no significant white-light in water can be expected, since the self-focusing distance $L_{sf}^{a} = 11cm$ of HG_{00} is longer than the cuvette length 40mm. In contrast, the self-focusing distances of the main lobes of HG_{01}, HG_{10} and HG_{11} beam are shorter than the cuvette length, so changing the beam configuration to HG_{01}, HG_{10} and HG_{11} beams resulted in the generation of white-light.

4. Conclusion

In this study, we presented how to generate the beams exhibiting phase discontinuities and steeper intensity gradients by imposing spatial phase masks on the initial Gaussian beam. Namely, HG_{01}, HG_{10} and HG_{11} and higher modes were produced by using a 1D spatial light modulator. The laser intensity distributions for the beams having step-wise spatial phase variations were described with the Fresnel-Kirchhoff integral in the Fresnel approximation and found to be in good agreement with experiment.

When the spatial phase of the Gaussian beam (showing no significant white-light generation) was changed to those of a HG_{01}, HG_{10} or HG_{11} mode, we observed significant production of white-light in the main lobes of the intensity distribution. Because self-focusing is known to play an important role in white-light generation, by calculating the self-focusing lengths of the resulting transverse intensity profiles we have qualitatively confirmed this effect. The calculations with experimentally obtained parameters of the beams confirmed that the resulting transverse HG_{01}, HG_{10} and HG_{11} intensity configurations have self-focusing distances shorter than the cell length, while the Gaussian beam requires a longer cell for strong white-light production.

#167058 - $15.00 USD Received 18 Apr 2012; revised 19 May 2012; accepted 19 May 2012; published 30 May 2012

There is only one beam on the output of the setup so the lobes “beams” in this beam are mutually coherent. Coherence of white light sources from single laser beam was studied and confirmed in [33]. The coherence of the white light radiation is an important aspect, and the beam lobes of coherent white-light radiation can be used for spectroscopy and pump-probe experiments. This aspect is the subject of our future studies.

Acknowledgments

This work was partially supported by the Robert A. Welch Foundation (grant No. A1546), the National Science Foundation (NSF) (grants Nos. 0722800 and 0555568), and the U.S. Army Research Office (grant No: W911NF-07-1-0475).

#167058 - $15.00 USD Received 18 Apr 2012; revised 19 May 2012; accepted 19 May 2012; published 30 May 2012